Problems of planetology, cosmochemistry and meteoritica

Alexeev V.A., Pavlova T.A. Peculiarities of distribution of the gas-retention and cosmic-ray exposure ages of ordinary chondrites depending on their physical properties. UDC 550.42

Vernadsky Institute of Geochemistry and Analytical Chemistry RAS, Moscow (AVAL37@mail.ru)

Abstract. The distributions of the gas retention and cosmic-ray exposure ages of ordinary chondrites are studied deppending on their porosity. A positive correlation with the porosity of contents both radiogenic and cosmogenic isotopes of noble gases in chondrites and the corresponding ages of meteorites is found. In all distributions, chondrites with small porosity have smaller ages.

Keywords: *meteorites, gas-retention ages, cosmic-ray exposure ages, porosity.*

Introduction. Data on gas retention ages and cosmic-ray exposure ages of meteorites can be attract to obtain information about the structure and thermal history of the meteorites parent bodies, and also about catastrophic collisions in space, at identifying meteoroid streams, at deciding the question about the difference between the sources of Antarctic and non-Antarctic meteorites, and also at identifying paired meteorites i.e. samples belonging to the same fall. Knowledge of the cosmic-ray exposure ages is necessary to determine the equilibrium contents of long-lived cosmogenic radionuclides in meteorites when studying variations of galactic cosmic rays, as well as in the resolving other tasks.

The age of the meteorite can be distorted due to diffusion losses of gases. These losses, in particular, are determined by the physical properties of the meteorite matter. One of the fundamental properties is porosity, the study of which in meteorites of different chemical classes is devoted to many works (Wasson, 1974; Yomogida, Matsui 1983; Alekseev, Kuyunko, 1997; Consolmagno, Britt, 1998; Britt, Consolmagno, 2003; Consolmagno et al., 2008). The most representative data of data on porosity was published in (Macke, 2010), where the results of measurement and analysis of data on porosity, density and magnetic susceptibility of more than 1200 samples from 664 meteorites are presented.

In this paper, we consider the features of the age distributions depending on porosity for the most common chemical groups of meteorites - H- and L-chondrites (more than 80% of all meteorite falls accounts to their share). The age distributions for meteorites with the known porosity are compared with previously obtained age distributions of more than 350 H and L chondrites.

Details of the calculations and the results of the determination of ages are given in (Alekseev, 2005) and in the refs there. The porosity information is taken from (Macke, 2010).

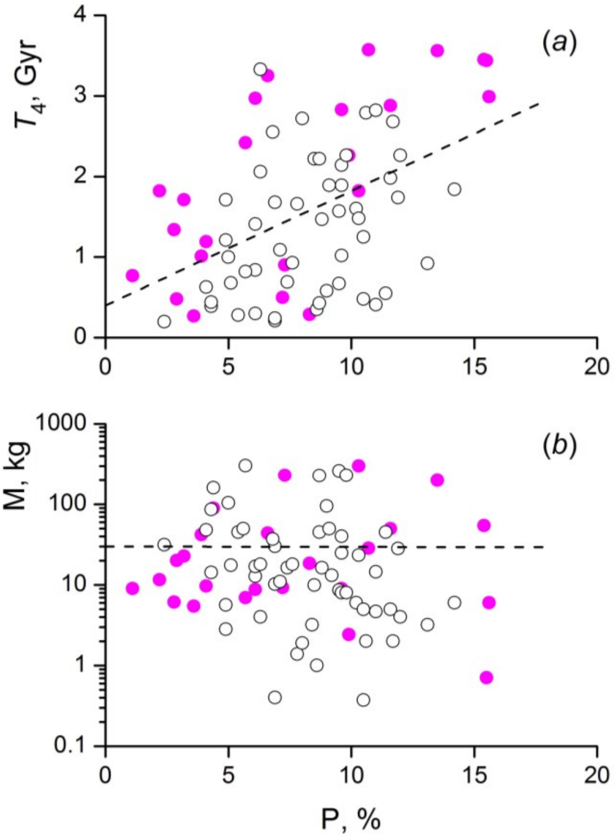

Fig. 1. Distributions: (*a*) U,Th-He gas retention ages (T_4) and (*b*) of found masses (M) of L-chondrite falls of different petrological types depending on the porosity of meteorites (P). Filled symbols refer to chondrites of L3, L4, and L5, open symbols refer to L6. Dashed lines are the regression lines for all L-chondrites. Parameters of the lines are given in the Table 1.

Correlation dependencies. For all distributions studied, the main peculiarity is characteristic: with growing porosity an increase of both the contents of cosmogenic and radiogenic gases and the corresponding ages. So, for example, in **Fig. 1a** it is seen the increase U,Th-He ages of gas retention of (T_4) for L-chondrites with growing increasing porosity. The parameter b in the equation for the regression line ($y = a + bx$) for all L-chondrites shown in the figure (0.142 ± 0.031) and the corresponding correlation coefficient r (0.47 ± 0.09) are significantly different from zero. A similar trend persists in the case of considering the data separately for two groups of L-chondrites - low (L3+L4+L5) and high (L6) petrological types (**Table 1**). It is characteristic that for chondrites of low petrological types (L3-L5), the values of b and r are significantly higher than for the most metamorphosed chondrites (L6). A decrease in the values b and r with growing petrological type indicates the decrease in the dependence of age on porosity.

The considered features peculiar properties of the distributions are found only for gases and ages calculated by their content; the gas content may decrease due to diffusion losses, which will result in a corresponding decrease in ages. No any correlation dependency was found between the porosity and the found masses of both L-chondrites (**Fig. 1b**, Table 1) and H-chondrites of various petrological types.

Table 1. Parameters of the equation of the regression lines $y = a + bx$ in the distribution of gas-retention ages (T_4) and the found masses (M) of L-chondrites of different petrological types depending on porosity of meteorites (Fig. **1).**

Distributions	Meteorites	*n*	*a*	*b*	*r*
T_4, Gyr	All	74	0.40 ± 0.27	0.142 ± 0.031	0.47 ± 0.09
	L3, L4, L5	23	0.61 ± 0.36	0.178 ± 0.041	0.69 ± 0.11
	L6	51	0.41 ± 0.37	0.113 ± 0.043	0.35 ± 0.12
lg M, kg	All	80	1.48 ± 0.18	-0.036 ± 0.021	-0.04 ± 0.11
	L3, L4, L5	25	1.36 ± 0.23	-0.008 ± 0.027	-0.06 ± 0.20
	L6	55	1.76 ± 0.30	-0.074 ± 0.034	-0.29 ± 0.13

Notes: *n* is the number of meteorites; *r* is the correlation coefficient.

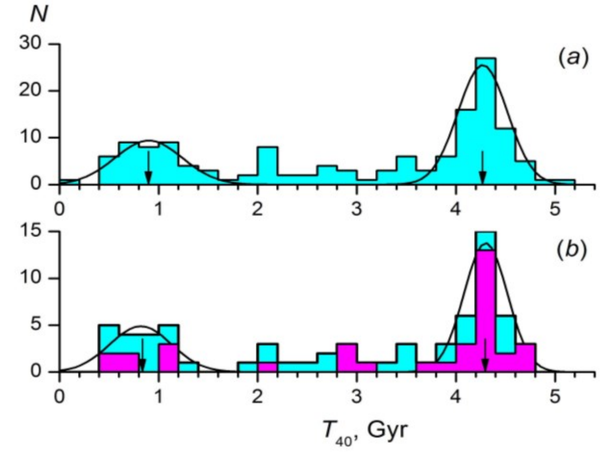

Fig. 2. Distributions of K-Ar gas-retention ages (T40) of L-chondritfe falls. a) - all meteorites (n = 143); (b) - meteorites with known values of porosity P (n = 69). The darker filling corresponds to the meteorites with porosity $P \geq P_{med}$ (n = 35). The arrows indicate the positions of the maxima of the Gaussian curves.

Table 2. The median age values in the distributions of T_{40}, T_4 and T_{21} of L-chondrites (Figs 2-4).

Age	Meteorites			
	All	P > 0	$P < P_{med}$	$P \geq P_{med}$
T_{40}, Gyr	3.5	3.5	2.6	4.2
T_4, Gyr	1.5	1.5	1.0	1.9
T_{21}, Myr	21.1	18.0	16.1	24.2

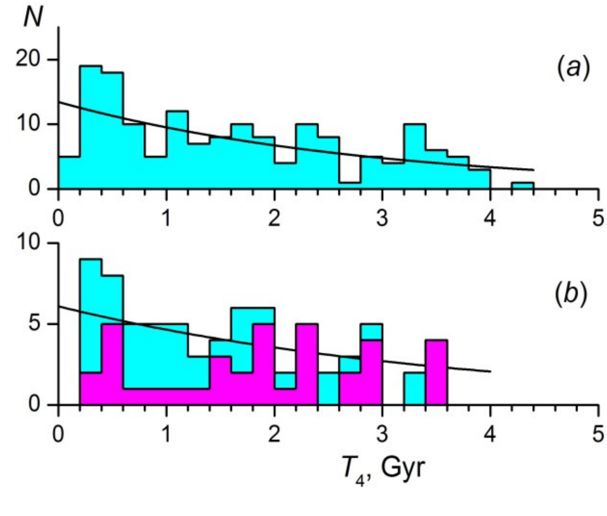

Fig. 3. Distributions of U,Th-He-ages of gas retention (T_4) of falls of L-chondrites. *a*) - All meteorites (*n* = 159); (*b*) - meteorites with known values of porosity P (*n* = 74). The darker filling corresponds to meteorites with porosity $P \geq P_{med}$ (*n* = 37). The curves are regression lines.

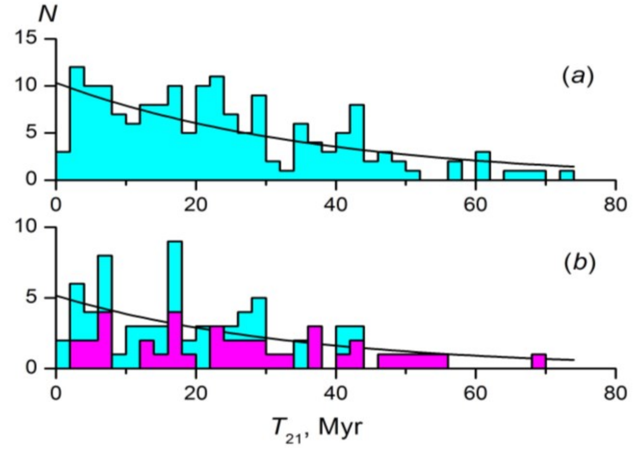

Fig. 4. Distributions of the cosmic-ray exposure ages (T_{21}) of falls of L-chondrites. a) - all meteorites (*n* = 167); (*b*) - meteorites with known values of porosity P (*n* = 78). The darker filling corresponds to the meteorites with porosity $P \geq P_{med}$ (*n* = 39). The curves are regression lines.

Age distribution of meteorites. Many works have been devoted to the study of the age distribution of ordinary, chondrites (Alekseev, 2005 and references given there). Often, distribution analysis is performed to establish a collisional history of meteorites (Graf, Marti, 1995). However, the type of distributions and the corresponding conclusions in their analysis may depend on the physical properties of meteorites. The following is a matching of the age distributions of L-chondrites as for all meteorites and for chondrites with different porosity (**Figs 2-4**). We are note that for the considered ages (T_{40}, T_4 and T_{21}) the distributions for all meteorites are similar to those for meteorites with the known porosity that indicates on the representativeness of the sample of meteorites with known porosity. The characteristic feature is that in all distributions the meteorites with higher porosity $P \geq P_{med}$ (where P_{med} is the median value of porosity for the considered populations) have mostly higher ages than meteorites of less porosity (Table 1). A similar pattern is observed and for H-chondrites.

Conclusions. The distributions of gas-retention ages (T_4 and T_{40}) and cosmic-ray exposure ages (T_{21}) for ordinary chondrites were studied depending on their porosity. A positive correlation was found with the porosity of both the contents of radiogenic and cosmogenic isotopes of noble gases in chondrites, and also of the corresponding ages of meteorites. In all distributions the chondrites with low porosity are characterized by the lower values of ages than the meteorites with high porosity. The regularities found can be explained by the higher diffusion losses of noble gases (especially He) from meteorites with low porosity, that the most likely was formed during the filling of large pores with fine dispersed mineral components during the impact events on the parent bodies of meteorites.

The work was partially supported by the Program No. 28 of the Presidium of the RAS.

References:

Alexeev V.A. The history of ordinary chondrites from the data on stable isotopes of noble gases (a review) // Sol. Syst. Res. 2005. V. 39. № 2. P. 124-149.

Alexeev V.A., Kuyunko N.S. Porosity and Thermal History of Meteorites // Sol. Syst. Res. 1997. V. 31. № 2. P. 157-162.

Britt D.T., Consolmagno G.J. Stony meteorite porosities and densities: A review of the data through 2001 // Meteoritics & Planetary Science. 2003. V. 38. P. 1161-1180.

Consolmagno G.J., Britt D.T. The density and porosity of meteorites from the Vatican collection // Meteoritics & Planetary Science. 1998. V. 33. P. 1231-1241.

Consolmagno G.J., Britt D.T. Macke R.J. The significance of meteorite density and porosity // Chemie der Erde – Geochemistry. 2008. V. 68. P. 1-29.

Graf Th., Marti K. Collisional history of H chondrites // J. Geophys. Res. 1995. V. 100. No. E10. P. 21247-21263.

Macke R.J. Survey of Meteorite Physical Properties: Density, Porosity and Magnetic Susceptibility // Ph.D. Thesis, University of Central Florida. 2010. 332 p.

Wasson J.T. Meteorites / Berlin: Heidelberg: N.Y.: Springer-Verlag, 1974. 316 p.

Yomogida K., Matsui T. Physical properties of ordinary chondrites // J. Geophys. Res. 1983. V. 88. P. 9513-9533.

Alexeev V.A., Kalinina G.V., Lorenz C.A., Pavlova T.A. Track studies of 2018-year falls of Ablaketka (H5) and Ozerki (L6) ordinary chondrites. UDC 550.42

Vernadsky Institute of Geochemistry and Analytical Chemistry RAS, Moscow (AVAL37@mail.ru)

Abstract. Track studies of the 2018-year falls of the Ablaketka (H5) and Ozerki (L6) ordinary chondrites were performed. Using data on the depth distribution of the formation rate of tracks of galactic cosmic ray VH-nuclei in meteorites of different pre-atmospheric sizes, pre-atmospheric sizes of these meteorites (*R*) and depths of location (*d*) of the samples studied were evaluated. For the Ablaketka chondrite, these values were found *d* = 2-6 cm in the pre-atmospheric body with *R* ≥ 6 cm. The absence of tracks in olivine grains of the chondrite Ozerki is possibly due to the low cosmic-ray exposure age of this meteorite.

Keywords*: chondrites, pre-atmospheric sizes, cosmic-ray exposure ages, VH-nuclei of galactic cosmic rays.*

Introduction The main source of galactic cosmic ray (GCR) tracks in meteorites are the iron group nuclei (VH-nuclei, 23 < Z < 28). Their abundance in the composition of GCR far exceeds the abundance of heavier elements. During deceleration of these nuclei in the matter of meteorites, zones of radiation micro-damage are formed in the silicate crystals. The appropriate chemical etching can increase them up to micron sizes, i.e. tracks become visible under an optical microscope. The length of the tracks depends on the charge and energy of the deceleration nuclei. VH-nuclei form the tracks in silicate minerals, such as olivine and pyroxene for the most common stone meteorites, and the average length of such tracks is about 10 μm.

The rate of formation of tracks strongly depends on the degree of shielding. For example, at a depth of 40 cm from the surface of a meteorite, the rate of formation of tracks of VH nuclei decreases by eight orders of magnitude (Bhattacharya et al., 1973). This makes the tracks the most accurate indicators of the depth of location of the studied samples and allows us to estimate the pre-atmospheric dimensions of meteorites and their ablation during the passage of the Earth's atmosphere. Track data, together with the results of analysis of the content of cosmogenic nuclides in meteorites, are successfully used in complex studies of freshly fallen meteorites, which allows to establish not only the radiation history of meteorites, but also to make estimates of the distribution and variations of cosmic radiation in the heliosphere (see, for example, Alexeev, 2005).

The paper presents the results of track studies for two chondrites 2018-year falls.

Research results The method of the carried out track research is considered in (Alexeev et al., 2012). Olivine grains (size fractions from 50 up to 200 μm) were used to measure the track parameters. From 0.5-1 g of the sample weight of each of studied samples of chondrites provided from the Collection of Meteorites of the Russian Academy of Sciences, several dozen of the silicate grains suitable for carrying track studies were separated out. The olivine grains hand-picked under a binocular microscope were mounted into epoxy resin tablets, then they were polished and chemical etched at a temperature of 110ºC in the multicomponent WN solution (Krishnaswami et al., 1974). The WN solution is designed to identify tracks formed by the VH-nuclei of the GCR in olivine. Before etching the surface of each investigated crystal was examined under a microscope in order to identify and fix the various dislocations, defects and other track-like micro destructions of the crystal structure. The chemical etching of natural tracks in the studied olivine grains was controlled by the way of registration of the artificially induced tracks from the fission fragments of the ^{252}Cf source (Alexeev et al., 2012).

When studying the track distributions in olivine crystals of chondrites there are usually used the calculated track formation rates in pyroxene (ρ/t, where ρ is the track density, cm^{-2} and t is the cosmic-ray exposure age of the meteorite, Ma) depending on the depth position of the sample (*d*, cm) in meteorites of the different pre-atmospheric sizes (Bhattachrya et al., 1973). In this regard, the data obtained for olivine are corrected using the data for pyroxene. The correction takes into account that the rate of the track formation in pyroxene is higher than in olivine. The excess ratio was found to be 1.8 ± 0.5; 2.4 ± 0.5; 2.1; 2.9 (according to data (Aaloe et al., 1979; Pereligin et al., 1975), etc.). In this work, the average value of this value was found equal to 2.3 ± 0.5 (Alexeev et al., 2018).

The Ablaketka meteorite fell on February 16, 2018, closely to Ablaketka, a suburb of Ust-Kamenogorsk, Kazakhstan. The weight of the individual samples was ranged from 0.1 to 1.2 kg. Total was found 10 specimens. The total mass of the meteor shower was about 5.5 kg. The Ablaketka meteorite is presented by individual exemplars composed of light-grayish chondritic material. Some samples composed of dark-grayish- to black highly shock-metamorphosed (shock-darkened) chondritic matter. The inclusions of this material up to several cm in size those have the sharp contacts with the host were found in the chondritic individual samples as well. Thus, the meteorite has brecciated texture and contains less metamorphosed host and about 20 vol% of highly shock metamorphosed inclusions. According to the petrographic analysis, the meteorite is classified as ordinary chondrite (H5, monomictic breccia), impact stage S3, weathering class W0 (Meteoritical Bulletin, 2018). The track analysis was performed on the samples of chondrite lithology of the Ablaketka meteorite.

The tracks were measured in olivine crystals separated out from the 560 mg sample. In the 43 crystals on a total area 1.35 10^{-3} cm^2, 2561 tracks were found, which corresponds to the average track density ρ_{Ol} = 1.9 10^6 см$^{-2}$. The distribution of the track density of VH-nuclei of GCR in the olivine grains is shown in **Fig. 1**. Information about the cosmic ray exposure age (t) of the Ablaketka meteorite is currently missing. In this connection, for calculating the rate of track formation (ρ/t) necessary for estimating the values of *d* and *R*, the data on the distribution of the cosmic ray exposure ages of H-chondrites (**Fig. 2**) were used: the meteorite studied belongs to this chemical group of chondrites. According to the cumulative curve, three "fixed" ("reference") values of age were chosen: 4.0; 8.8 and 38.2 Ma, corresponding to the accumulated frequency w = 0.1; 0.5 and 0.9. (The magnitude of the frequency w shows what proportion of meteorites has an age $t < t_w$.) For the selected reference age values, the rates of the track formation are calculated and the estimates of *d* and *R* are made according to dependencies obtained by Bhattachrya et al. (1973). The calculation scheme and the results for w = 0.5 (and, accordingly, t = 8.8 Ma) are shown in the Fig. 3 and in the table. From these data, it follows that for the selected age, the depth of the sample studied was d ~ 2-6 cm in the pre-atmospheric body with a radius $R \geq 6$ cm. Similar calculations performed for other reference values of age (4.0 and 38.2 Ma) gave the close values: 2-4 and 5-10 cm for *d* and ≥4 and ≥10 cm for *R*, respectively.

The Ozerki meteorite fell on June 21, 2018 in the Lipetsk region, Russia. Found more than 90 specimens. The summary mass of the meteorite shower was more than 6.5 kg. Among the chondritic individual exemplars the samples of brecciated texture were found. The brecciated samples are composed of the fragments of chondrite matter ranging in size from tens of microns to 1 cm enclosed in dark cement (matrix), which is the shock melt of chondrite. According to the results of petrographic analysis, the meteorite was classified as the ordinary chondrite (L6), impact stage S4/5, weathering class W0 (Meteoritical Bulletin, 2018). The samples of chondritic lithology were used for the track studies.

The tracks were measured in olivine crystals separated out from two weights of 550 and 162 mg of the sample No. Oz-1. In the 163 crystals on a total area of 2.8 10^{-2} cm^2, no tracks were found, i.e. the track density in the selected out olivine grains was $\rho_{\mathrm{Ol}} \leq 36$ cm^{-2} and at correcting for pyroxene $\rho_{\mathrm{Px}} \leq 90$ cm^{-2}.

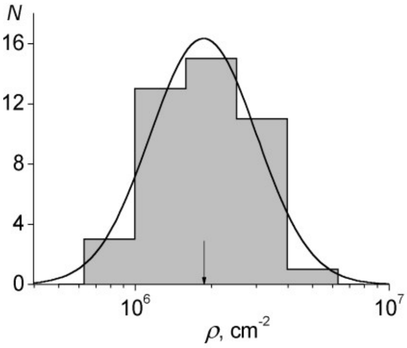

Fig. 1. The distribution of the track density (*ρ*) of VH-nuclei of GCR in the olivine grains (*N* = 43) of the Ablaketka H5 chondrite. The distribution is approximated by a Gaussian curve. The arrow indicates the position of the maximum: $\rho = (1.9 \pm 0.2)\ 10^6\ cm^{-2}$.

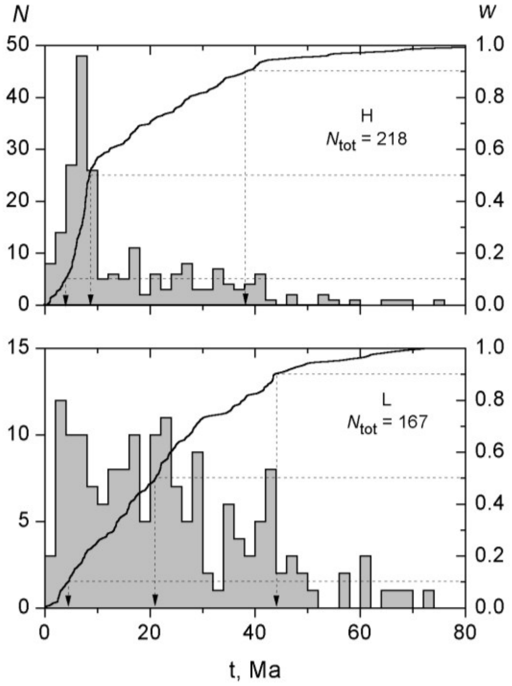

Fig. 2. Distributions of cosmic ray exposure ages (t) of H- and L-chondrites falls (histograms). The solid lines are cumulative distribution curves. The dashed lines indicate the values of the accumulated frequency *w* = 0.1; 0.5 and 0.9 and the age values corresponding to these frequencies (shown by arrows): 4.0; 8.8 and 38.2 Ma for H-chondrites and 4.5; 21.0 and 44.0 Ma for L-chondrites.

Table. The results of track studies of meteorites.

Meteorite	N_{tr}	*S*, 10^{-3} cm^2	ρ_{Ol}, cm^{-2}	ρ_{Px}, cm^{-2}	$t_{w=0.5}$, Ma	$\rho_{Px}/t_{w=0.5}$, cm^{-2} Ma^{-1}	*d*, cm	*R*, cm
Ablaketka	2561	1.35	1.9 10^6	4.4 10^6	8.8	5.0 10^5	2-6	≥6
Ozerki	≤1	28	≤36	≤90	21	<100*	≥30	≥50

* For t = 1 Ma.

Information about the cosmic ray exposure age (t) of the Ozerki meteorite is absent. In this connection, for calculating the rate of formation of tracks (ρ/t), which is necessary for estimating the values of *d* and *R*, the data on the distribution of cosmic ray exposure ages of L-chondrites were used (Fig. 2). According to the cumulative curve, for the values of the accumulated frequency of 0.1; 0.5 and 0.9, three "fixed" age values were selected: 4.5; 21.0 and 44.0 million years. However, the absence of tracks in the olivine grains of the Ozerki meteorite may be due to the short duration of irradiation with galactic cosmic rays of the meteoroid after its separation from the parent body. In this regard, when calculating the minimum values of d and *R* for the calculating rate of accumulation of tracks, the value of the cosmic ray exposure age t = 1 million years was chosen. The calculation scheme and the obtained limiting (minimum) values of *d* and *R* are shown in **Fig. 3** and in the **Table**. From these data, it follows that even for such a low CRE age t = 1 Ma, the absence of tracks may be due to the considerable depth of position of the investigated sample *d* ≥30 cm in the body with the pre-atmospheric radius *R* ≥ 50 cm.

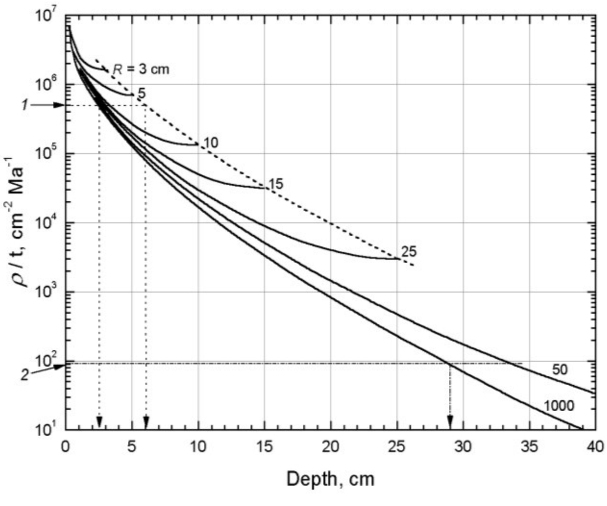

Fig. 3. Track formation rate (*ρ*/t) of VH-nuclei of GCR in chondrites depending on the depth of the sample in the pre-atmospheric body of radius *R*. The dashed line is the

interpolation of the track formation rate values in the centers of the pre-atmospheric bodies. The dashed line is an estimate of the depth of the sample and the pre-atmospheric size of Ablaketka chondrite according to the average rate of track formation (arrow 1 to the ordinate axis). The dash-dotted line is an estimate of the limiting values of the depth of occurrence and the pre-atmospheric size by the limiting value of the rate of track formation in the Ozerki chondrite (arrow 2 to the ordinate axis).

If, however, when calculating the rates of the track formation, to choose the higher values of the cosmic ray exposure age: t = 4.5; 21.0 and 44.0 Ma, corresponding to the values of $w = 0.1$, 0.5 and 0.9 in the L-chondrites age distribution discussed above (Fig. 2), then the obtained values of d and R will be significantly higher than the values given in the Table for this meteorite.

Conclusions Track studies of olivine crystals separated from the Ablaketka (H5) and Ozerki (L6) chondrites, fell out in 2018 were carried out. Using the data on the depth distribution of the rate of the GCR VH-nuclei track formation in meteorites of different pre-atmospheric sizes, there were estimated the pre-atmospheric sizes (R) and the depth location (d) of the studied sample. For the Ablaketka chondrite, these values were found d = 2-6 cm in the pre-atmospheric body with $R \geq 6$ cm. The absence of tracks in the olivine crystals of the Ozerki chondrite implies the location of the sample studied at the great depth $d \geq 30$ cm in the pre-atmospheric body with $R \geq 50$ cm. This conclusion (location of the sample of the Ozerki meteorite at the great depth) requires further research with involving new samples of the meteorite.

The work was partially supported by the Program No. 28 of the Presidium of the RAS.

References:

Aaloe A.O. et al. On the preatmospheric sizes of the Yamyshev pallasite // Communications of the Joint Institute of Nuclear Research. Dubna. 1979. P. 14 – 12937 (*in Russian*).

Alexeev V.A. The history of ordinary chondrites from the data on stable isotopes of noble gases (a review) // Sol. Syst. Res. 2005. V. 39. № 2. P. 124-149.

Alexeev V.A., Bagulya A.V., Volkov A.E., Goncharova L.A., Gorbunov S.A., Kalinina G.V., Konovalova N.S., Okateva N.M., Pavlova T.A., Polukhina N.G., Starkov N.I., Than Naing Soe, Chernyvsky M.M., Shchedrina T.V. The track studies of olivine crystals in the pallasites // Proceedings of the All-Russian Annual Seminar on Experimental Mineralogy, Petrology and Geochemistry. Moscow, April 18-19, 2018. Moscow: GEOKHI RAS. 2018. P. 286-289.

Alexeev V.A., Gorin V.D., Ivliev A.I., Kashkarov L.L., Ott U., Sadilenko D.A., and Ustinova G.K. Integrated Study of the Thermoluminescence, Noble Gases, Tracks, and Radionuclides in the Fresh_Fallen Ash Creek L6 and Tamdakht H5 Chondrites // Geochemistry International. 2012. V. 50. № 2. P. 105–124.

Bennett, M. E., & McSween, H. Y. Shock features in iron-nickel metal and troilite of L-group ordinary chondrites // Meteoritics & Planetary Science. 1996. V. 31. № 2. P. 255–264.

Bhattacharya S.K., Goswami J.N., Lal D. Semiempirical rates of formation of cosmic ray tracks in spherical objects exposed in space: pre- and post-atmospheric depth profiles // J. Geophys. Res. 1973. V. 78. № 34. P. 8356-8363.

Krishnaswami S., Lal D., Prabhu N., Tamhane A.S. Olivines: revelation of tracks of charged particles // Science. 1974. V. 174. № 4006. P. 287–291.

Meteoritical Bulletin. 2018. № 107. https://www.lpi.usra.edu/meteor/

Perelygin V.P., Viik Sh.B., Otgonsuren O. On determination of preatmospheric dimensions of Marjalahti meteorite // Communications of the Joint Institute of Nuclear Research. Dubna. 1975. P. 13 – 8359 (*in Russian*).

Badekha K.A.[1], Uymin A.A.[2] Optical features of the schlieren bands in Chinga meteorite in a front reflection of light UDC 669 72

[1] Vernadsky Institute of Geochemistry, Moscow, [2]Ural Technical Institute of Communications and Informatics, Ekaterinburg (ksenia_uimina@mail.ru)

Abstract. Most of the ataxites demonstrate the bands of selective reflection (Schlieren bands) in the polished and etched sections. Optical properties of Chinga meteorite (Fe-18 weight.% Ni) with different depth of etching relief – 10, 85, 280, 500 nm were investigated in the paper. Measurements were carried out on a single-beam spectral installation in the range 180-1080 nm. A halogen lamp with a power of 12-35 V was used as a radiation source, the spectrum was recorded using the FSD-8 mini-spectrometer connected to the microscope by a special single-mode fiber-optic cable. When snapping the reflection spectra, it was found that the Schlieren bands differ only in the ratio of the picks on the plot. Frontal reflection shows that the critical wavelength is 350 nm, in the area of which there is a change in the sign of the graph of subtraction of the reflection spectra of "light" and "dark" Schlieren bands.

Keywords: *ataxites; plessite structure; spectrometer; spectrum.*

The reflection method has been traditionally used to measure the optical characteristics of a wide class of materials. It is based on the definition of the reflection coefficient $R(\hbar\omega)$ of the light waves from measurements of the intensity of the incident $I_0(\hbar\omega)$ and reflected $I(\hbar\omega)$ light: $R(\hbar\omega) = I(\hbar\omega) / I_0(\hbar\omega)$. Here it was used to quantify the optical effect of selective reflection bands (Schlieren bands) in the ataxites.

The group of high-Nickel (15-18 wt.% Ni) meteorites - ataxites differs from other groups by a pronounced structure of plessite consisting of a mixture of submicroscopic bcc- and fcc-phases. Occasional small (15x100 µm) embryos of widmanstatten bcc-kamacite. One of the features of this group is the presence of parallel bands of selective reflection 1-10 cm wide on the surface of etched sections (Badekha K.A., 2012; Buchwald V. F., 1981). Here we study the Schlieren bands on the example of Chinga ~17 wt.% Ni. To measure the effect we recorded the spectra of the frontal light reflection from the given areas of the polished section.

Material and methods. A sample of Chinga meteorite (16.58 wt.% Ni, 0.55 wt.% Co, 0.05 wt.% P) was selected for the research, demonstrating the most finely dispersed structure among all the studied meteorites and parallel big Schlieren bands (Fig. 1). The sample was polished on a diamond paste followed by finishing on a colloid. The sample was then sequentially etched in HNO_3 followed by purification in distilled water using an ultrasonic bath. The depth of the polished surface etching terrain was 10, 85, 280, 500 nm.

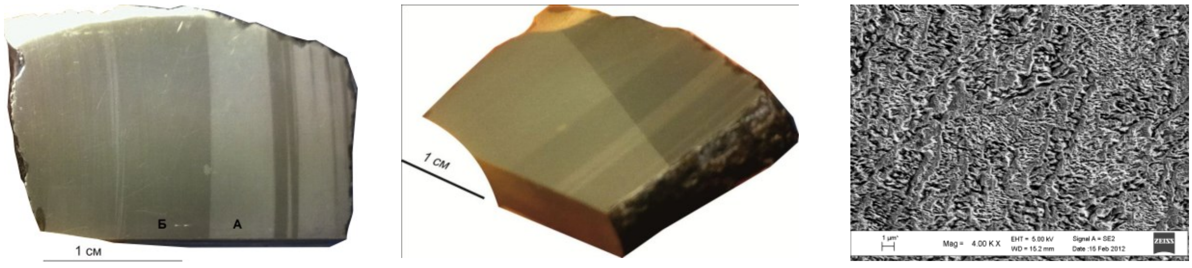

a b c

Fig. 1. Chinga meteorite after etching: (a), (b) – Schlierenbands at different angles; (c) – SEM- image of the surface - the structure of the plessite is visible.

After etching the sample, the depth of the surface topography and the size of the subgrains in plessite were estimated using “FemtoScan Online” Scanning probe microscope. The size of small grains of round shape and cross-section of grain ridges in the light area "A" was 270, 310, 323, 344, 372, 417 and 524 nm (average – 365 nm), the size of small grains in the dark region “B” was 286, 284, 452 nm, large grains were 1.6 microns wide.

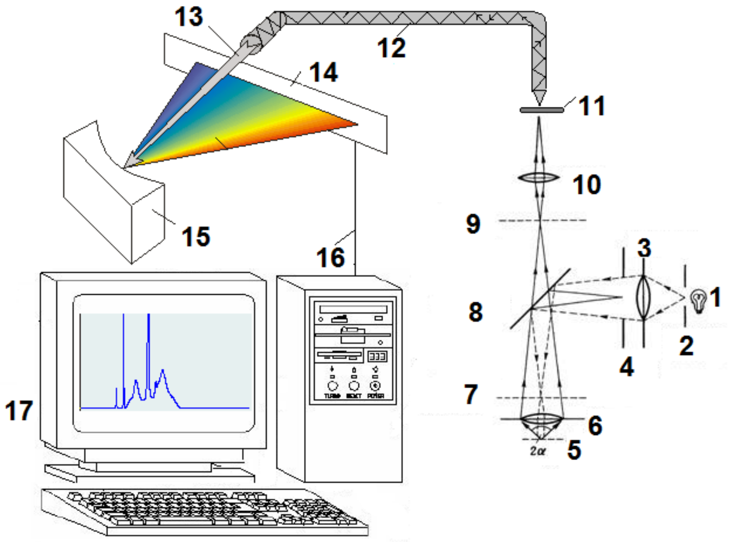

Fig. 2. The scheme of installation for measuring the intensity of reflected radiation from the predetermined region of the sample surface:

1 – the lamp, 2 – aperture diaphragm of the condenser, 3 - condenser lens, 4 -the true image, 5 – the sample, 6 – the lens, 7 – the rear focal plane of the lens, 8 – the translucent mirror, 9 – the plane of the first image, 10 – the ocular, 11 - adapter, 12 – fiber, 13 – the investigated radiation, 14 – the optical sensor plane, 15 - a spherical diffraction grating, 16 – spectral data, 17 - PC

The measurements of spectral characteristics were carried out on a single-beam spectral installation specially designed to measure the reflection spectra, implemented on Zeiss Axiovert 40 MAT microscope. Using the aperture of the microscope, a local area of the section was selected, different magnification X20, X50, X100 was applied to estimate the effect of the contrast beween the bands structure. A halogen lamp with a variable 12-35 V radiation power was applied as a radiation source. The spectrum was recorded and analyzed using the FSD-8 mini-spectrometer connected to the microscope by a special single-mode fiber-optic cable (Fig. 2). To organize the connection of the microscope output with the input of the fiber optic cable, adapters with adjustable focal length were specially made. This allowed us to adjust the amount of illumination of the photodiode bar matrix. An optical fiber with a diameter of 100 microns equipped with an optical connector was used as an input optical gap of the measuring circuit. It was installed on the wall of the device allowing connection of an external fiber optic cable for the delivery of optical radiation. The inlet, which is the polished end of the optical fiber, is located in the focal plane of the spherical (concave) diffraction grating and serves for investigated radiation input. The spectrum range analyzed was 180-1080 nm, but reliable data lay between 410-650 nm because of the radiator and the optics of the microscope features.

Since it is difficult to register the own spectrum of the radiation source in this installation, a comparison of two reflection spectra in a wide spectral range was used.

The diffraction grating decomposes the light signal into monochromatic components and creates a spectrum image in its focal plane. An optical sensor with linearly arranged light-sensitive elements (pixels) is installed in this focal plane. The intensity distribution vs the wavelength data are transmitted to the PC using a standard cable with an USB connector. Initial analysis of the spectra is carried out in the FSD Soft software 1.1. The software allows recalculation of the spectra and its export for further processing into Microsoft Excel or Origin format.

Results and discussion. The measurements were carried out at different magnification to estimate the influence of the square from which the image is recorded to the magnitude of the Schlieren bands effect. At high magnification, the difference between the resulting spectra faded away. In other cases, the ratio between the spectral peaks was estimated (Fig. 3).

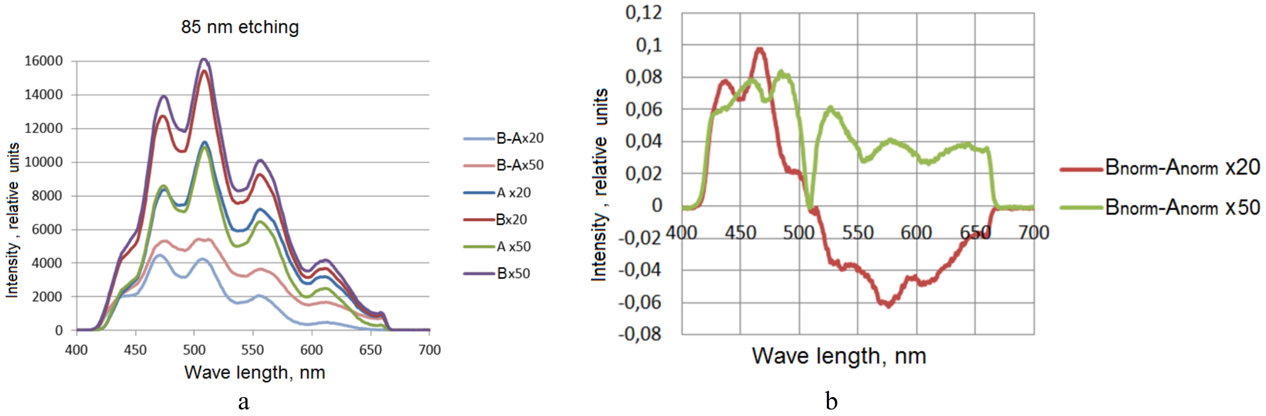

Fig. 3. Analysis of reflection spectra at the 85 nm etching depth: (a) – reflection spectra of the Schlierren bands, (b) – difference normalized spectra for "A" and "B" at x20 magnification (red curve) and x50 (green curve). Diaphragm 512 ms.

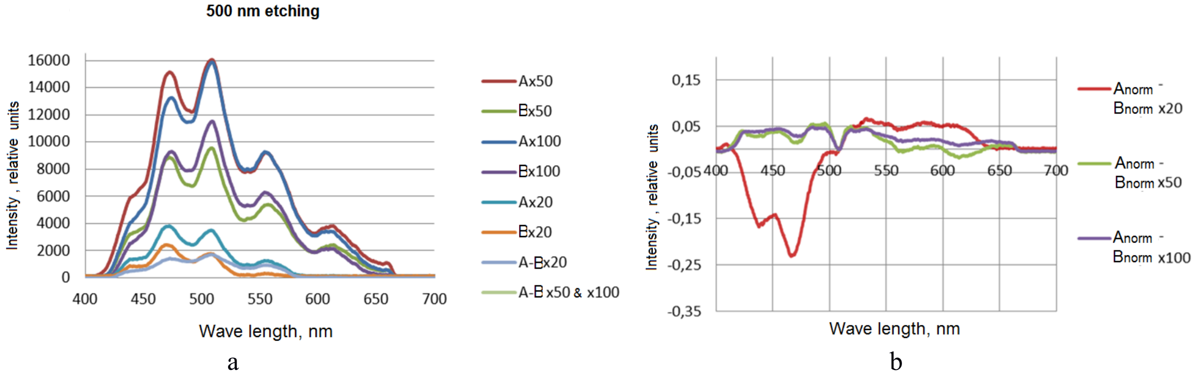

Fig. 4. Analysis of reflection spectra at 500 nm etching depth: a – reflection Spectra of the Schlieren bands "A" and "B", b – difference normalized spectra for "A" and "B" at the magnification x20, x50 and x 100. Aperture 1024 ms.

It is noticeable that in the spectra of the regions "A" and "B" have three main peaks corresponding to 470, 510 and 660 nm wavelength, which highlights the blue, green and red components of the spectrum. With increasing of the etching depth, the form of the spectra changes a little (Fig. 4). Informative becomes only the magnification x20.

When analyzing the difference spectra, it is noticeable that in the "A" region the orange-red component slightly prevails, in the "B" region the blue-green one is expressed. At the same time in the "B" region with the etching increase saturation of 410-470 nm spectral range also increases (figure 2B,3b, magnification x20), and the "A" region remains slightly enriched in the spectrum above 510 nm. Thus, despite the loss of illumination in the optics of the microscope, the photodetector receives enough radiation to record the difference in the reflection spectra of the Schlieren bands.

Analyzing the normalized spectra it should be noted that when considering the areas under high magnification, the reflection spectrum between the Schlieren bands is minimal. This, apparently, is due to the fact that the black plessite – the product of martensite decomposition (J. I. Goldstein, 2006) occupies significant area of the sample surface, in comparison with directed plessite. The intensity is always higher for the light area and lower for the

Matt. In the "B" band spectrum wavelengths of 400-500 nm prevail, in the "A" band the range of 500-650 nm prevails.

Conclusion. The front reflection spectra for the "bright" and "dark" Schlieren bands in Chinga allow us to estimate of the contribution of the spectral components in the effect of the bands. The differences are in the correlation between the peaks of the 470, 510 and 660 nm. The increase in the etching depth leads to a change in the intensity for both bands synchronously with the preservation of the spectral wavelength separation effect. In the analysis of the terrain, the regularity of the structure in the "B" band is observed, it is also possible to distinguish a single peak in the difference reflection spectrum corresponding to λ=470 nm, so this structure can be represented as a diffraction grating. Its period, according to the spectral analysis, is a multiple of 235 nm (2·d·SinΘ=k·λ, SinΘ=1, λ=470 nm), which is correlated with the terrain measurement data using SPM. For the "A" band it is difficult to distinguish a separate period, but according to the existing peaks on the difference spectrum graphs, structures with a period of ~280 nm and 300 nm (λ~560 and 600 nm) are observed. Since the change in the sign of the graphs is observed at 510 nm, it can be said that the structures of ~250 nm in size are observed in both Schlieren bands.

References:

Badekha K. A., Grokhovsky V. I., Yakovlev G. A. Study of Schlieren bands in the ataxites using EBSD method// Meteoritics and Planetary Science.- 2012. - V. 46. № S1. - P. A49.

Buchwald V. F. On the Oriented Sheen in Ataxites // Meteoritics. - 1981. Vol. 16.- P.298-299.

Goldstein J.I. The formation of plessite in meteoritic metal / Goldstein J.I., Michael J.R. // Meteoritics and Planetary Science.- 2006. - Vol. 41, № 4.- P. 553-570.

Barenbaum A.A, Klimov D.S. Theoretical model Anderson-Schulz-Flory as a tool to study geosynthesis mechanism UDC 551.23: 525.235

Oil and Gas Research Institute RAS (OGRI RAS), Russia, Moscow azary@mail.ru, seydem@mail.ru

Annotation: Using the theoretical model of Anderson-Schulz-Flory and its modifications, it is shown that hydrocarbons of oil, gas and bitumen are formed from carbon oxides and water by the mechanism of geosynthesis. At the same time, unlike other reactions of polycondensation synthesis of hydrocarbons, the chemical formula of geosynthesis must necessarily take into account the catalytic properties of the geological environment.

Keywords: *geosynthesis; hydrocarbons; Anderson-Schulz-Flory model.*

Introduction. We named geosynthesis (Zakirov et al, 2013) as a polycondensation synthesis of hydrocarbons of a gas and oil series occurring in a matrix of rocks saturated with water, mechanically activated by seismotectonic processes (Discovery No. 326). In this mechanism, the hydrogen donor in hydrocarbons is water, and organic matter, carbon dioxide (CO2) dissolved in water, and carbon-containing minerals are carbon donors. Although geosynthesis was studied by many authors (Molchanov, 1967; Molchanov et al, 1988, 1992; Trofimuk et al, 1981; Chersky, Tsarev et al, 1984, 1985, 1986; Zakirov et al, 2013; et al), it is impossible to consider this mechanism explained.

In this paper, the mechanism of geosynthesis is studied on the basis of the theoretical Anderson-Schulz-Flory model (ASF-model) intended for analyzing molecular-mass distributions (MMD) of hydrocarbons arising in Fischer-Tropsch synthesis (FT-synthesis). L. Glebov first attracted the ASF-model to study oil (2002). In the works (Barenbaum, 2007, Barenbaum, Abla, 2009), the ASF-model and its modifications were used in the analysis of n-alkanes of heavy oils, bitumens and gas hydrates. In this work the phenomenological formula of geosynthesis of hydrocarbons, taking into account the catalytic properties of the geological environment, is substantiated.

Anderson-Schulz-Flory model. The model got its name after G. Henrici-Olive and S. Olive (1987) first applied the equations of G. Schulz (1935) and P. Flory (1936) known in polymer chemistry for the description of the molecular-mass distributions (MMD) of hydrocarbons in the FT-synthesis products (n-alkanes, alkanols, alkylamines, alkenes, etc.). The first is established for MMD of polymers obtained by radical polymerization, and the second is the same polymers obtained by the method of linear polycondensation. The authors found that MMD calculated by both formulas and the Anderson formula (1984) are identical and well describe MMD of the individual monocomponents of FT-synthesis.

The classic Anderson-Schulz-Flory model can be represented by the formula:

$$lg(g_n/n) = n\, lg\alpha + lg(ln^2\alpha), \qquad (1)$$

where g_n – the mass fraction of hydrocarbons with the number n of atoms in the molecule, α – hydrocarbons distribution parameter ($0 < \alpha < 1$).

Formula (1) reflects the random continuous growth of the hydrocarbon chain due to the addition of new links (intermediates) to it and chain termination due to desorption in the case when the parameter α is constant and has a physical meaning $\alpha = r_p/(r_p+r_o)$, where r_p and r_o – chain growth and chain breakage independent of chain length.

By modifying the chemical process (1), a number of models are obtained, with the help of which it is possible to describe the main types of MMD during FT-synthesis (Glebov, Klige, 1994). Three of them are shown in fig. 1.

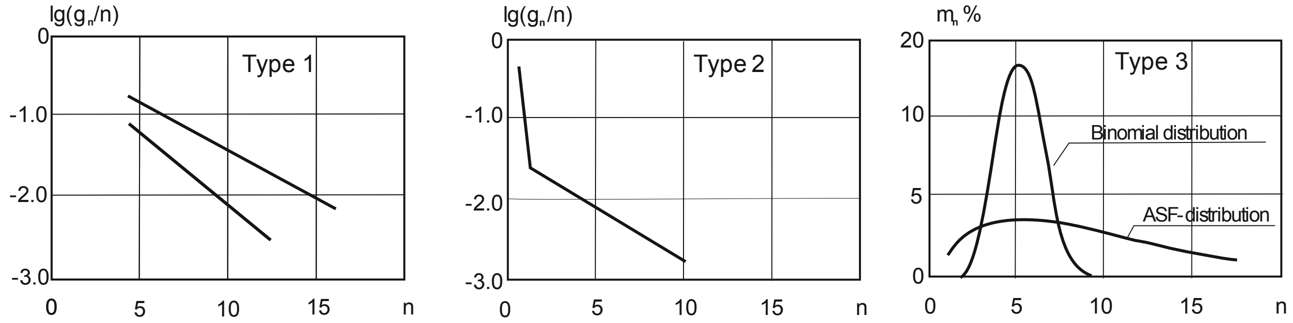

Fig. 1. Typical distribution of hydrocarbons in the products of the FT-synthesis.

Type 1 distributions are explained by the presence of several active hydrocarbon growth sites on the catalyst. Type 2 is characteristic of the products of the FT-synthesis with a high content of methane (CH_4). This type of MMD is explained by the existence of additional pathways for the formation of methane. Type 3 distributions follow the binomial law. For comparison, this figure shows MMD (1). The process of forming a hydrocarbon chain in their binomial distribution is also random. However, in this case it is limited by time or a finite number of events. The probability $P_n(k)$ that a hydrocarbon molecule consisting of k carbon atoms will arise as a result of n events is described by the expression:

$$P_n(k) = \frac{n!}{k!(n-k)!} p^k (1-p)^{n-k} \qquad (2)$$

where – chain growth probability, $k \le n$. The value p has the same physical meaning as the parameter α in formula (1). For a large number n the most probable value of the chain length k, as well as the dispersion σ of the distribution of the hydrocarbons in it, are calculated using the formulas: $\bar{k} = n \cdot p$ and $\sigma = \sqrt{np(1-p)}$.

We emphasize that all these conclusions relate to the products of the reaction of FT-synthesis.

Oil, hydrocarbon gases and natural bitumens. In fig. 2 shows the distribution of hydrocarbons in the Tengiz oil (Glebov, 2002). From this oil a gasoline fraction was previously extracted, which boiled up to 200°C and amounted to 41.6%. The higher temperature part of the oil was represented by paraffin and naphthenic hydrocarbons (41.4%), aromatic hydrocarbons and resins (16.9%), and asphaltenes (0.1%).

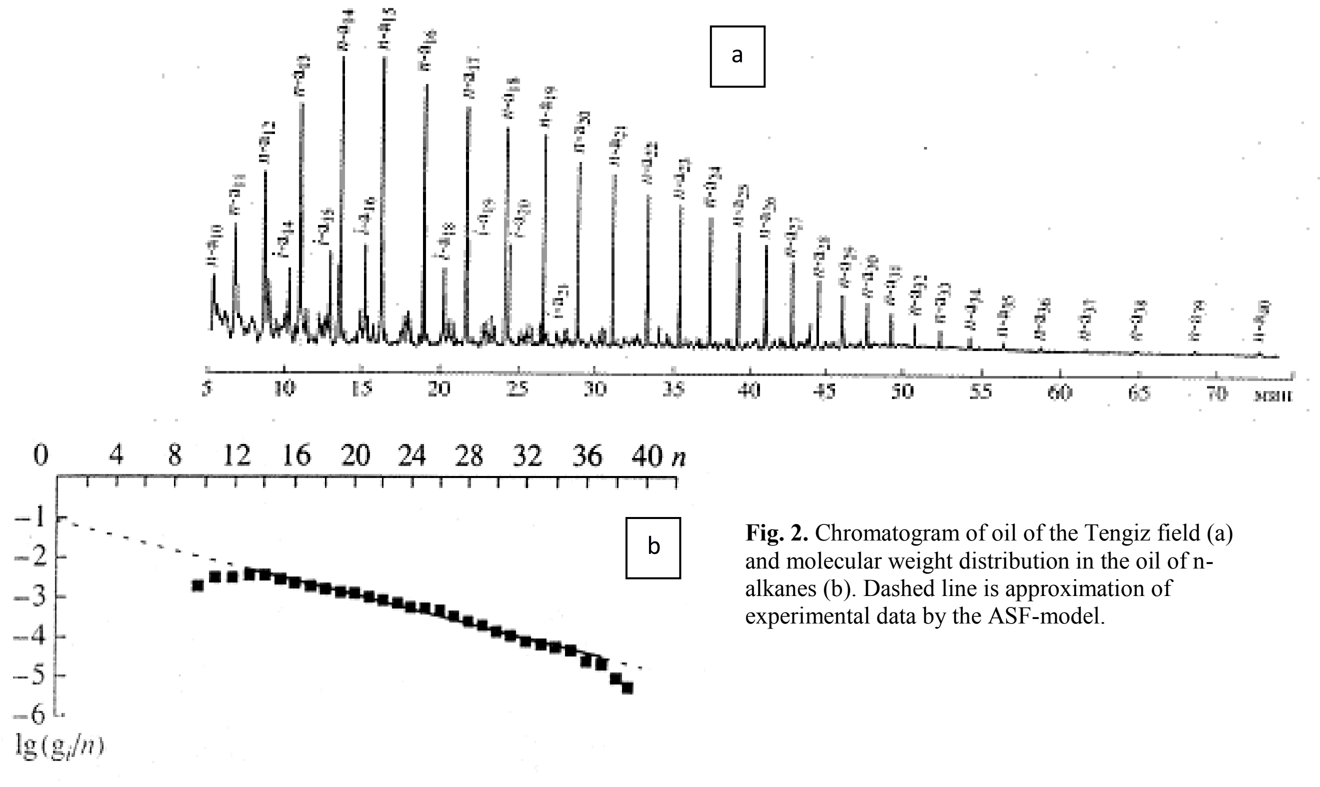

Fig. 2. Chromatogram of oil of the Tengiz field (a) and molecular weight distribution in the oil of n-alkanes (b). Dashed line is approximation of experimental data by the ASF-model.

We see that the n-alkanes of oil in the range $12 \leq n \leq 37$ ($C_{12}H_{26}$ – $C_{37}H_{76}$) fit well on a straight line. The parameter α, found from the tangent of the angle of inclination of this straight line to the abscissa axis (α_{tg}) и and calculated from the segment cut off by this straight line on the ordinate axis (α_{om}), are the same and equal to $\alpha_{tg} = \alpha_{om} = \alpha = 0.77 \pm 0.01$. Standard error of determination α less than 1% with a confidence level of 0,95. Deviation from a straight line is observed for hydrocarbons with the number of carbon atoms $n = 10 \div 12$ и $n = 38 \div 40$. This is due to the loss of paraffins in the release of paraffin-naphthenic fraction from oil. These losses are quite small. So the molecular mass distributions of n-alkanes of the Tengiz oil fully correspond to the classical model (1).

In fig. 3 as examples are given of the distribution of n-alkanes in oil, gas, and tar sands, borrowed from our works. In non-biodegraded oils, good agreement with the classical model is observed, and in gases and bitumens – with models of type 2 and 3 (see Fig. 1).

The distribution of hydrocarbons in oils and gases differ in the value of the parameter α. In gases, it is 0.4 – 0.6, and in oils it is $\alpha \geq 0.6$, and moreover, it has two meanings $\alpha = 0.63 \div 0.68$ и $0.77 \div 0.78$. The ASF-model explains this by the presence of two centers of growth of hydrocarbons chains with different reactivity on the catalyst. Bitumens are also characterized by two parameter values p. In this case, the first maximum of MMD corresponds to the number of chain-forming events $n = 22 – 26$, and the second one has a smaller amplitude $n = 31 – 35$ (Barenbaum, 2007).

Comparison of MMD of n-alkanes in non-biodegraded oils, bitumens and gases with hydrocarbon distributions in FT-synthesis products (Glebov, Klige, 1994) allows us to conclude (Barenbaum, 2007) that geosynthesis refers to the same type of polycondensation hydrocarbon synthesis, like the Fischer-Tropsch synthesis.

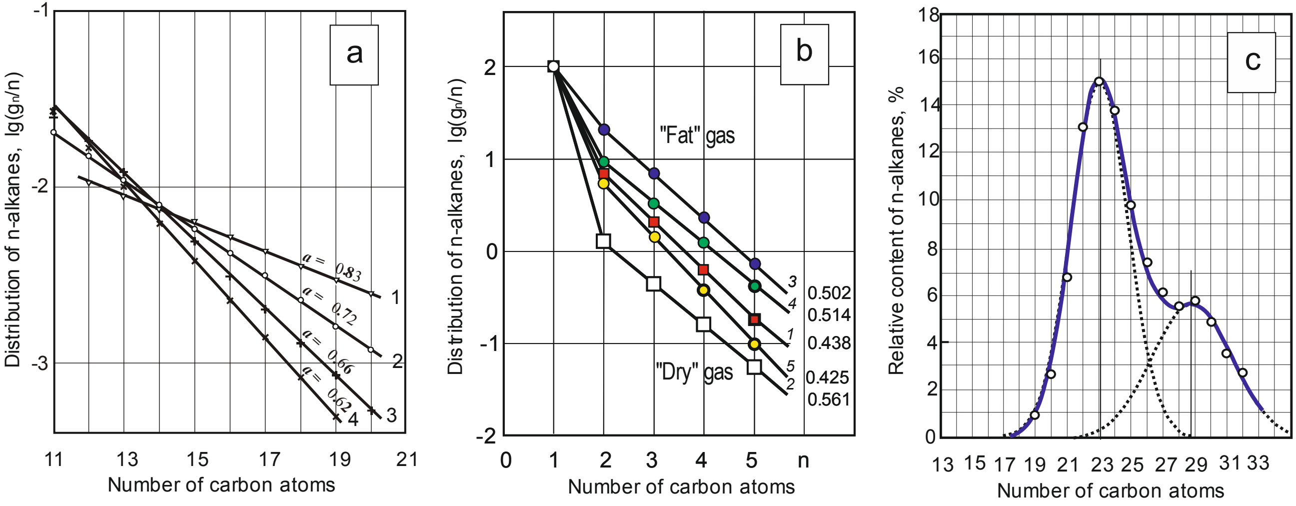

Fig. 3. Distributions of n-alkanes in: a) oils (Barenbaum, 2007); b) gases from the Vuktylskoye field (1–2) and obtained (3–5) in experiments (Klimov, 2017). The value of the parameter α is indicated near the distributions. All distributions are normalized to methane, taken as 100%; c) tar sands (Barenbaum, 2007). The chromatogram of bitumen is approximated by two maxima (dotted line), corresponding to formula (2)

Our research, however, shows (Barenbaum, 2007; Zakirov et al, 2013; Barenbaum, Klimov, 2015) that, unlike Fischer-Tropsch synthesis, the geosynthesis of oil and gas hydrocarbons is accompanied by the destruction of a large mass of groundwater and the formation of free hydrogen. These differences can be reflected in chemical formula of geosynthesis (Barenbaum, 2017, 2018), which is phenomenological in nature.

Chemical formula of geosynthesis. It is known (Rudenko, 1969) that in nature there is a sufficiently large number of catalytic reactions of polycondensation synthesis of hydrocarbons from carbon oxides (CO, CO_2) and hydrogen (H_2 and H_2O). Therefore, geosynthesis can also be attributed to such reactions. If we restrict ourselves to n-alkanes (C_nH_{2n+2}), which constitute the main part of the hydrocarbon of oil and gas, then they can be synthesized from CO, CO_2, H_2 and H_2O in various ways.

The most studied FT-synthesis process takes place in two ways:

$$nCO + (2n + 1)H_2 = C_nH_{2n+2} + nH_2O, \qquad (3)$$

$$2nCO + (n + 1)H_2 = C_nH_{2n+2} + nCO_2. \qquad (4)$$

Since 1935, the Fischer-Tropsch reaction has been used in industry for the production of synthetic oil. From other reactions of the synthesis of hydrocarbons can be noted the Kohlbel-Engelhardt reaction:

$$(3n + 1)CO + (n + 1)H_2O = C_nH_{2n+2} + (2n + 1)CO_2, \quad (5)$$

as well as the reaction:

$$nCO_2 + (3n + 1)H_2 = C_nH_{2n+2} + 2nH_2O, \quad (6)$$

where: n is the number of carbon atoms in the molecules of n-alkanes.

All these reactions are exothermic, accompanied by a large heat release. At the synthesis of methane (n = 1) under “standard” conditions (P =1 atm., T = 25°C), according to reactions (3) and (4), the heat effect (Gibbs energy) will be -158.8 and -170.8 kJ/mol, respectively, according to the Kelbel-Engelhardt reaction – -208.7 kJ/mol, and in the last reaction – -180.1 kJ/mol.

Typically, the synthesis is carried out using catalysts that dramatically increase the output of hydrocarbons. Many metals and their oxides can serve as such catalysts: Fe, Cu, Ni, Co, Mg, etc., which are part of sedimentary rocks, as well as the rocks themselves, represented by clays, aluminosilicates, etc. With increasing temperature, including due to the synthesis process (Storch et al, 1954), the output of hydrocarbons increases.

Unlike the reactions types: $CO+H_2$, $CO+H_2O$ and CO_2+H_2, the geosynthesis reaction – type CO_2+H_2O is endothermic and does not proceed under standard conditions. However, it becomes possible in a water-saturated mechanically activated mineral matrix of rocks (Discovery No. 326), when the synthesis is determined by free radicals, i.e. broken chemical bonds that are generated by intracrystalline defects in minerals. Moving to the surface of the rock matrix, the defects create an energy-saturated layer that reduces the Gibbs energy of chemical reactions. A necessary requirement is to create on the surface of minerals contacted with water recovering conditions under which H_2O decomposes, forming atomic hydrogen reacting with carbon oxides. At the same time, according to (Galkin, Lunin, 2005), water acts not only as a solvent, but also as a reagent and as a catalyst.

Experiments using catalysts from Fe (Zakirov et al, 2013) showed that the geosynthesis of n-alkanes by the reaction of CO_2+H_2O can be represented by two phenomenological chemical formulas:

$$nCO_2 + (n + \mu + 1)H_2O + \langle Fe \rangle = C_nH_{2n+2} + \mu H_2 + \text{æ}(FeO) + (3n + \mu + 1 - \text{æ})O, \quad (7)$$

$$nCO_2 + 2(2n + \mu + 1)H_2O + \langle Fe \rangle = C_nH_{2n+2} + (3n + 2\mu + 1)H_2 + \text{æ}(Fe\ O) + (3n + \mu + 1 - \text{æ})O, \quad (8)$$

where: n, m, æ are the stoichiometric coefficients, and the symbol “Fe” denotes the catalytic properties of the medium, which, during geosynthesis, fulfill the functions of not only a catalyst, but also an oxygen “sink”.

The Gibbs energy of reactions (7–8) in the synthesis of CH_4 under conditions of complete removal of free oxygen from the system (æ = 3n + m + 1) and the formation of various Fe-oxides indicates (Table 1), which, judging by the Gibbs energy (*ΔG*), geosynthesis can create the same or greater yield of n-alkanes than FT-synthesis.

Table 1. Gibbs energies in the synthesis of methane under standard conditions with the formation of different oxides of Fe.

Oxide	FeO	Fe_2O_3	Fe_3O_4	$Fe(OH)_2$	$Fe(OH)_3$	$FeCO_3$
ΔG, kJ/mol	-168	-228.8	-133	-77.6	-169.2	-116.4

Conclusion

1. The mechanism of geosynthesis is one of the varieties of a wide class of polycondensation reactions of hydrocarbon synthesis from oxides of carbon and hydrogen.

2. Unlike other reactions of this class, the phenomenological chemical formula of geosynthesis must necessarily take into account the catalytic properties of the geological environment.

References:

Barenbaum A.A. Study of oil production conditions using the theoretical model of Anderson-Schulz-Flory // Vestnik ONZ RAN, 2007, № 1 (25).

Barenbaum A.A. On the possible connection of gas hydrates with submarine groundwater // Vodnye resursy, 2007a. V.34, №5, pp. 620–625.

Barenbaum A.A. About the age of oil in deposits // Georesursy. 2017. V. 19. №1. pp. 30-37.

Barenbaum A.A. On the relationship between the processes of oil and gas formation and degassing with the decomposition of groundwater. // Georesursy, 2018, Vol. 20, No. 4, Part 1, pp. 290–300.

Barenbaum A.A., Ablya E.A. Molecular mass distribution of normal alkanes of oil as evidence of their polycondensation synthesis // Mater. III Ros. soveshchaniya: «Organicheskaya mineralogiya». Syktyvkar: Geoprint. 2009, pp. 74-77.

Barenbaum, A.A., Klimov, D.S. Experimental measurement of the rate of destruction of carbonized water during geosynthesis // Trudy VESEMPG-2015. Moscow: GEOKHI RAS. 2015, pp. 347–351.

Chersky N.V., Tsarev V.P. Mechanisms of synthesis of hydrocarbons from inorganic compounds in the upper horizons of the earth's crust // Doklady AN SSSR. 1984. V.279. № 3. pp. 730–735.

Chersky N.V., Tsarev VP, Soroko T.I., Kuznetsov O.L. Influence of tectonic and seismic processes on the formation and accumulation of hydrocarbons. Novosibirsk: Nauka. 1985, 224 p.

Chersky N.V., Melnikov V.P., Tsarev V.P. The phenomenon of the generation of hydrocarbons from extremely oxidized compounds of carbon and water // Doklady AN SSSR. 1986. V.288. №1,

Galkin A.A., Lunin V.V. Water in the sub- and supercritical states – a universal medium for chemical reactions // Uspekhi himii. 2005, V. 74, №1, pp. 24–40.

Glebov L.S. Molecular mass distribution of n-paraffins of Tengiz oil // Neftekhimiya. 2002, V.42, №2, pp.92–94.

Glebov LS, Kliger G.A. Molecular mass distribution of the products of Fischer-Tropsch synthesis // Uspekhi himii. 1994, V.63, №2, pp. 192–202.

Henrici-Olive G., Olive S. Chemistry of catalytic hydrogenation of CO. Moscow: Mir. 1987, 248 p. pp. 201–204.

Klimov D.S. Experimental studies of physicochemical phenomena involving CO_2 in filtration and metabolic processes. Abstract of the candidate dissertation of technical sciences. Moscow: OGRI RAS, 2015. 22 p.

Molchanov V.I. Experiments on the synthesis of hydrocarbons in the fine grinding of mineral substances in water // Doklady AN. 1967, T. 174, No. 5, pp.1185–1187.

Molchanov V.I., Gontsov A.A. Oil and gas formation modeling. Novosibirsk: UIGGM, 1992, 246 p.

Molchanov V.I., Selezneva O.G., Zhirnov E.N. Activation of minerals during grinding. Moscow: Nedra. 1988, 208p.

Opening № 326 of 04/21/1982: The phenomenon of organic matter transformation of sedimentary rocks under the influence of tectonic and seismic processes of the earth's crust. Auth .: Trofimuk A.A., Chersky N.V. Tsarev V.P., Soroko T.I.

Rudenko A.P. The theory of self-development of open catalytic systems. M .: MGU, 1969. 272 p.

Storch G., Golombik N., Anderson R. Synthesis of hydrocarbons from carbon monoxide and hydrogen. Moscow: Izdatel'stvo Inostrannoy literatury. 1954. 516 p.

Trofimuk A.A., Chersky N.V., Tsarev V.P., Soroko T.I. New data on the experimental study of the transformation of fossil organic matter using mechanical fields // Doklady AN SSSR, 1981, V. 257. No.1, pp. 207–211..

Zakirov S.N., Zakirov E.S., Barenbaum A.A., Klimov D.S., Lysenko A.D., Serebryakov V.A. Geosynthesis in the problem of the origin of oil and gas // Advanced technologies of development, enhanced oil recovery of deposits and well studies (domestic and world experience): Tr. VIII Mezhd. Tekhnologich. simpoziuma. Moscow: Institut neftegazovogo biznesa. 2013, pp.43–46.

Barenbaum A.A.[1], Shpekin M.I.[2] Origin of craters, mares and mascons on Moon in the light of the galactocentric paradigm UDC: 550.2: 523.4-1/-8

[1]*Oil and Gas Research Institute RAS, Moscow* (azary@mail.ru),
[2]*Kazan Federal University, Kazan* (michaels1@yandex.ru)

Abstract. Previously from the positions of the Galactocentric paradigm representations, the authors concluded that large craters and mares on the Moon, Mars and Mercury have a very young age and originated during one – three latest bombardments of the Solar System by galactic comets. In this paper we explain the size-distributions of lunar craters and mares by their creation by galactic comets. Craters with a diameter of more than ≈10 km are formed by falls of individual comets, while mares are the result of craters imposition from many comets falls. In the latter case, along with the heating and melting of lunar crust material, there is a melting and rise to the surface of large masses of more dense mantle substance, forming mascons.

Keywords: *Galactocentric paradigm; galactic comets; craters, mkares and mascons on Moon.*

Introduction. The surface of the Moon, Mars and Mercury, as is known, is almost entirely covered with craters and mares of impact origin. In the lunar mares with D> 218 km under a layer of basaltic lava there are clusters of mantle matter — the mascons, which create positive gravitational Bugue anomalies (Melosh et al, 2013; Neumann et al., 2015; Soderblom et al., 2015). Craters, mares and mascons on the Moon are believed to have been created by the fall of interplanetary space bodies. In the case of very large bodies, along with the formation of a crater and crushing of the crust material, melting and rising to the surface of large masses of heavier mantle matter occur. It is also believed that craters and mares existing on the Moon, Mars and Mercury overwhelmingly appeared in the time interval from 4.1 to 3.8 billion years ago during the so-called “late heavy meteorite bombardment” (Gomes et al., 2005).

These representations, however, face serious difficulties. The main explanation is the distribution of craters in size. This applies both to “continental” craters — on elevated areas of the surface (Fig. 1), and craters “mare” – on the surface of mares (Fig. 2). The first ones, the largest and morphologically more complex, are 1–2 orders of magnitude larger than the second ones, and their size distribution is more complex. It is not possible to explain the origin of these craters by the fall of cosmic bodies with a size distribution the same as that of the bodies of the modern asteroid belt (Woronov, 1977; Neumann et al., 2015).

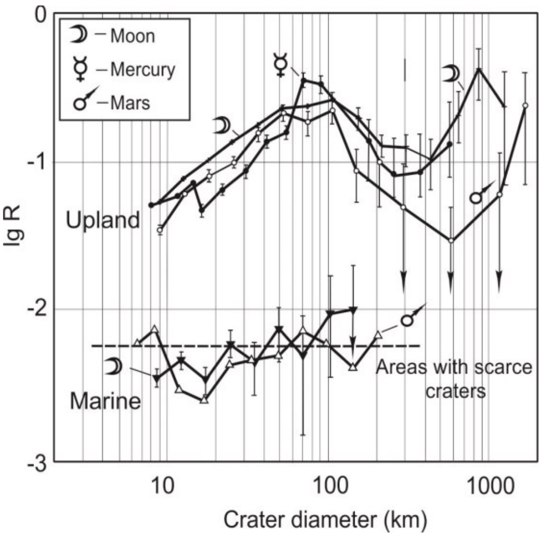

Fig. 1. Density of craters (Voronov et al., 1986) on the elevated portions of the Moon, Mars and Mercury (upper graph) and mares (lower graph)

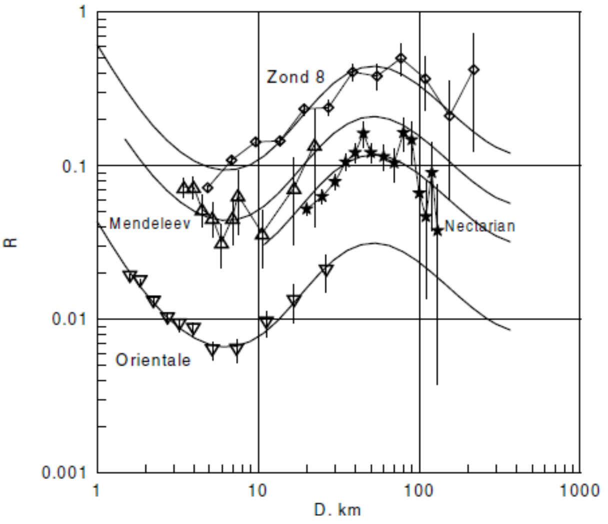

Fig. 2. Density of craters with a diameter from 0.01 to 200 km in mares of the Moon. Curves – theoretical description of the density of craters by the formula (1) (Neukum et al., 2001)

No less difficulty in explaining the origin of mare craters (Fig. 2). Their distribution is also very difficult. It is formally described by a polynomial (Neukum et al., 2001):

$$\log(N) = a_0 + \sum_{n=1}^{11} a_n \left[\log(D)\right]^n \qquad (1)$$

where N is the number of craters with a diameter > D appearing over a period of 1 billion years on an area of 1 km^2; a_o and a_n – constant coefficients, the values of which are determined from actual data.

Approximation (1) is used when estimating the age of the crater surface from the measured density of craters existing on it. This relationship is expressed by the formula (Neukum et al., 2001):

$$N(1) = 5.44\times10^{-14}\left(\exp(6.93T)-1\right)+8.38\times10^{-4}T \qquad (2),$$

where: N(1) is the number of craters with D > 1 km on an area of 1 km^2, T is the time of accumulation of craters in billion years.

Formula (2) was obtained under the following assumptions (Ivanov et al., 2001): 1) The density of craters on the Moon is closely related to the age of rock samples brought to Earth from Apollo landing sites; 2) the size distribution of crater bodies and their frequency of falls have been relatively stable over the past 4 billion years; 3) the size distribution of crater bodies in the first approximation can be taken as similar to the modern distribution of bodies in the asteroid belt; and 4) with increasing crater density, the age of the crater surface increases.

All 4 assumptions and formula (2) do not correspond to reality. The identification of the age of the Moon rock samples and the time of formation of the surface areas from which they are taken is a profound error (Barenbaum, Shpekin, 2011). Currently, in all sciences at the junction of the astronomical and geological fields of knowledge, a scientific revolution is occurring, caused by their transition to the concepts of the Galactocentric paradigm (Barenbaum, 2010, 2016, 2018). These ideas allow a new approach to solving the problems of individual sciences, including comparative planetology (Barenbaum, 2016).

We have developed a new approach to the interpretation of crater data on the basis of the Galactocentric paradigm (Barenbaum, 2015; Barenbaum, Shpekin, 2016, 2018, 2019), which, in our opinion, quite adequately explains the origin and size distribution of craters, mares and mascons on the Moon.

This article briefly introduces this approach and its results.

Galactocentric Paradigm. The galactocentric paradigm for the first time takes into account an important physical phenomenon – the jet outflow of matter from the gas-dust nuclear disk of spiral galaxies (Barenbaum, 2002), which has long escaped the attention of researchers. In accordance with its concepts, during the orbital movement of the Sun in the Galaxy, all the objects of the Solar System from time to time are subjected to intense bombardment by galactic comets. Comets arise in the zones of gas condensation (star formation) of galactic arms and enter the Solar System exclusively during periods when the sun and the spiral arms of the Galaxy intersect. Therefore, the fall of galactic comets on the planets has the character of “cometary showers” with duration of ≈1–5 million years, which recur in 20–37 million years. At the same time, after 150 million years, comets alternately bombard the southern and the northern hemispheres of the planets.

The last comet bombardment took time from 5 to 0.7 million years ago. The comets moved relative to the Sun at a speed of ≈450 km/s, consisted mainly of water ice with a density of ≈1 g/cm^3, had a diameter of 0.1 ÷ 3.5 km, a mass of ~10^{12} ÷ 10^{17} g and energy of ~10^{20} ÷ 10^{25} J. The distribution of comets in size obeyed the exponential dependencies, the fall density was 3–5 comets of all sizes over an area of 100×100 km^2, and their bombardment mainly occurred in the southern hemisphere of the planets.

Interaction of galactic comets with planets. At a speed of ≈450 km/s, galactic comets interact with planets differently (Barenbaum, 2015; Barenbaum, Shpekin, 2016) than interplanetary bodies (Melosh, 1989) falling onto planets with speeds of an order of magnitude smaller. The fall of galactic comets to the Earth is accompanied by the formation in the atmosphere of a narrowly directed hypersonic shock wave, which can penetrate deep into the lithosphere, causing strong heating of rocks up to depths of ≈300 km.

The high density of cometary falls also leads to the appearance in the lithosphere of large lenses of highly heated and partially melted rocks of the asthenosphere (Barenbaum, 2016a). Their formation on the Earth under the conditions of the “thick” lithosphere (continents) causes a significant rise in the surface of continents, and under the conditions of the “thin” lithosphere (oceans) leads to the outpouring of large quantities of basalt magmas to the ocean floor. In the intervals between the cometary bombardments, the lens substance cools down, and relaxation processes in the lithosphere level out the effects on the surface.

The outlined mechanism of interaction of galactic comets with planets applies to all the terrestrial planets, including the Moon. Depending on the combination of a number of conditions, such comets can create on the planets: craters, diatremes, lava covers, volcanoes, dome-shaped surface elevations, as well as crowns and monks (on Venus). The main factors for the formation of these structures are (Barenbaum, 2015): 1) the density of the gas envelope of the planet, 2) the thickness of the planetary lithosphere, 3) the composition and degree of heating of the rocks of the lithosphere, and 4) the frequency of falls of galactic comets.

New approach to the interpretation of crater data. We believe that the craters on the Moon, Mars and Mercury are formed by two different populations of cosmic bodies: 1) interplanetary asteroids and comets, and 2) galactic comets. The former are characterized by an inverse quadratic size distribution, and the latter are exponential. Therefore, craters and other impact structures resulting from their falls have size distributions of the same type as that of the cosmic bodies that created them.

Figure 3 shows the integral distributions of continental craters on the Moon, Mars, and Mercury (see Fig. 1), and Fig. 4 size distributions of lunar mares, and separately for the near and far side of the Moon. All graphs are given in semi-logarithmic coordinate system.

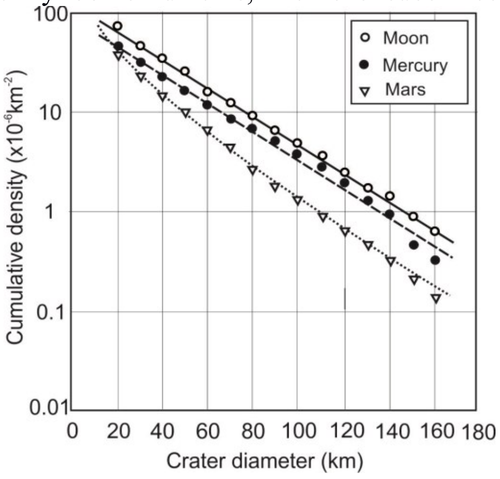

Fig. 3. Integral distributions over crater diameters on continental portions of the surface of the Moon, Mercury and Mars (Barenbaum, 2010)

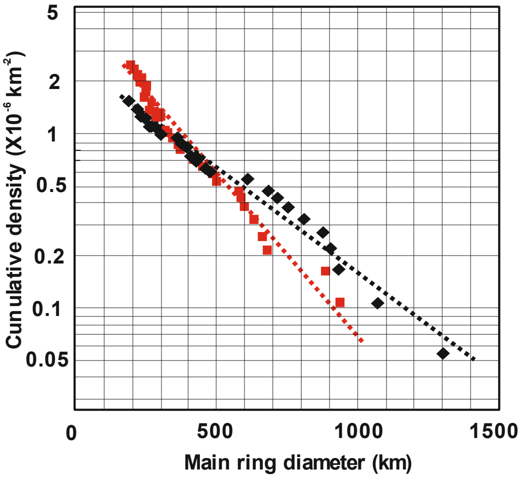

Fig. 4. Integral distributions of the mares by their diameters on the near (black icons) and far (red icons) side of the Moon (Neumann et al., 2015)

We see that the integral distributions over the diameters of large craters (Fig. 3) and lunar mares (Fig. 4) follow an exponential relationship: $N(D) = N(0)\exp(-\lambda D)$, where λ is a constant, and diameters vary within $a \leq D_i \leq b$. These dependences clearly indicate the formation of craters and mares by galactic comets. The distribution of craters on continents is characterized by the value $\lambda_{cr} = 3.3\times10^{-2}$ km^{-1}, and the mares on the near and far side of the Moon are $\lambda_{nm} = 1.923\times10^{-3}$ km^{-1} and $\lambda_{fm} = 2.857\times10^{-3}$ km^{-1}.

We explain the very existence of the mares on the moon by the threshold nature of their formation by comets. While the energy of comets transferred to the surface rocks is small and the cratering process develops, without going beyond the refractory anortosite crust of the Moon, comet incidence leads to multiple "plowing" of its surface, in which new craters level earlier emerged. It is shown (Barenbaum, 2010) that the continents of the Moon, Mars and Mercury are completely saturated with craters with a diameter of >10 km. Craters of smaller diameter are destroyed during the equilibrium process. The ultimate saturation of the surface with craters on the Moon, Mars and Mercury is almost the same and amounts to ≈100 craters D > 10 km over an area of 10^6 km^2. Such a density of craters, in principle, could only be ensured with the last bombardment of galactic comets from 5 to 0.7 million years ago. According to preliminary estimates, the density of their falls amounted to ≈3–5 comets of all sizes on an area of 100×100 km^2.

With such intense cometary bombardments on the Moon and Mercury, as well as having a very rarefied gas envelope of Mars, the craters craters from falling of many comets overlap. This leads to an increase in the diameter of the resulting crater and the heating of the underlying mantle rocks. At the same time, on the one hand, a large amount of lava appears, which floods the crater, turning it into a marine basin, and on the other, dense mantle rocks heat up and melt, which causes them to rise to the surface and lead to the appearance of positive Bugue anomalies over the mares.

Thus, the mares arise when craters overlap under conditions of high intensity of cometary falls, and the differences in the distribution of the mares on the far and near sides of the Moon are consequences of the different thickness of the refractory anorthosite crust on both sides of the Moon.

Since the fall of comets is a random process, it is possible to draw on probability theory, which operates with mathematical expectations, i.e. average values of random variables. In our case, these are the average diameters of craters $\overline{D}_{cr}$ and mares $\overline{D}_m$. Their values we find as:

$$\overline{D} = \frac{\int_{\alpha}^{b} De^{-\lambda D} dD}{\int_{\alpha}^{b} e^{-\lambda D} dD} = \frac{(\alpha + \lambda^{-1})e^{-\lambda\alpha} - (b + \lambda^{-1})e^{-\lambda b}}{e^{-\lambda\alpha} - e^{-\lambda b}} \qquad (3)$$

The parameters of distributions necessary for the calculation by the formula (3) will be taken from the graphs of Fig. 3 and 4. For craters we find ≈ 39 km, and for the mares on the near and far side of the Moon ≈520 km and ≈350 km. Assuming that the mares are formed by the imposition of craters from the falls of single comets, we conclude that on the near side of the Moon, the mares on average originated from falls of $k = \overline{D}_{nm}/\overline{D}_{cr} \approx 13$ comets, and on far side $\overline{D}_{fm}/\overline{D}_{cr} \approx 9$ comets. We explain these differences by the thicker thickness of the crust on the far side of the Moon compared to the near crust (Barenbaum, Shpekin, 2019).

This reasoning is general and therefore also applicable to mascons. With an increase in the number of crater overlaps, k, the thermal energy transferred to rocks increases, as a result, the volume of magmatic melts that form the basalt mares increases, and the depth of the magma chambers increases under the craters. Starting from the diameter of the mares D > 218 ± 17 km (Soderblom et al., 2015), this leads to the observed, almost proportional, growth of the Bugue anomalies over the mares.

Since during the formation of the mares, the density of cometary falls is k ≈ 11 ± 2 over an area of 100 × 100 km^2, cometary craters are necessarily present in the mares (see Fig. 2). According to Fig. 2 it is difficult to doubt that craters with diameters of 10 < D < 160 km are formed by comets and craters with D < 1 km – by asteroid bodies. With good statistics, which is hardly achievable for comet craters in the mares, they will show a distribution with the same slope as in Fig. 3, while craters from the fall of asteroid bodies will give an inverse quadratic dependence.

References:

Barenbaum A. A. Galaxy, Solar System, Earth. Subordinated Processes and Evolution, GEOS, Moscow: 2002, 353 p.

Barenbaum A. A. Galaxycentric Paradigm in Geology and Astronomy. Moscow: Librokom. 2010. 546 p.

Barenbaum A.A. On the scientific revolution in comparative planetology // Proceedings of Russian Annual Seminar on Experimental Mineralogy, Petrology and Geochemistry (RASEMPG – 2016). Moscow: GEOKHI RAS, 2016, pp. 82–83.

Barenbaum A.A. The formation of the asthenosphere by galactic comets as a new trend in tectonophysics // Tectonophysics and Topical Issues of Earth sciences. Conf. Proc.: Moscow: Institute for Earth Physics RAN. 2016, Vol.2(5), p.430–438. http://www.ifz.ru/lab_204/konferencii/chetvertaja-tk-2016/materialy-konf/

Barenbaum A.A. 2018 Space Sciences on the threshold of a change of scientific paradigms // Inzh. Fiz. 9, 30–47, doi:10.25791/infizik.09.2018.

Barenbaum A.A., Shpekin M.I. About age of the lunar surface // Vestnik Otdelenia Nauk o Zemle RAN, 2011, 3, NZ6011, doi:10.2205/2011NZ000141.

Woronov A., Strom R.G., Garkis M. Interpretation of the crater chronicle: from Mercury to Ganymede and Callisto // Satellites of Jupiter, edit. D. Morrison – Moscow: Mir. 1986. Vol. 2. pp. 5–48.

Barenbaum A.A. On the mechanism of energy dissipation of galactic comets bombarding terrestrial planets // Journal of Physics: Conf. Ser. 2015, 653, 012073, doi:10.1088/1742-6596/ 653/1/012073.

Barenbaum A.A. On the modern state of Comparative Planetology // 7-th Moscow Solar System Symposium Moscow. 2016. 7MS3-PS-65.

Barenbaum A.A., Shpekin M.I. To the development of the mechanism of interaction of galactic comets with the terrestrial planets // Journal of Physics: Conf. Ser.

2016, 774, 012096, doi:10.1088/1742-6596/774/1/012096.

Barenbaum A.A., Shpekin M.I. Problem of lunar mascons: an alternative approach // Journal of Physics: Conf. Ser. 2018. 946. 012079. doi:10.1088/1742-6596/946/1/012079.

Barenbaum A.A., Shpekin M.I. Origin and formation mechanism of craters, mares and mascons on the Moon // Journal of Physics: Conf. Ser. 1147, 2019, 012057. doi:10.1088/1742-6596/1147/1/012057

Gomes R., Levison H.F., Tsiganis K., Morbidelli A. Origin of the cataclysmic Late Heavy Bombardment period of the terrestrial planets // Nature, 2005, Vol. 435, Issue 7041. pp. 466–469. doi:10.1038/nature 03676.

Melosh H.J. Impact Cratering. A Geological Process. 1989. (New York: Oxford University Press Inc.)

Melosh H.J., Freed A.M., Johnson B.C., Blair *D.M.,* Andrews-Hanna J.C., Neumann G.A., Phillips R.J., Smith D.E., Solomon S.C., Wieczorek M.A., Zuber M.T. *The origin of lunar mascon basins // Science. 2013,* Vol. 340, Issue 6140, pp. 1552–1555. doi: 10.1126/Science. 1235768

Ivanov B. A., Neukum G., Wagner R. Size-frequency distributions of planetary impact craters and asteroids // Collisional Processes in the Solar System (eds.: H. Rickman and M. Marov), 2001, pp. 1–34. Kluwer, Dordrecht.

Neukum G., Ivanov B.A., Hartmann W.K. Cratering records in the inner Solar System in relation to the lunar reference system // Space Science Reviews, 2001. Vol. 96(1-4), pp. 55–86. doi: 10.1023/A:1011989004263.

Neumann G.A., Zuber M.T., Wieczorek M.A., Head J.W., Baker D.M.H., Solomon S.C., Smith D.E., Lemoine F.G., Mazarico E., Sabaka T.J., Goossens S.J., Melosh H.J., Phillips R.J., Asmar S.W., Konopliv A.S., Williams J.G., Sori M.M., Soderblom J.M., Miljković K., Andrews-Hanna J.C., Nimmo F., Kiefer W.S. Lunar impact basins revealed by Gravity Recovery and Interior Laboratory measurements // Science Advances. 1, 2015, e1500852, doi: 10.1126/sciadv.1500852

Soderblom J.M., Evans A.J. Johnson B.C., Melosh H.J., Miljković K., Phillips R.J., Andrews-Hanna J.C., Bierson C.J., Head J.W., Milbury C., Neumann G.A., Nimmo F., Smith D.E., Solomon S.C., Sori M.M., Wieczorek M.A., Zuber M.T. The fractured Moon: Production and saturation of porosity in the lunar highlands from impact cratering // Geophys. Res. Lett., 2015, 42, 6939–6944, doi:10.1002/2015GL065022

Woronov A. Crater saturation and equilibrium: A Monte Carlo simulation // J. Geophys. Res. 1977, Vol. 82, pp. 2447–2456.

Demidova S.I., Anosova M.O., Badekha K.A., Some evidence of the metasomatic activity in the lunar rocks. UDC 551.14:554.015.4

V.I. Vernadsky Institute of Geochemistry and Analytical Chemistry RAS, Moscow, Russia
(demidova.si@yandex.ru,m_anosova@mail.ru, ksenia_uimina@mail.ru,)

Abstract. Metasomatic processes are widespread on the Earth and might be possible on the Moon. Two mineralogical evidences of metasomatic activity in lunar material have been found in olivine fragments of Apollo 14321 lunar sample and gabbro-noritic anorthositic clast of Dhofar 301 lunar meteorite. The rock and mineral fragments are thought to be related to the high-Mg suite rocks (HMS). The presence of chains of inclusions of Ca-phosphate and zircelite/zirconolite in magnesian olivines of Apollo 14321 lunar sample suggests their possible formation during infiltration metasomatism with addition of incompatible elements. Unlikely fluid metasomatism with the participation of CO fluid could be responsible for the unusual high-Mg mineral association of the gabbro-noritic anorthosite clast of Dhofar 301 lunar meteorite.

***Keywords**: lunar rocks, lunar meteorites, lunar samples, lunar metasomatism.*

Metasomatic processes are widespread on the Earth and might be possible on the Moon. The search of mineralogical evidences of such processes involvement allows researching of its features and finding its relation to some types of the lunar rocks. High-Mg suite of primary lunar highland rocks is of special interest. The rocks are characterized by both high MG number of mafic silicates and high incompatible elements content. This enrichment is thought to be connected with high modal phosphate abundance. Its appearance in the primitive rocks may be related either to geochemical features of the parent melts or metasomatic processes.

Samples and methods. The thin sections of 14321 lunar sample and Dhofar 301 lunar meteorite were investigated in detail with standard optical microscopy methods. The chemical composition of the mineral phases was identified with Cameca SX-100 (Vernadsky Institute of Geochemistry and Analytical Chemistry RAS) under 15 kV voltage and 10 nA beam current. Some rare and major elements content in the olivines of 14321 sample were determined with LA-ICP-MS realized on Element-XR (Thermo Finnigan) mass-spectrometer with inductively coupled plasma and UP-213 (New Wave Research) laser system (Vernadsky Institute of Geochemistry and Analytical Chemistry RAS). All analysis are performed «in situ» in the thin sections. Laser beam size was 30 μm, frequency was 4 Hz. NIST 610 and ML3B glasses and MongOl Sh11-2olivine were used as external standards. Mg was used as an internal standard for the olivines, which were previously studied by the microprobe. The results were treated by Glitter and Isoplot programs. The analysis method details are published (Demidova et al, 2019).

Results. The «Big Bertha» 14321 rock sample (8998 g) was found near the Cone crater edge during "Apollo 14" mission. It is thought to be the fragment of Fra Mauro formation (Grieve et al., 1975). The sample is a breccia, containing the pieces of mare and non mare origin. Three components are present in the sample: 1) rounded fragments of a "dark" microbreccia, in which the fragments of the rocks and minerals are embedded into the fine-grained matrix; 2) a variety of low-Ti, high-Al mare basalts; 3) "light" matrix, in which the fragments of basalts and "dark" microbreccia fragments are dominant (Grieve et al., 1975). Microbreccia clasts contain fragments of various highland rocks varying in composition from dunites to felsites (Lindstrom et al., 1984; Belucci et al., 2019). Some large fragments of magnesian olivine Fo_{76-88} found in a dark microbreccia clast contain up to 0.4 wt.% P_2O_5, up to 0.2 wt.% Cr_2O_3. They are present in a fragment of olivine noritic anorthosite, in plagioclase-olivine intergrowth and as large mineral fragments (ranging in size from 40x60 to 280x400 microns). The associated pyroxene is represented by enstatite ($En_{87-88}Wo_{1-2}$), plagioclase – by anortite ($An_{94-96}Or_{0-1}$). Some fragments of olivine (Fo_{78-84}) contain tiny inclusions (<1 micron) located along cracks or form patches (Fig. 1). By laser ablation method it was determined that the inclusions are represented by calcium phosphate enriched in Y and REE and also by Zr-Ti phase, presumably zircelite or zirconolite. In addition, in the areas free of inclusions, these olivines are enriched in Zr, Hf, REE and Y (1-9xCI), but depleted in V, Co and Cr (0.01-0.1xCI).

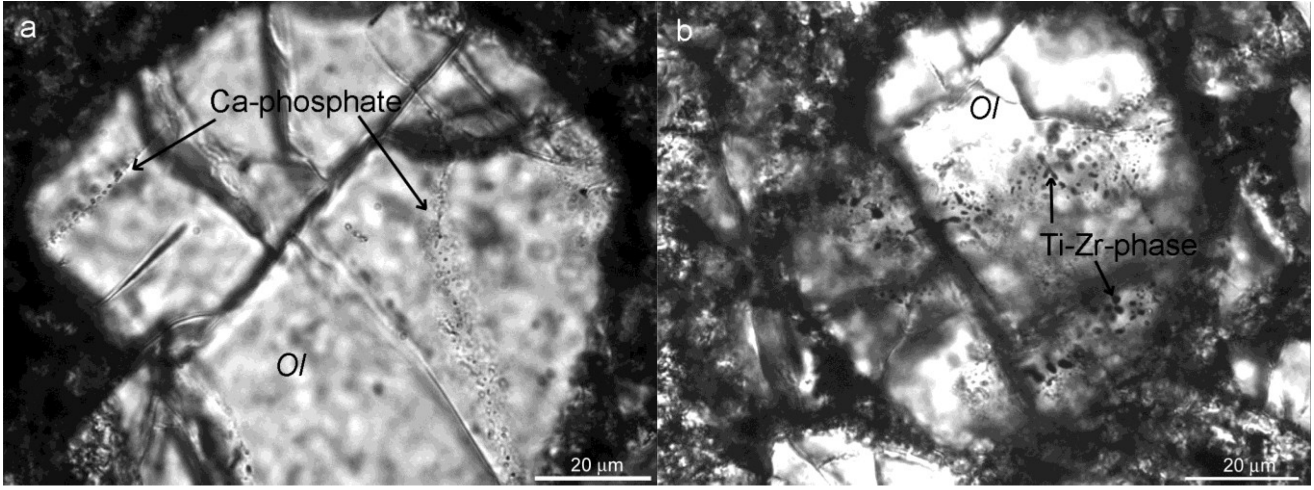

Fig. 1. Inclusions in olivine fragments of 14321 lunar sample: (a) Ca-phosphate, (b) Ti-Zr phase (BSE images).

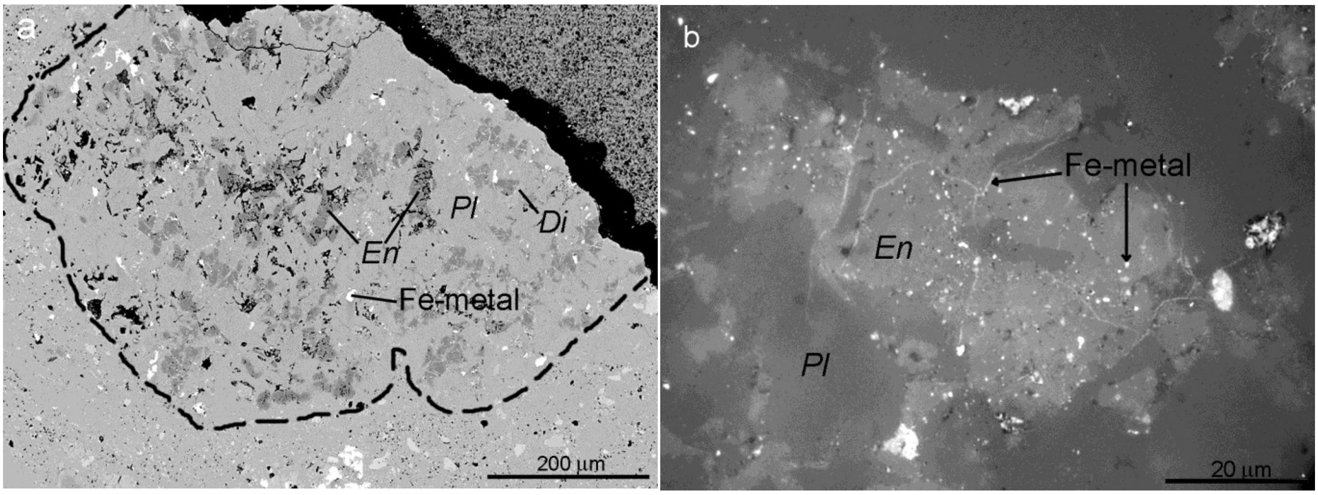

Fig. 2. Gabbro-noritic anorthosite fragment in Dho 301 lunar meteorite (BSE image) (a), tiny Fe-metal nuggets in enstatite grain of the clast (in reflected light) (б).

Dho 301 highland meteorite, which is supposed to be paired with Dhofar 025, 304, 308 meteorites, contain the fragment (0.4x0.5 mm) of gabbro-norite anorthosite (Nazarov et al., 2011). The rock consists of irregular plagioclase and interstitial pyroxene grains (Fig. 2a). In the latter, the smallest (about 1 µm) inclusions of iron metal not containing Ni are often observed. Sometimes they are concentrated along the cracks (Fig. 2b). The accessory phases are represented by Ca carbonate, troilite, Fe,Ni-metal and iron hydroxides. The latter sometimes contain Ni, S and less often Cr and Ti. Singular isolated silica phases, which seems to be associated with Fe,Ni-metal, are observed in the sample. Pyroxenes are represented by almost Fe-free magnesian species: enstatite ($En_{94-99}Wo_{1-3}$) and diopside ($En_{55-58}Wo_{42-44}$), containing mainly <0.2 wt. % FeO, <0.1 wt. % Cr_2O_3 and have a very low FeO/MnO ratio (1-4). Plagioclase is represented by anortite $An_{90-97}Ab_{3-10}$. In addition, there is a noticeable predominance of magnesium over iron.

Discussion. Previously, it was found that in 14321 sample the fragments of various highland rocks, varying in composition from dunites to granites, are confined to fragments of the most ancient component of breccia, clusts of so-called "dark" microbreccia, which are significantly enriched in REE (Lindstrom et al., 1972). Phosphorus-bearing olivines with unusual inclusions are revealed in one of these clusts. Most of the studied fragments of phosphorus-bearing olivines of 14321 sample have Mg-rich composition, are enriched in incompatible elements, but depleted in Co and Cr, which is typical for the primary highland HMS rocks. Warren and Lindstrom with coworkers suggested that the magnesian rocks from the Apollo 14 samples represented by dunite, troctolites and anorthosite surprisingly enriched in REE are interrelated and may represent fragments of layered intrusive complex of troctolitic composition (Warren et al., 1981; Lindstrom et al. 1984). The similarity of the chemical composition of P-bearing olivines and the associated phases of the 14321 sample with those of magnesian anorthosites and troctolites with high probability indicates their relationship.

In contrast, the origin of the gabbro-norite clust of Dho 301 meteorite is not so obvious. High MG number observed in this rock could not occur during the melt crystallization. Along with structural features it may indicate the metamorphic origin of the cluster. The depletion in Fe, Cr, Mn and low (non-lunar) Fe/Mn ratio in pyroxenes, low Fe/Mg ratio in plagioclases indicate that the rock has undergone a strong reduction during metasomatic processes. However, quite a high content of albite component in plagioclase suggests that the parent rock is not ferroanorthosite (FAN), but high-Mg suite rock (HMS).

It is believed that HMS rocks are the product of the early stage of the lunar crust formation after the primary differentiation, but the high content of incompatible elements does not correspond to their primitive composition (e.g. Shearer et al., 2015 and references therein). A number of researchers believed that this enrichment was a consequence of metasomatic processes in the lunar crust under the influence of fluids enriched in incompatible elements (Neal, Taylor, 1991; Shervais, Vetter, 1991). Alternatively, it was assumed that the high contents of these elements represent a characteristic feature of their parent magmas. To explain the enrichment of the sources with incompatible elements, various possibilities were considered, including the assimilation of KREEP material (see e.g. the review of Shearer et al., 2015 and references there).

The discovery of Ca-phosphate inclusions and Ti-Zr phases in some grains of Mg-rich olivine in the 14321 sample is surprising, since in the crystallization process these phases are not formed simultaneously. One of the possible explanations for such an association lies in the segregation of impurities during annealing after the crystallization of olivine from a melt rich in P, Ti, Zr, and REE, but such a process seems not possible due to the extremely slow diffusion rate of phosphorus. The characteristic arrangement of the inclusions along the chains or in some planes indicates that this mineralization is overlaid, and we apparently observe healed cracks in the olivine. Previously, similar chains of phosphate inclusions were observed in the plagioclase grains in 14305,400 lunar sample (Shervais, Vetter, 1991). In addition, discrete interstitial regions enriched in Ti, P, K (Grieve et al 1975; Neal, Taylor, 1991) were observed in the 14321 sample matrix. Thus, a possible explanation for the presence of such inclusions in the early phases is the infiltration of the impact melt rich in P, Zr, Ti and REE through an olivine-bearing rock. Alternatively, gas-phase metasomatic processes may be proposed. According to the latest isotope data, these processes were assumed to have been distributed on the visible side of the Moon 4 billion years ago (Potts et al., 2018). This implies that in the "Apollo-14" samples the part of phosphorus, and other incompatible elements could be brought in the course of the overlaid processes.

In contrast, another type of metasomatic process may be responsible for the formation of an unusual association of the gabbro-norite clast in Dho 301 meteorite and the tiny metal inclusions in the pyroxene of this clast. The pyroxene – Fe metal - silica association indicates the formation under highly reducing conditions in which iron is restored from pyroxene with the formation of Fe metal and the corresponding amount of silica phase. The absence of sulfides and aqueous phases may indicate CO participation as a reducing agent, according to the reaction: $FeSiO_3 + CO = Fe + SiO_2 + CO_2$ (Nazarov et al., 2011 and references therein)

Conclusion. The composition of the studied olivines and the associated phases of the 14321 sample and the mineral composition of the gabbro-norite anorthosite fragment of Dho 301 indicates relation to the HMS rocks. The secondary inclusions of calcium phosphate and zirkelite/zirconolite in the magnesian olivine of 14321 sample were probably formed during infiltration of the melt enriched in P, Zr, Ti, REE, which indicates the possibility of infiltration metasomatism in lunar HMS rocks. The mineral association of gabbro-norite anorthosite in Dhp 301 lunar meteorite suggests the possibility of fluid metasomatism involving CO fluid.

Acknowledgments: The study was partly supported by Russian Academy of Sciences (Program №28).

References:

Demidova S. I., Anosova M. O., Kononkova N. N., Brandstetter F., Ntaflos T. Phosphorus-Containing olivines of lunar rocks: sources and their localization in the lunar crust // Geochemistry. 2019 №8 (in press)

Bellucci J.J., Nemchin A.A., Grange M. et al. Terrestrial-like zircon in a clast from an Apollo 14 breccia // Earth and Planetary Science Letters. 2019. V. 510. P. 173–185.

Grieve R.A., McKay G.A., Smith H.D., Weill D.F. Lunar polymict breccia 14321: a petrographic study. Geochim Cosmochim Acta // 1975. V. 39. P. 229-245.

Lindstrom M.M., Duncan A.R., Fruchter J.S., et al. Compositional characteristics of some Apollo 14 clastic materials // Proc. Lunar Planet. Sci. Conf. 3rd. 1972. P. 1201-1214.

Lindstrom M.M., Knapp S.A., Shervais J.W., Taylor L.A. Magnesian anorthosites and associated troctolites and dunite in Apollo 14 breccias // Proc. Lunar Planet. Sci. Conf. 15th. J. Geophys. Res. 1984. P. C41-C49.

Nazarov M.A., Demidova S.I., Brandstätter F., Ntaflos T. Dhofar 301: Evidence for strong reduction in lunar highland rocks // Lunar Planet. Sci. Conf. 42. 2011. #1228.pdf.

Neal C.R., Taylor L.A. Evidence for metasomatism of the lunar highlands and the origin of whitlockite // Geochim. Cosmochim. Acta. 1991. V. 55. P. 2965-2980.

Potts N. J., Barnes J. J., Tartese R. et al. Chlorine isotopic compositions of apatite in Apollo 14 rocks: Evidence for widespread vapor-phase metasomatism on the lunar nearside ~4 billion years ago // Geochim. Cosmochim. Acta. 2018. V. 230 P. 46-59.

Shearer C.K., Elardo M.E., Petro N.E., et al. Origin of the lunar highlands Mg-suite: An integrated petrology, geochemistry, chronology, and remote sensing perspective // Amer. Miner. 2015. V. 100. P. 294–325.

Shervais J.W., Vetter S.K. Auto-metasomatism of the western lunar highlands: Result of closed system fractionation and mobilization of a KREEPy trapped liquid // Lunar Planet. Sci. 22nd. 1991. P. 1237-1238.

Warren P.H., Taylor G.J., Keil K. et al. Foraging westward for pristine nonmare rocks: Complications for petrogenetic models // Proc. Lunar Planet. Sci. Conf. 12th. 1981. P. 21-40.

Dunaeva A.N., Kronrod V.A., Kuskov O.L. Thermal flux in Titan for the different composition of chondritic substance.

V.I. Vernadsky Institute of Geochemistry and Analytical Chemistry RAS, Moscow (dunaeva.an@gmail.com)

Abstract. In this paper, the total radiogenic heat rates of different types of chondrites (L/LL and CI) were found to be equal to 5.14e-12 W/kg and 3.46e-12 W/kg, respectively. Based on these values, the heat fluxes of partially differentiated Titan composed of different types of chondritic substance were obtained. Calculations have shown that, depending on chondritic composition of rocky component, Titan's heat flux varies in the range of 3.65-5 mW/m^2. The corresponding structure parameters of the satellite are as follows: the outer icy shell thickness is 110-145 km, the depth of the internal ocean is 100-250 km, Love number k_2 values are 0.46-0.52.

***Keywords**: Titan heat flux, CI chondrites, L/LL chondrites.*

The heat flux of Titan (F) is an important parameter when studying the thermal evolution of the satellite and, moreover, it imposes certain constraints on the composition and structure of the satellite's internal regions. In particular, the heat flux determines the structure of Titan's water-ice shell, conditions for the internal ocean and rock-ice mantle existence, points to the applicability of the model of the satellite's partial differentiation. Since no direct instrumental measurements of the Titan heat flux has been carried out, the F value can be obtained on the basis of various mathematical models of thermal processes in the satellite interiors.

The most significant thermal processes occurring in Titan include the following: the gravitational differentiation of a substance by density, leading to the release of potential energy and its transfer to heat, phase transitions in a water-ice system, reversible chemical reactions of hydration/serpentinization (and counter reactions) accompanied by significant thermal effects, as well as tidal heating of the satellite and the radioactive decay, accompanied by release of thermal energy. The analysis of the intensity of those processes suggests that the main stage of the gravitational redistribution of Titan substance was completed at the period of ~ 500 Myr after CAI (Castillo-Rogez, Lunine, 2010) when Titan's rocky core was isolated inside initially homogeneous rock-ice satellite (Fig. 1). Chemical reactions and phase transitions in Titan are reversible due to convection in the satellite mantle and core; their thermal effects are opposite and mutually compensated. The tidal heating of Titan's interiors including ocean and solid tidal dissipation is much less compared to the radiogenic heating and is about 15% of the total energy arriving into Titan (Hay, Matsuyama, 2019; Sohl et al., 1995). Thus, radiogenic heating can be considered as the main thermal process in Titan with a minor energy contribution of tidal effects.

The Titan's silicate substance, as well as the substance of other large icy satellites of the Solar system, is modeled by ordinary (L/LL) or carbonaceous (CI) chondrites (Kuskov, Kronrod, 2001, 2005; Castillo-Rogez, Lunine, 2010). Therefore, the amount of radiogenic energy released in the satellite will be determined by the type of chondritic substance, namely, by concentration of radioactive elements in it and their radiation properties. The contents and radiation characteristics of the main radioactive isotopes (^{26}Al, ^{53}Mn, ^{60}Fe, ^{40}K, ^{232}Th, ^{235}U, ^{238}U) in L/LL and CI chondrites are presented in Tab. 1, 2.

Based on the Tab. 2 data, the radiogenic heat rate of chondritic substance for any given time $t$is calculated according to the formula:

$$H(t)=\sum_{i=1}^{7} H_{0i} e^{-\lambda_i t} .$$

The results of the calculations (Fig. 1) show that at present the radiogenic heat rates of L/LL and CI chondrites are equal to 5.14e-12 W/kg and 3.46e-12 W/kg, respectively.

The chondritic component' content in Titan depends on the chosen satellite model. In this paper, we consider the model of partially differentiated Titan which includes the outer water-ice shell (high pressure water ices + water ocean), rock-ice mantle and the central silicate core (Dunaeva et al., 2016). For this model, the maximum content of L/LL-chondritic component in the satellite is ~50 wt.% (Dunaeva et al., 2014). This permits to determine the value of L/LL chondritic radiogenic heat generated in Titan, which is equal to 4.15 mW/m^2 in terms of surface units. Taking into account the additional contribution of satellite tidal heating, the surface heat flux in Titan can be estimated as ~5 mW/m^2. Such heat flux, apparently, is the maximum value for the considered satellite model.

The minimum surface heat flux in Titan should not be lower than 3.1-3.3 mW/m^2 (Dunaeva et al., 2016, Kronrod et al., 2019), which follows from existence of the satellite's internal ocean, assumptions of outer icy crust conductivity and from Love numbers obtained for a given satellite model. Fig. 2 shows the main characteristics of partially differentiated Titan (thickness of icy crust Ih, depth of the ocean Hw, Love numbers k_2) for the different values of surface heat fluxes F (Kronrod et al., 2019). Theoretically, all satellite models should be located in the F range from 3.1-3.3 to 5 mW/m^2 and in the intervals of Ih, Hw, k_2 corresponding to this range. In this case, the intermediate values of heat fluxes are likely to arise as a result of hydration of the Fe-Mg-silicates (olivines and pyroxenes) contained in L/LL chondrites or in the case of mixed (L/LL+CI) chondritic composition of the rocky component.

Table 1 Content of the main radioactive isotopes in L/LL and CI chondrite**s.** [1] – (Braukmüller et al., 2018); [2] – (Wasson, Kalleymen, 1988); [3] – (Ruedas, 2017); [4] – (Nyquist, 2009); [5] – (Tang, Dauphas, 2015).

Element	element content in bulk chondrite		isotope	isotopic abundance at present, wt% [3]	initial isotopic abundance	initial isotope content in bulk chondrite, ppb	
	CI [1]	L/LL [2]				CI	L/LL
Al, mg/g	7.967	11.9-12.2	^{26}Al	0	^{26}Al/^{27}Al = $5.1\cdot10^{-5}$ [4]	402	608
Mn, mg/g	2.04	2.57-2.62	^{53}Mn	0	^{53}Mn/^{55}Mn = $9.1\cdot10^{-6}$ [4]	18.6	23.6
Fe, mg/g	182.348	185-215	^{60}Fe	0	^{60}Fe/^{56}Fe = $1.01\cdot10^{-8}$ [5]	1.69	1.85
K, µg/g	407	790-825	^{40}K	$1.1668\cdot10^{-2}$	-	823	1199.9
Th, ng/g	25.1	43	^{232}Th	100	-	36.36	53.91
U, ng/g	6.0	8.2	^{235}U	0.72045	-	5.22	8.28
			^{238}U	99.27955	-	16.53	26.21

Table.2. Characteristics of radioactive isotopes**.** λ_i - decay constant of i-th isitope; $T_{1/2}$ – half-life; H_{0i}, - initial (just after CAI) radiogenic heat rate of i-th isotope in bulk chondrite.

isotope	$T_{1/2}$, Myr	λ_i, yr^{-1}	initial specific heat production, W/kg of element [3]	H_{0i}, W/kg of chondrite	
				CI	L/LL
^{26}Al	0.717	9.68E-07	0.3583	1.44E-07	2.18E-07
^{53}Mn	3.7	1.87E-07	2.70E-02	5.01E-10	6.38E-10
^{60}Fe	2.62	2.64E-07	$3.6579\cdot10^{-2}$	6.18E-11	6.78E-11
^{40}K	1248	5.55E-10	$2.8761\cdot10^{-5}$	2.38E-11	3.45E-11
^{232}Th	14000	4.95E-11	$2.6368\cdot10^{-5}$	9.59E-13	1.42E-12
^{235}U	704	9.84E-10	$5.68402\cdot10^{-4}$	2.97E-12	4.71E-12
^{238}U	4468	1.55E-10	$9.4946\cdot10^{-5}$	1.57E-12	2.49E-12

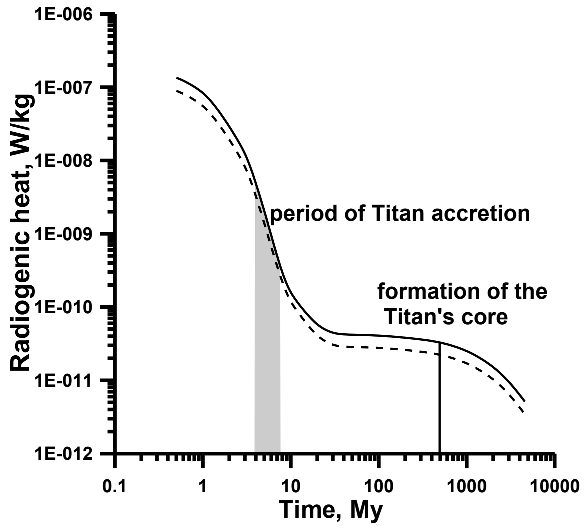

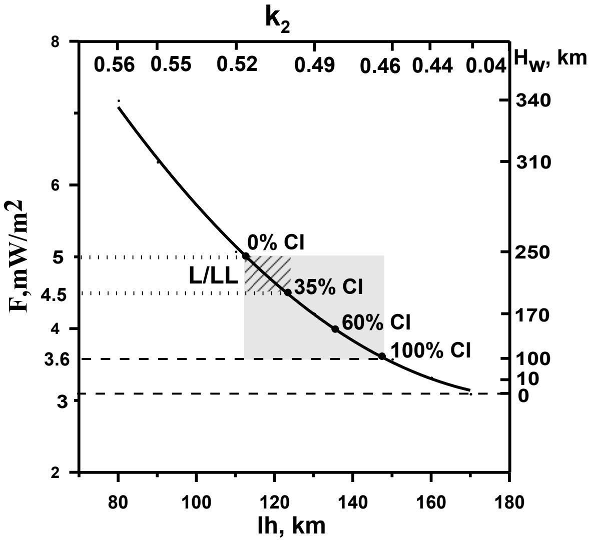

Fig. 1.Change of total radiogenic heat rate of different chondritic substances over geologic time.Solid lines – L/LL-chondrites, dotted lines – CI-chondrites.

Fig.2. Dependence of the main characteristics of partially differentiated Titan (H_{Ih}-H_w-k_2) on the satellite's heat flux and chondritic composition of the rocky component. Hatching - intervals of heat fluxes and corresponding values of H_{Ih}-H_w-$k_2$for Titan of L/LL-composition with varying degrees of hydration of the chondritic substance; The gray area marks allowable limits of F-H_{Ih}-H_w-$k_2$in Titan.

The processes of hydration of the L/LL-chondritic component of Titan can occur at different stages of satellite's formation and evolution and lead to formation of low-density water-containing silicates (serpentines, smectites) by serpentinization reactions. Hydrated minerals contain up to 14% of bounded water, which has a "diluting" effect on the radioactive isotopes concentration in the chondritic substance, that reduces its specific radiogenic heat rate, and hence the total heat flux in the satellite. Since in L/LL-chondrites the amount of silicates capable of hydration does not exceed 70% (McSween et al., 1991), this value can be considered the highest degree of silicate substitution by hydrous phases (hydration degree) in such type of chondrites. The calculations showed that at the maximum hydration degree of L/LL-substance (70%), the Titan heat flux will decrease to 4.5 mW/m^2, which satisfies the satellite's model in question (dashed area in Fig. 2). Thus, it can be concluded that the heat flux of Titan, formed by L/LL chondrites, is 4.5-5 mW/m^2 and leads to the formation of ice-Ih crust with a thickness of 110-125 km, an internal ocean of ~180-250 km; the Love number k_2 for such a model is in the range of ~0.5-0.52.

With the mixed chondrite composition of the rocky component, the heat flux is calculated from the relative proportions of the L/LL and CI components in the satellite's material. Fig. 2 shows the change in the Titan heat flux depending on CI component proportion. As can be seen from the figure, with a pure CI composition (CI-100%), the heat flux of the satellite is 3.6 mW/m^2, and this value should be considered as the minimum heat flux for the model of partially differentiated Titan. The thickness of the icy crust, corresponding to F = 3.6 mW/m^2, is 145 km, the depth of the ocean is 100 km, k_2 = 0.46. These results confirm the theory of existence of significant liquid volumes in Titan, since regardless of chondritic substance composition, the radiogenic and tidal energy produced by the satellite seems sufficient to maintain the internal ocean in a liquid state.

The results of performed calculations allow to formulate the following conclusions:

1. Radiogenic heat releases of L/LL- and CI-chondritic substances differ significantly and equal to 5.14e-12 W/kg and 3.46e-12 W/kg, respectively.
2. The heat flux of Titan composed of L/LL-substance is in the range of 4.5-5 mW/m^2; which corresponds to the thickness of the icy crust of 110-125 km and to the depth of internal ocean of ~180-250 km.
3. For CI-chondritic Titan, the heat flux is 3.6 mW/m^2, the corresponding ice crust thickness is 145 km, and the ocean depth is 100 km.
4. The mixed (L/LL+CI) composition of the satellite rocks leads to a heat flow in the range of 3.6–5 mW/m^2, the thickness of the ice crust is 110–145 km, the ocean depth is 100–250 km, k_2= 0.46–0.52. These resulting F-H_{Ih}-H_w-k_2 intervals are also the main constraints for the model of partially differentiated Titan.

Acknowledgements *This research was supported by the RFBR grant (№ 18-05-00685)*

References:

Dunaeva A., Kronrod V., Kuskov O. (2014). Models of Titan with rock-ice or hydrous silicate mantle. In European Planetary Science Congress 2014, EPSC Abstracts, Vol. 9, id. EPSC2014-663 (Vol. 9).

Dunaeva A.N., Kronrod V.A., & Kuskov O.L. (2016). Physico-chemical models of the internal structure of partially differentiated Titan. Geochemistry International, 54(1), 27-47.

Кронрод В.А., Дунаева А.Н., Гудкова Т.В., Кусков О.Л. Согласование моделей внутреннего строения частично дифференцированного Титана с данными гравитационного поля и хондритовым составом железокаменной компоненты. 2019, Труды ВЭСЭМПГ – 2019. (in Russian)

Braukmüller N. et al. (2018). The chemical composition of carbonaceous chondrites: Implications for volatile element depletion, complementarity and alteration. Geochimica et Cosmochimica Acta, 239, 17-48.

Castillo-Rogez J.C., Lunine J.I. (2010). Evolution of Titan's rocky core constrained by Cassini observations. Geophys. Res. Lett. 37, L20205.

Hay H.C., Matsuyama I. (2019). Nonlinear tidal dissipation in the subsurface oceans of Enceladus and other icy satellites. Icarus, 319, 68-85.

Kuskov O.L., Kronrod V.A. (2001). Core sizes and internal structure of the Earth's and Jupiter's satellites. Icarus, V. 151, 204-227.

Kuskov O.L., Kronrod, V.A. (2005). Internal structure of Europa and Callisto, Icarus, V. 177, 550–569.

McSween H.Y., Bennett M.E., Jarosewich E. (1991). The mineralogy of ordinary chondrites and implications for asteroid spectrophotometry. Icarus, 90(1), 107-116.

Nyquist L.E., Kleine T., Shih C.Y., Reese Y.D. (2009). The distribution of short-lived radioisotopes in the early solar system and the chronology of asteroid accretion, differentiation, and secondary mineralization. Geochimica et Cosmochimica Acta, 73(17), 5115-5136.

Ruedas T. (2017). Radioactive heat production of six geologically important nuclides. Geochemistry, Geophysics, Geosystems, 18(9), 3530-3541.

Sohl F., Sears W.D., Lorenz R.D. (1995). Tidal dissipation on Titan. Icarus, 115(2), 278-294.

Tang H., Dauphas N. (2015). Low 60Fe abundance in Semarkona and Sahara 99555. The Astrophysical Journal,802(1), 22.

Wasson, J.T., Kallevmen, G.W. (1988). Composition of chondrites. Philos. Trans. R. Soc. London A 325, 535–544.

Ivanov A.A., Sevastyanov V. S., Shnykin B.A., Dolgonosov A. A., Krivenko A.P., Priymak S.V., Roslyakova A. S., Galimov E.M. Self-organization of prebiological environment in the conditions of early Earth UDC 550.47

V.I. Vernadsky Institute of Geochemistry and Analytical Chemistry RAS, Moscow (aiva@geokhi.ru)

The question of non-occasional occurrence of the biological level of organization of matter remains controversial, because a deeper and more detailed understanding of causal relationship of the events is necessary, that took place during the self-formation of the conditions of early Earth that are favorable for the self-spawn of life. In this connection, knowledge of the sequence of reasons that contributed to building a real sequence of all factors that influenced the process is required. Today, it is known how geological events could develop, that formed the circumstances suitable for the spontaneous generation of life, under which the preparatory stage of abiogenesis, the stage of the formation of a primary aqueous environment with a different molecular mixture of organic and inorganic compounds passed. Therefore, there are no fundamental problems with the emergence of primary organic broth in the conditions of the early Earth, with the introduction of cosmogenic organic matter. Our research has shown that as a result of the thermobarocyclic mode of pneumatic impact arising from the action of surf waves, a multiphase bubble environment is formed in the caverns of the abrasive banks, contributing to the generation of polypeptide microspheres and the synthesis of high molecular weight organic compounds, anticipating the beginning of the shadow stage of structure of the first probionts. Therefore, the formation of abrasive coasts may be a key factor in abiogenesis.

Keywords: *abiogenic origin of life; polypeptide microspheres; probionts; thermobarocyclic mode; pneumatic impact; abrasive coasts; multiphase bubble environment.*

The self-organization of the prebiological environmental conditions begins with formation of a planetary system, which has a region that allows water to be in a liquid state. Liquid water is the main integral indicator representing the minimum number of parameters required for the conditions for biological activity.

It is believed that the water itself was already in the gas-dust cloud of the protoplanetary disk, and the necessary oxygen for its synthesis was formed in the depths of stars 1 billion years after the Big Bang. Then, during supernova explosions, oxygen was thrown into interstellar space, where water molecules formed in gas clouds. Therefore, pre-biological preparation of environmental conditions and the formation of the basis of the original substance of life - water, began long before the appearance of the Earth itself. At the same time, in the gas-dust cloud of the protoplanetary disk, the synthesis of organic compounds took place. With the formation of the Earth in the temperature zone, which allows the formation of a primary ocean on its solid surface, conditions emerged for the development of subsequent prebiological events. And first of all, it refers to the chemical change in the composition and properties of water, which occurs due to the dissolution of organic and inorganic substances in it. Due to the uniqueness of the properties of water and with the active participation of various kinds of energy effects, the transformation of the original environment continued not only in water but also on land. Water, saturated with organic compounds, accumulated in itself, the so-called organic broth, containing the component basis for the formation of prebiological structures. And the coastal part of land, under the action of the surf and waves of the primary ocean, was subjected to abrasion. The stage of natural self-organization of the process of formation of abrasive coasts probably predetermined the next important step towards fundamentally new environmental conditions of abiogenesis, which allowed to rise to a new level of prebiological development of events and move on to the stage of structural formation of protobionts. And here are the reasons. First, it required milder conditions, and second, softer sources of energy. Both of this can provide the cellular structure of the abrasive coasts, which can protect the protobionts from the sterilizing effect of hard cosmic radiation. Since the primary atmosphere of the Earth was oxygen-free, the reservoirs open to the Sun were exposed to the destructive action of UV radiation. But the rocky base of the abrasive banks served as a screen for the water that gets into the voids of the caverns during waving. In addition, in such conditions, under the stone screen, in the water in the caverns, containing organic broth, when the surf and the waves rolled, a pneumatic impact occurred (Ivanov, 2018). Water, working like a piston, instantly squeezed the air of the voids of the caverns, briefly heating it to hundreds of degrees. Under pressure, air aerated water containing organic broth, as a result of which polypeptides coagulated at the hot bubble boundary to form microsphere shells. As previously reported, polypeptide microspheres could be the first cell-like structure that initiated the formation of protobionts, since life begins with the cell and the cell with the membrane (Ivanov, 2018). At the same time, the cellular structure of the abrasive coasts is the main feature forming the generative conditions, in the active environment of which the polypeptide microspheres are forced to pulsate in time with the waves of the primary ocean. This is possible due to the thermobarocyclic mode of formation of a multiphase bubbly environment in the inner cavity of the caverns. Thus, being subjected to compulsory metabolism, microspheres, for a long geological time, were able to be modified to become protobionts. Probably, the shady environment of the caverns of the abrasive banks allowed them to develop and evolve to full-fledged living forms capable of independent ontogenesis. Then it becomes clear that the shadow stage of abiogenesis is the missing element of the theories of the origin of life. In connection with the above, the process of self-organization of the prebiological environment in the conditions of the early Earth should be considered in the direct relationship of combinations of the two stages of abiogenesis - light and shadow. The light stage is responsible for the prebiological synthesis of the structure-forming components of the living substance. The shadow stage organizes the structural abiogenesis of living matter. And this begins in the caverns of the abrasive banks under the action of the soft energy of the pneumatic impact, initiated by the shock of the waves of the primary ocean. Obviously, the generalization of abiogenesis occurred during the self-organization of the light and shadow stages under the conditions of the cellular structure of the abrasive banks. If this is so, then for abiogenic spontaneous generation of life on the early Earth, abrasive coasts are an indispensable attribute of the conditions of the prebiological environment.

It is possible that for the abiogenic origin of life, wherever the conditions for finding water in a liquid state arise in the Universe, one of the obligatory factors of the prebiological environment is the coastline with abrasive banks.

References:

Ivanov A.A., Sevastyanov V.S., Voropaev S.A., Dolgonosov A.A. Microscale processes of thermal coagulation of polypeptides during pneumatic impact // Goldschmidt2018, August 12-17, Boston, USA

Ivanov A.A., Sevastyanov V.S., Voropaev S.A., Dnestrovskiy A.Y., Galimov E.M. Experimental Modeling of Microsphere Formation Process in Organic Broth During Pneumatic Impact // Experiment in Geosciences – 2018 – Volume 24 – N 1

Ivanov A.A, Sevastyanov V.S., Dolgonosov A.A., Galimov E.M. Experimental model of genesis of protobionts // Goldschmidt2019, August 18-23, Barcelona, Spain

Kuyunko N.S., Alexeev V.A. A procedure of identifying extraterrestrial matter on the thermoluminescent characteristics. UDC 550.42

Vernadsky Institute of Geochemistry and Analytical Chemistry RAS, Moscow (AVAL37@mail.ru)

Abstract. According to the results of thermoluminescent studies of meteorites and samples-findings of unknown genesis, a procedure has been developed to establish the terrestrial or cosmic origin of the object under study. The mineral components of meteorites under the action of cosmic radiation accumulate traces of radiation disturbances, which cause thermoluminescent glow when heated substance. Comparison of thermoluminescent characteristics of the finding (intensity of luminescence, position of maximum and characteristic features of the luminescence curve) with those of meteorites of different chemical classes is used to establish the possibility of extraterrestrial origin of the found object. For meteorites, we have determined an area with a positive correlation dependence of natural thermoluminescence and thermoluminescence induced in laboratory conditions by x-ray radiation. Thus, for the test sample it is necessary to measure the natural and laboratory-induced x-ray thermoluminescence and by their ratio to determine belonging to the meteorite region. This paper presents thermoluminescent studies for a large group of meteorites and samples of unknown origin.

***Keywords**: thermoluminescence, meteorites, identification of extraterrestrial substance, samples-findings.*

Thermoluminescent method is successfully used for studying the substance of meteorites. Under the action of cosmic radiation, in addition to cosmogenic isotopes, traces of radiation disturbances accumulate in the mineral components of meteorites, which, when heated, cause a thermoluminescent glow. Measurements of natural thermoluminescence (stored by a meteorite in outer space) are used mainly to estimate the orbits of meteorites (Melcher, 1981), to analyze impact metamorphism, to estimate the terrestrial ages of meteorites (Akridge et al., 2000), to identifying environmental effects on the substance of a meteorite (Benoit et al., 1997) and for to identification of paired finds (Benoit et al., 1991). Induced thermoluminescence (induced from an external radioactive radiation source in the laboratory) reflects changes in the crystal structure of feldspar as a result of thermal or impact induced metamorphism. Induced thermoluminescence measurements are used to study the metamorphism of non-equilibrium ordinary chondrites (Sears et al., 1980), carbonaceous chondrites (Sears et al., 1991) and eucrites (Batchelor, Sears, 1991), to study the impacts (Batchelor, Sears, 1991), to study the impact-thermal history of meteorites, to determine the impact class and the magnitude of the shock pressure of equilibrium chondrites (Ivliev et al., 2007).

This work proposes a procedure for identifying extraterrestrial substances by thermoluminescent characteristics. The assumption of the use of the thermoluminescence method for the identification of extraterrestrial matter arose in the study of three samples taken from the site of the fall of the Kosice H5 meteorite, Slovakia (Kuyunko et al., 2015a). The value of natural thermoluminescence for one sample turned out to be 40 times higher than for the other two, whose luminescence intensity approached the background value. The shape of the luminescence curve of these samples is not typical of meteorites. Therefore, we assumed that, highly likely, these samples are terrestrial matter, while the third sample with a high intensity of thermoluminescent glow is a fragment of a meteorite.

The past three years, we have measured the natural thermoluminescence and thermoluminescence induced by laboratory x-ray radiation for a large group of meteorites of various chemical classes and samples-findings from the population of unknown genesis in order to establish the criteria for identifying substances of extraterrestrial origin using the thermoluminescence method. Samples were selected by A.YA. Skripnik.

To study the gross samples of meteorites and samples of unknown origin weighing 0.7-1.0 g were crushed and ground in a jasper mortar under a layer of ethyl alcohol. After drying for 24 hours, the magnetic fraction was separated by a manual magnet in air. Three samples of 2 mg each were prepared from the non-magnetic fraction of each test sample by the quartering method. Each sample was placed in a 6 mm diameter beryllium foil cup and evenly distributed on the bottom with a drop of acetone under the binocular. The solvent was removed by air drying for 24 hours. Thermoluminescence was recorded on a modified laboratory unit. The interface, made on the basis of the L-154 board, made it possible to register the photomultiplier current (FEU-93) and sample heating temperature on the computer. Discreteness of registration was 1 °C.

Previously, we (Kuyunko et al., 2015b) measured the thermoluminescence induced by X-rays when developing the methodology for determining the petrological subtype of nonequilibrium ordinary chondrites. The luminescence curve was approximated by a Gaussian curve, and the thermoluminescence intensity was determined over the total area and in different temperature ranges. Our calculations showed the consistency of the results both using the peak height and area in different temperature ranges of the Gaussian curve, and using the original thermoluminescence spectrum.

In this investigation the calculations of the parameters of thermoluminescence were carried out from the initial spectra. The average value of three measurements was used to calculate the thermoluminescence parameters. The intensity of natural and X-ray induced thermoluminescence in the laboratory was from determined from the area under the peak of the decay curve in the temperature range 50–350 °C. All thermoluminescence values were determined in relative units by normalization to the corresponding thermoluminescence values of Dhajala H3.8 chondrite. The results of thermoluminescent studies of meteorites and samples of unknown genesis are presented in Tables 1 and 2. It should be noted that for samples of unknown origin, the characteristics of the thermoluminescence spectra — the position of the peak maximum, its width, the shape of the curve significantly differ from the corresponding characteristics of Dhajala chondrite and other meteorites. In the range of 50–350 °C, the natural thermoluminescence spectra of all these samples do not have a clearly pronounced maximum — the luminescence intensity increases with increasing temperature.

The figure shows the ratio of natural and x-ray induced in the laboratory thermoluminescence for meteorites and samples of unknown origin. For meteorites, a region with positive correlation dependence was identified by the ratio of the natural and induced thermoluminescence. Several meteorites were out of this area. These are meteorites with a small perihelion value (like Malakal L5), which lost of natural thermoluminescence due to sun heating, as well as chondrites found in deserts (Dhofar 022 H3.9 and Dhofar 024 H3.9), that lost their natural thermoluminescence due to partial annealing due to their contact with heated sand. Samples of unknown genesis to this area do not apply. For them, the value of natural thermoluminescence is significantly lower than the value expected for the measured x-ray induced thermoluminescence values in these objects, with compared for meteorites data. Two samples are located on the border of the meteorite area, they are characterized by higher values of natural and x-ray induced thermoluminescence. However, the shape of the spectrum of natural thermoluminescence does not allow attributing them to objects of cosmic origin. Higher values of natural thermoluminescence can be due to their technogenic origin, and a significant content of feldspar that led to an increase the intensity of laboratory-induced thermoluminescence.

Thus, the algorithm for identifying samples-findings of unknown genesis is reduced to measuring the natural and x-ray induced TL according to the above method and determining their ratio and their relation to the region of meteorites. The shape of the TL spectrum, the position of the peak maximum, and its width are additional arguments for the identification of samples of extraterrestrial origin.

Table 1. Normalized to chondrite Dhajala H3.8 values of natural (TLnat.) and induced by x-ray radiation under laboratory conditions (TLind.) thermoluminescence in the ordinary chondrites.

№	Meteorites	TLnat.	TLind.	№	Meteorites	TLnat.	TLind.
1	Bogoslovka, H5	0.849	0.723	26	Khmelevka, L5	0.076	0.587
2	Borodino, H5	3.273	1.489	27	Tsarev, L5	0.366	0.400
3	Vengerovo, H5	3.864	1.031	28	Chelyabinsk, LL5	23.508	2.055
4	Gorlovka, H3.7	0.269	0.058	29	Ausson, L5	2.831	2.464
5	Doroninsk, H6	6.170	1.867	30	Barwell, L5	21.417	4.603
6	Elenovka, L5	1.873	2.478	31	Bjurbole, L/LL4	6.830	1.303
7	Erofeevka, H4	0.066	0.254	32	Chainpur, L3.4	0.083	0.041
8	Zhovtnevyi H6	3.241	1.657	33	Chantonnay, L6	0.101	0.033
9	Kargapole, H4	1.324	0.752	34	Dalgety Downs, L4	0.286	0.525
10	Kirishi, L4	4.761	1.786	35	Dengli, H3.8	0.492	0.338
11	Kunashak, L6	3.450	1.572	36	Dhofar 022, H3.9	0.037	0.300
12	Manych, LL3	0.222	0.058	37	Dhofar 024, H3.9	0.103	0.497
13	Markovka, H4	0.214	0.243	38	Dimmitt, H3.7	0.025	0.130
14	Mordvinovka, L6	1.605	1.363	39	Grady (1937), H3.7	0.446	0.528
15	Nikolskoe, L4	13.188	3.492	40	Khohar, L3.6	0.153	0.189
16	Odessa, H4	0.203	0.546	41	Kilabo, LL6	1.864	2.184
17	Orlovka, H5	0.828	0.378	42	Kosice, H5	0.701	2.279
18	Pervomaisky, L6	0.132	0.028	43	Kyushu, L6	0.805	0.153
19	Petropavlovka, H4	0.357	0.247	44	Leedey, L6	21.944	4.645
20	Pultusk, H5	1.610	1.017	45	Malakal, L5	0.030	0.288
21	Raguli, H3.8	1.265	0.881	46	Mezoe-Madaras, L3.7	1.447	0.404
22	Rakity, L3	0.511	0.249	47	Pribram, H5	2.931	1.058
23	Sevrukovo, L5	0.130	0.139	48	Sayh al Uhaymir 089, L/LL3.6	0.638	0.245
24	Slobodka, L4	1.994	1.222	49	Tugalin-Bulen, H6	3.047	3.780
25	Stavropol, L6	14.271	2.814	50	Weston, H4	1.668	0.683

Table 2. Normalized to chondrite Dhajala H3.8 values of natural (TLnat.) and induced (TLind.) thermoluminescence in the findings of indeterminate genesis.

Sample	Characteristic of sample	TLnat.	TLind.
P15	Weathered granite	1.935	3.064
P39	Metamorphic rock - shale with amphibole and quartz	0.0037	2.5
P22	Silicate glass with plagioclase microlites, metal globules and inclusions	0.0074	0.94
P16	Magmatic rock	0.0067	0.36
P82	Granite-type rock with amphibole, biotite, plagioclase, quartz	0.043	0.20

Sample	Characteristic of sample	TLnat.	TLind.
P25	Type gabbro diabase (was found at a depth of 2.5 m in permafrost)	0.035	0.065
P94	Fine-grained gabbroid with whitish crust of weathering	0.003	0.044
P292	Metasomatic rock with pyroxene, medium granular	0.0054	0.033
P60	Silicate glass with skeletal crystallization	0.007	0.021
P293	Metasomatic rock with pyroxene and corundum	0.0051	0.018
P23	Vitreous silicate slag	0.004	0.015
P28	Zoned colored quartzite	0.0040	0.015
P5	Igneous rock with a microophyte structure and quartz tonsils	0.0067	0.014
P291	Metasomatic rock with pyroxene, coarse	0.048	0.013
P14	Mica Shale	0.005	0.011
P97	Breed type gabbroid with oxidized crust	0.010	0.008
P32	Ferrous siltstone with quartz inclusions	0.004	0.006
PS	Aluminosilicate slag	0.009	0.004
Gd	Godziecina (Poland), rock	<0.002	0.0018
P1	Ferrous quartzite	0.0005	0.0014
P31	Type of diabase. Oxidized.	0.005	0.001
P8	Graphite slate with silicate interlayer	<0.002	0.0004

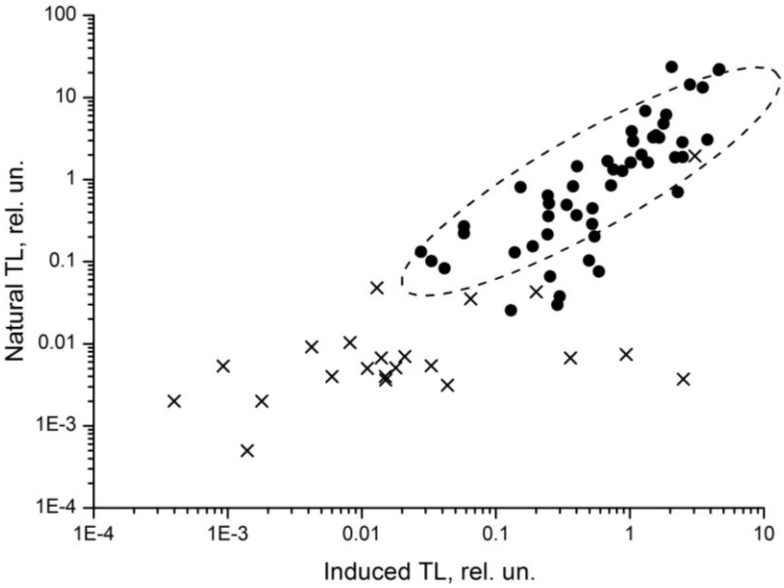

Fig. The ratio of the natural and x-ray induced thermoluminescence in chondrites (circles) and in samples of uncertain origin (crosses).

The work is partially supported by the Program No. 28 of the Presidium of Russian Academy of Sciences.

References:

Akridge J.M.S., Benoit P.H., Sears D.W.G. Terrestrial age measurements using natural thermoluminescence of a drained zone under the fusion crust of Antarctic ordinary chondrites // Meteoritics Planet. Sci. 2000. V. 35. N 4. P. 869-874.

Batchelor J.D., Sears D.W.G. Metamorphism of eucrite meteorites studied quantitatively using induced thermoluminescence // Nature. 1991. V. 349. P. 516-519.

Benoit P.H., Sears H., Sears D.W.G. Ice movement, pairing and meteorite showers of ordinary chondrites from the Allan Hills // Meteoritics. 1991. V. 26. N 4. P. 317-328.

Benoit P.H., Arcridge J.M.C., Sears D.W.G. et al. The weathering of Antarctic meteorites: climatic controls on weathering rates and implications for meteorite accumulation // Lunar Planet. Sci. 1997. V. 28. Houston: LPI. P. 95-96.

Ivliev A.I., Alexeev V.A., Kuyunko N.S. Research of the shock metamorphism of ordinary chondrites by the thermoluminescence method // Lunar Planet. Sci. 2007. V. 38. Houston: LPI. CD #1043.

Kuyunko N.S., Ivliev A.I., Alekseev V.A. Determination of the degree of metamorphism of ordinary nonequilibrium chondrites by the thermoluminescent method // Proceedings of the All-Russian Annual Seminar on Experimental Mineralogy, Petrology and Geochemistry. Moscow, April 21-22, 2015. Moscow: GEOKHI RAS. 2015a. N 1. P. 293-296.

Kuyunko N.S., Skripnik A.Ya., Alekseev V.A. Identification of extraterrestrial matter by the thermoluminescent method // Proceedings of the XVI International Conference "Physicochemical and Petrophysical Research in Earth Sciences", September 28. - 1 October. 2015, Moscow: IGEM RAS. 2015b. P. 144-147.

Melcher C.L. Thermoluminescence of meteorites and their orbits // Earth Planet. Sci. Lett. 1981. V. 52. N 1. P. 39-54.

Sears D.W.G., Grossman J.N., Melcher C.L., et al. Measuring metamorphic history of unequilibrated ordinary chondrites // Nature. 1980. V. 287. N 5785. P. 791-795.

Sears D.W.G., Batchelor J.D., Lu J., Keck B.D. Metamorphism of CO and CO-like chondrites and comparison with type 3 ordinary chondrites // Proc. NIPR Symp. Antarct. Meteorites. 1991. V. 4. P. 319-343.

Lavrentjeva Z.A., Lyul A.Yu. A comparative study of trace element concentration in heavy and light fractions from Adhi Kot EH4 enstatite chonrite. UDC 552.63

V.I. Vernadsky Institute RAS, Moscow (lavza@mail.ru).

Abstract. Based on the study of the features of lithophile and siderophile trace element distributions in the density separated grain-sized fractions from Adhi Kot EH4 enstatite chondrite a conclusion has been made that these peculiarities probably result from mixing effects of nebular fractionation, thermal metamorphism and shock.

Keywords: *mineral fractions; trace element distributions; enstatite chondrites.*

Among known planetary materials, enstatite chondrites (EC) are truly a breed apart. They are highly reduced, with < 1 mol percent FeO in their silicates, in contrast to other chondrites as well as Earth, Mars, and Venus, which have FeO contents in the 10 - 40% range [Hertogen et al., 1983]. Enstatite chondrites are formed in highly reducing environment. This inference is supported by the high Mg/(Mg + Fe) of olivine and pyroxene, presence of Si in Fe,Ni metal, and occurrence of typically lithophile elements, such as Ca, Mg, Mn and K, in sulfide minerals in enstatite chondrites [Weisberg et al., 2009]. The fO_{2s} inferred typical EC mineral assemblages (pure En, Si-bearing metal, Mg-sulfides) are several orders of magnitude below those of a system of solar composition [Grossman et al., 2008]. Relative to ordinary chondrites and most carbonaceous-chondrite groups, EC are enriched in volatile and moderately volatile elements. EC (particularly, EH chondrites) are enriched in five geochemical classes of volatile and moderately volatile elements – siderophiles, chalcophiles, alkalis, halogens and nitrogen. This enrichment reflects the composition of the gas in the nebular region where EC formed. The local gas was reducing and may have had high C/O and/or high PH_2 /H_2O ratios relative to gas in other nebular regions (Rubin, 2008). EC are divided into two main groups, EH and EL, based on high and low abundances of Fe,Ni metal: both groups show a metamorphic sequence from type 3 to 6 similar to that observed in ordinary chondrites [Baedecker and Wasson, 1975; Sears, 1980].

This work reports data on the composition of density separated grain-sized mineral fractions on the Adhi Kot EH4 enstatite chondrite which are considered from the viewpoint of cosmochemical history of EH chondrites. The main aim of our study is to estimate better the genesis of EH chondrites from studying the trace element distribution in individual mineral phases.

Samples and methods

Keil [Keil, 1968] reported that the Adhi Kot meteorite contains 68 wt % silicate, 23 wt % metal, 6 wt % troilite, 1 wt % schreibersite, 1 wt % niningerite, 0.9 wt % oldhamite and 0.15 wt % graphite. The Adhi Kot EH4 enstatite chondrite breccia consist of silica-rich clasts (12+5 vol %), chondrule-rich clasts (55+10 vol %) and matrix (35+10 vol %). The silica – rich clasts are new kind of enstatite chondritic material, which contains more cristobalite (18 – 28 wt %) than enstatite (12 – 14 wt %), as well as abundant niningerite and troilite [Rubin, 1983]. Cristobalite occurs as anhedral grains (<30 μm) in both matrix and clasts. Large rounded grains of cristobalite inside kamacite clasts are associated with clinoenstatites. Pyroxenes are set in a fine-grained matrix and in the metal clasts enclosed euhedral laths and also subhedral to anhedral grains [Leitch, 1982].

We studied the density separated grain-sized fractions from Adhi Kot EH4 enstatite chondrite. The mineral fractions were isolated by handpicking under microscope and by physical separation methods. The elemental composition of fractions was analyzed at the Central Laboratory of GEOKHI RAS using optimized version of neutron–activation analysis developed for analyzing extraterrestrial material [Kolesov, 2001].

Results and discussion

Under consideration are peculiarities of elemental composition of heavy and light nonmagnetic grain-sized fractions extracted from Adhi Kot EH4 enstatite chondrite. The analysis of the chemical composition of the obtained data in fractions A, B, C, D, with ($\rho > 4.18$ g cm^{-3} (most part troilite), extracted from unequilibrated Adhi Kot EH4 enstatite chondrite showed that:

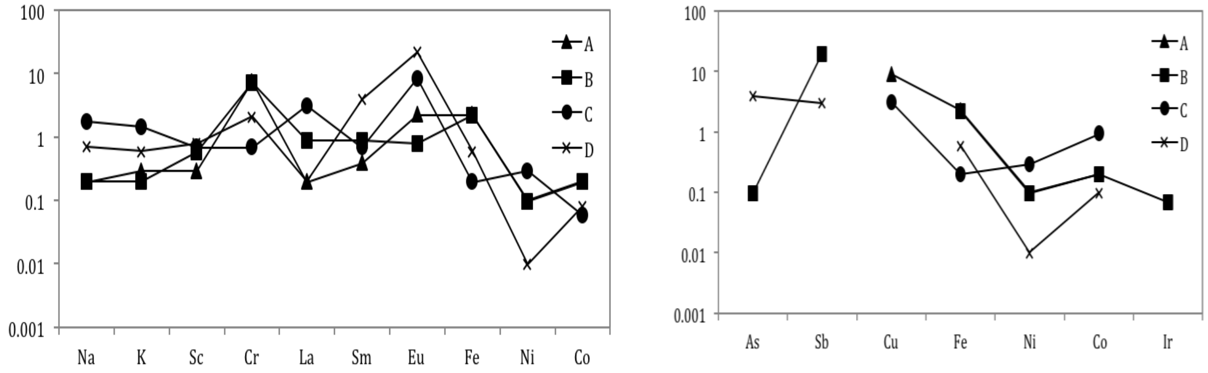

a) b)

Fig.1. CI chondrite–normalized of trace element abundance patterns in non-magnetic fine – grained fractions from Adhi Kot EH4 enstatite chondrite ($\rho > 4.18$ g cm^{-3}): a) lithophile and siderophile elements; b) siderophile elements; 1 – fraction A (45 <d < 71 μm); 2 - fraction B (35<d < 45 μm); 3 - fraction фракция C (25<d < 45 μm); 4 - fraction фракция D (10 < d < 35 μm).

The fine-grained nonmagnetic fractions A, B, D (Fig.1a) ($\rho > 4.18$ g cm^{-3}) are depleted in lithophile nonrefractory Na (0.2 – 0.7 x CI), K (0.2 – 0.6 x CI) and refractory lithophile Sc (0.3 – 0.8 x CI), but is enriched in lithophile Cr (2.1 – 7.86 x CI). Most part fine-grained fractions are depleted in La and Sm, and is enriched in Eu (2.3 – 21.0 x CI), that indicate for positive Eu – anomalies [(Eu/Sm) $_{A, C, D}$ / (Eu/Sm)$_{CI}$] = 5.63 – 12.6. The enrichment in La (3.2 x CI) of fraction C and in Sm (3.9 x CI) of fraction D and the enrichment of all fine-grained fractions (troilite) in Eu can be associated by this, that these elements are take during stage of sulfide condensation.

One of the feature of element distribution in fraction B ($\rho > 4.18$ g cm^{-3}) is high abundances of calcium relative to scandium - [(Ca/Sc) $_F$ / (Ca/Sc)$_{CI}$] = 5.9. Such a distribution of refractory elements with close condensation temperature indicates their strong fractionation in the matter – precursor of this fraction. The fraction C ($\rho > 4.18$ g cm^{-3}) is enriched in La and Eu relative to Sm - [(La, Eu /Sm) $_C$ / (La, Eu /Sm) $_{CI}$] = 4.6 and 12.6, respectively. Such anomalous enrichment in La and in Eu of fraction C can be associated by this that these elements are take during stage of sulfide condensation. The abundance of siderophile elements in fractions with density $\rho >$ 4.18 g cm^{-3} (Fig.1b) show some variations – Ni (0.01 – 0.32 x CI),] and Co (0.06 – 0.15 x CI) and ratios [(Co/Ni) $_{A, B, C, D}$]/[(Co/Ni)$_{CI}$] = 0.18 - 8.0. Such a distribution of siderophile elements with close condensation temperature indicates their strong fractionation of trace elements in the matter-precursor of these fractions. The fraction B (Fig.1b) have the lowest refractory siderophile Ir abundance relative to non-refractory siderophile Ni, Co, As and Sb - [(Ir/ Ni, Co, As,Sb)]$_B$ / [(Ir/ Ni, Co, As, Sb)]$_{CI}$ = 0.7; 0.35; 0.7; 0.003, respectively.

The fine-grained nonmagnetic fractions E, F, G ($\rho < 4.18$ g cm^{-3}) (Fig.2a) are enriched in moderately volatile lithophile Na (1.03 – 1.46 x CI) and are depleted in refractory lithophile Sc (0.38 – 0.52 x CI). The fraction E are characterized more high ration of lanthanum to samarium [(La/Sm) $_E$ / (La/Sm) $_{CI}$] = 1.52, than the fraction F – 1.05 and G – 0.92. Lanthanum shows fractionation to samarium with enrichment La in fraction E. The fraction E и F are characterized by HREE depletion in with regard to LREE [(Lu/La) $_{E,F}$ / (Lu/La)$_{CI}$] = 0.2; 0.5, respectively.

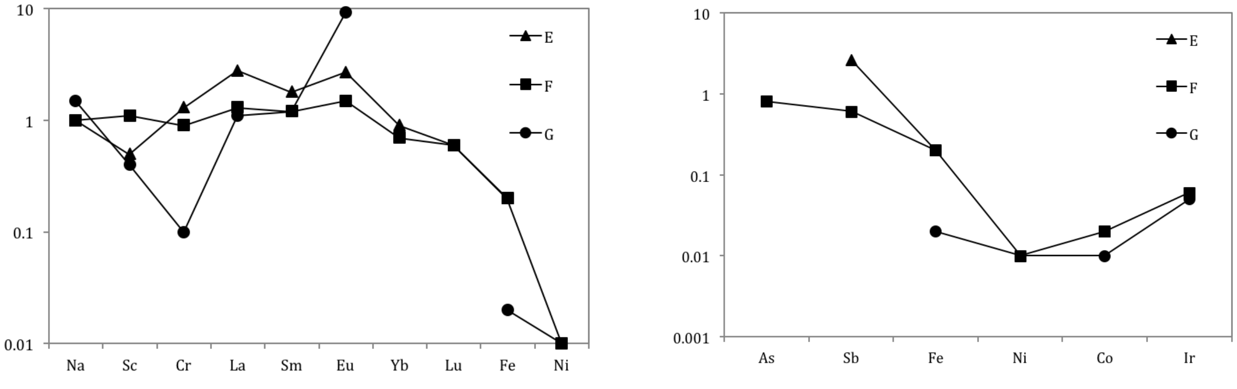

a) b)

Fig.2. CI chondrite–normalized of trace element abundance patterns in non-magnetic fine - grained fractions from Adhi Kot EH4 enstatite chondrite ($\rho < 4.18$ g cm^{-3}): a) lithophile and siderophile elements; b) siderophile elements 1 – fraction E (10<d < 35 μm); 2 - fraction F (25<d < 35 μm); 3 - fraction фракция G (10<d < 45 μm).

One of the feature of element distribution in fraction F is high abundances of scandium relative to calcium -[$(Sc/Ca)_F$ / $(Sc/Ca)_{CI}$] = 4.0. Such a distribution of refractory elements with close condensation temperature indicates their strong fractionation in the matter – precursor of this fraction.

The abundance of siderophile elements in fractions with density $\rho < 4.18$ g cm^{-3} (Fig.2b) show some peculiarities. Iridium – gold relationships in fraction F (25<d < 35мкм) less than cosmic - $(Ir/Au)_F / (Ir/Au)_{CI} = 0.43$, that indicates the fractionation of these elements in this fraction perhaps by shock-melting of matter.

The abundance of lithophile elements in fractions H и K with density ($2.9 < \rho < 3.0$ g cm^{-3}) and L ($\rho < 2.9$ g cm^{-3}) (Fig.3a) show some variations: in Na (0.4 – 1.8 x CI) and K (1.0 – 2.7 x CI) and this ratios [$(Na/K)_{H,K,L}$] / [$(Na/K)/_{CI}$] = 0.15 - 1.3 and considerable variations of LREE - in La (1.2 – 9.0 x CI), in Sm (0.7 – 2.2 x CI), in Eu (0.6 – 27.1 x CI) and this ratios - [$(La/Sm)_{H,K,L}$ / $(La/Sm)_{CI}$] = 1.7 - 4.09; [$(Eu/Sm)_{H,K,L}$ / $(Eu/Sm)_{CI}$] = 1.23 - 1.99. Such a distribution of lithophile elements indicates their strong fractionation of trace elements in the matter-precursor of these fractions.

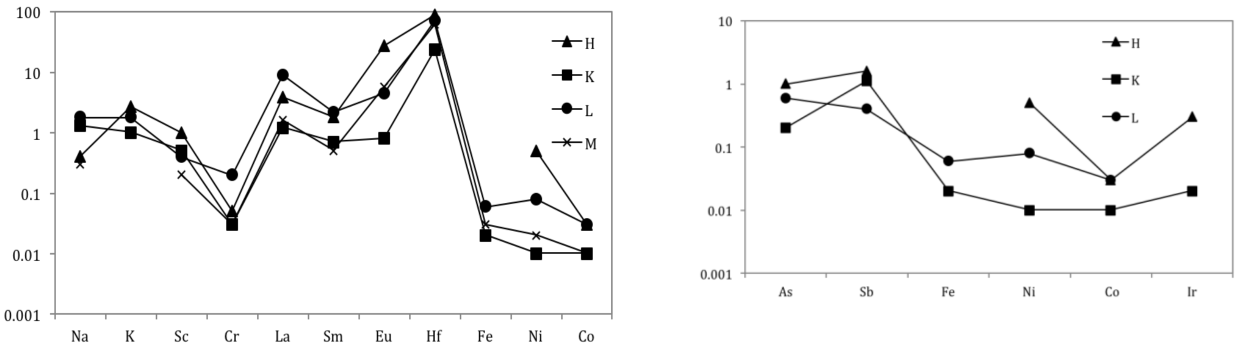

a) b)

Fig.3. CI chondrite–normalized of trace element abundance patterns in non-magnetic fine – grained fractions from Adhi Kot EH4 enstatite chondrite: a) lithophile and siderophile elements; b) siderophile elements 1 – fraction H (1<d < 25 μm), ($2.9 < \rho < 3.0$ g cm^{-3}); 2 - fraction K (35<d < 45 μm), ($2.9 < \rho < 3.0$ g cm^{-3}); 3 – fraction L (1<d < 45 μm), ($\rho < 2.9$ g cm^{-3}).

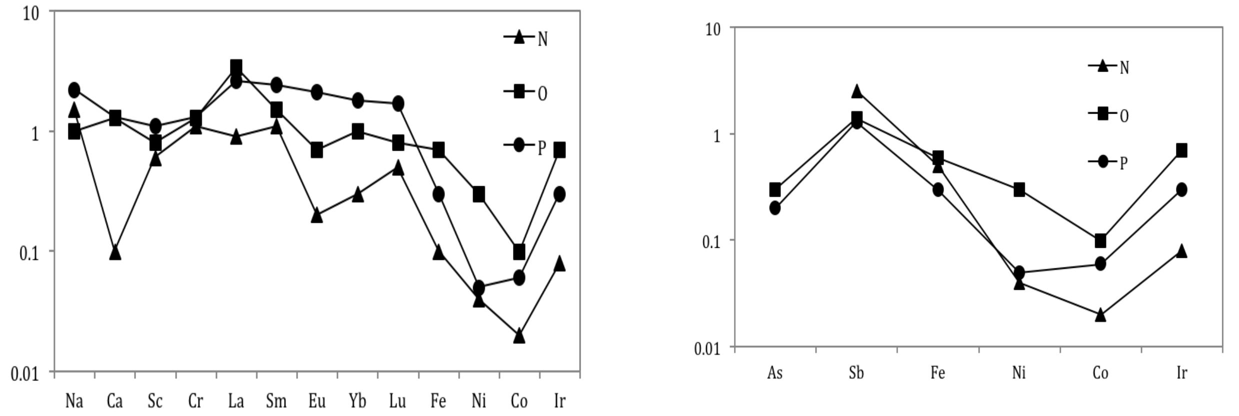

a) b)

Fig.4. CI chondrite–normalized of trace element abundance patterns in non-magnetic fine – grained fractions from Adhi Kot EH4 enstatite chondrite (density no separated): a) lithophile and siderophile elements; b) siderophile elements; 1 – fraction N (10<d < 45 μm); 2 - fraction O (25<d < 45 μm); 3 - fraction фракция P (30<d < 45 μm).

The abundance of lithophile and siderophile elements in the density no separated grain-sized fractions N, O, P (Fig. 4.a, b) show the considerable variations. One of the feature of element distribution in this fractions are low (fraction O) and high (fraction P) abundances of calcium relative to scandium - [$(Ca/Sc_{O,P}$] / [$(Ca/Sc)_{CI}$] = 0.85 and 2.7, respectively. Other feature of element distribution in N, O, P fractions is the depletion of $HREE_S$ - $(Lu/La)_{N,O,P}$ / $(Lu/La)_{CI}$] = 0.24 - 0.65 and Eu minimum - [$(Eu/Sm)_{N,O,P}$ / $(Eu/Sm)_{CI}$] = 0.18 - 0.86, The abundance of siderophile elements in N, O, P fractions (Рис. 4 b) show large variations: Ni (0.04 – 0.3 x CI), Co (0.02 – 0.1 x CI), Ir (0.08 – 0.7 x CI), As (0.2 – 1.0 x CI), Sb (0.4 – 1.5 x CI) and ratios of this elements - [$(Co/Ni)_{N,O,P}$] / [$(Co/Ni)_{CI}$] = 0.3 - 1.2; [$(Ir / Co, Ni)_{N,O,P}$] / [$(Ir / Co, Ni)_{CI}$] = 4.0 и 2.0 (N); 7.0 и 2.3 (O); 5.0 и 6.0 (P), respectively. The fractions N, O, P have the highest refractory siderophile Ir abundance relative to non-refractory siderophile Ni, Co. Such a distribution of lithophile and siderophile elements indicates their strong fractionation of trace elements in the matter-precursor of these fractions.

Conclusion. Based on the study of the features of lithophile and siderophile trace element distributions in the density separated grain-sized fractions from Adhi Kot EH4 enstatite chondrite a conclusion has been made that these peculiarities probably result from mixing effects of nebular fractionation, thermal metamorphism and shock.

References:

Baedecker P.A. and Wasson J.T. Elemental fractionations among enstatite chondrites. //Geochim. Cosmochim. Acta. - 1975. - V. 38. - P. 735 - 765.

Grossman, L., Beckett, J.R., Fedkin, A.V., Simon, S.B., Ciesla, F.J. Redox conditions in the solar nebula: observational, experimental, and theoretical constraints. // Rev. Mineral. Geochem. - 2008. - V.68. - P. 93 - 140.

Hertogen J., Janssens M-J., Jakahashi H., Morgan J. W., Anders E. Enstatite chondrites: trace element clues to their origin. //Geochim. Cosmochim. Acta. - 1983. - V. 47. - P. 2241 - 2255

Keil K. Mineralogical and chemical relationships among enstatite chondrites. //Journal of Geophysical Research. – 1968. - V.73. - P. 6945 - 6976.

Kolesov G. M., Shubina N.V., Lyul A.Yu. Optimizing instrumental neutron activation analysis of extraterrestrial materials: fragments of lunar rocks, meteorites, chondrules and ultrarefractory inclusions. // J. Anal. Chem. - 2001. - V.56. - P. 1169 – 1172.

Leitch C.A., Smith J.V. Petrography, mineral chemistry and origin of type I enstatite chondrites. //Geochim. Cosmochim. Acta. - 1982. - V.46. - P.2083 – 2097.

Rubin A.E. The Adhi Kot breccia and implications for the origin of chondrites and silica-rich clasts in enstatite chondrites. // Earth Planet. Sci. Lett. - 1983. - V.64. - P. 201 - 212.

Rubin A. E. (2008). Geochemical, mineralogical and petrological relationships in enstatite chondrites. //Lunar Planet. Sci. Conf. XXXIX. – 2008. - # 1114.

Sears D.W., Kallemeyn G. W., Wasson I. T. The compositional classification of chondrites II. The enstatite chondrite groups. // Geochim. Cosmochim. Acta . - 1982. - V. 46. - P. 597 - 608.

Weisberg M. K., Ebel D. S., Connolby Ir., Kita N. T., Ushikubo T. Petrologic – geochemical study of chondrules in enstatite chondrites. //Lunar Planet. Sci. Conf. XL. - 2009. - #1886.

Lyul A.Yu., Lavrentjeva Z.A. On the siderophile element distributions between the metal and fine-grained fractions of the enstatite meteorites. UDC 542.42

Vernadsky Institute of Geochemistry and Analytical Chemistry RAS, Moscow (ajull@mail.ru)

Abstract. Analysis of the data on the siderophile element contents in the metal and fine-grained fraction of enstatite chondrites and achondrites shows that that the secondary processes in parent bodies did not lead to a noticeable redistribution of elements between the major components of meteorites. The similarity of trends in the fractionation of siderophile elements in the metal and the fine-grained fraction of enstatite chondrites and achondrites are consisted with the hypothesis that enstatite meteorites were formed at different depths of a single parent body.

Keywords*: enstatite meteorites, metal, fine-grained fractions, siderophile elements, fractionation*

Introduction. Enstatite meteorites that have been formed under strongly reducing conditions are represented by two, possibly genetically related types, a namely, the primitive chondrites with different iron contents and differentiated achondrites. These two groups of meteorites, the main component of which is iron-free enstatite (FeO <1 wt.%), are similar in mineralogy, in the presence of Si-containing metal and numerous sulphides formed by typically lithophile elements, and also have a similar isotopic composition of oxygen, but differ greatly in structure and in metal content (from 19 to ~ 28 wt.% in E-chondrites and <1 wt.% in achondrites) (Keil, 1968, Watters, 1979). Owing to these similarities, the question of the genetic relationship between enstatite meteorites has been the subject of many years discussion about two main models for the formation of this group of meteorites. According to one of model, enstatite meteorites were formed in a single parent body, the composition of which corresponds to the composition of EL6 chondrites ([Moynier F et al., 2011, van Acken et al. 2012), while other researchers believe that enstatite chondrites and achondrites were formed in chemically similar bodies, but at different heliocentric distances from the Sun (Brett R., Keil K., 1986). To receive a more information about the compositional features of the individual components of enstatite of meteorites, the data on the of siderophile element contents in the fine-grained (<45 μm) fraction and metal of enstatite chondrites of EH and EL groups and enstatite achondrites (fragmental breccia Norton County and regolith breccia Pesyanoe) are discussed. The data on the siderophile element contents in the separated fractions obtained by INAA method are given in the table and the abundance of these elements normalized to CI-chondrites in these components is presented in Fig.1 and 2.

Results and discussion

You can also note (Tab., Fig. 1, 2) a number of common properties characteristic of the composition of the metal enstatite chondrites and achondrites. So, the peculiarity of the metal composition of enstatite meteorites is a noticeable fractionation between iridium and gold - elements with strong siderophile properties, but with different volatility. This type of fractionation is characteristic of the metal of iron meteorites that have passed the stage of magmatic differentiation. However, since it is observed both in chondrites and achondrites, it is primary and indicates the formation of this group of meteorites in the gold-rich region of the protoplanetary cloud.

Table. 1. Siderophile element contents for metal (1) and fine-grained fraction (2) of enstatite chondrites (Co, Ir, Au, Ga in µg/g). Data from (Lavrukhina et al., 1982; Lyul et al., 2017).

	Abee EH4		Adhi Kot EH4		Atlanta EL6		Pillistver EL6	
	1	2	1	2	1	2	1	2
Fe, %	92	11.5	93	7.6	94	14.2	93	9.5
Ni, %	7.1	0.24	6.4	0.06	6.0	0.77	6.5	0.14
Co	3660	120	3200	32	3400	365	3600	48
Ir	2.43	0.048	1.6	0.14	1.9	0.26	1.8	0.032
Au	1.35	0.05	1.4	0.16	1.2	0.11	1.0	0.013
Ga	71	8.2	56	6.8	53	5.1	49	4.9

Table 2. Siderophile element contents for different components of the enstatite achondrites. (Co, Ir, Au, Ga in µg/g). Data from (Lyul et al. 2013; Lavrentjeva et al., 2003).

	Norton County			Pesyanoe		
	1	2	3	1	2	3
Fe,%	91	87	1.6	91	89	1.5
Ni,%	7.5	10.9	0.04	6.72	7.95	0.075
Co	3260	3100	5.5	3060	2930	15
It	2.4	0.34	0.006	3.13	0.11	0.005
Au	1.4	2.0	0.25	1.33	1.5	0.01
Ga	40	39	0.2	48	43	0.2

1- Fe,Ni- nodules;
2-fine metal grains;
3- fine-grained fractions

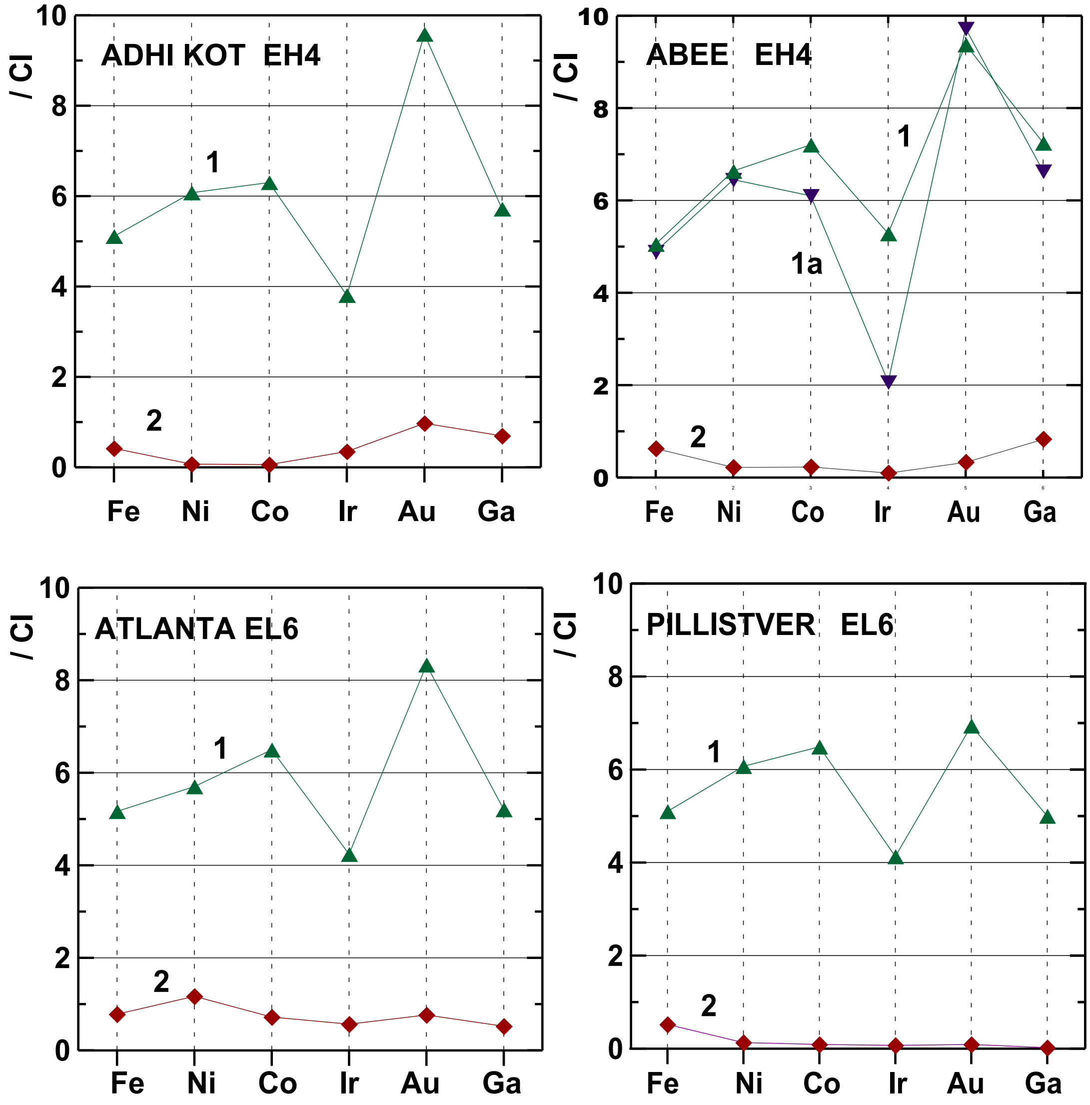

Fig. 1 CI-normalized siderophile element abundance patterns for the enstatite chondrite components. 1 - Fe,Ni metal (Lavrukhina et al, 1982); 2-fine-grained fraction {Lyul et al., 2017); 2a- metal particle from a impact-melted clast (Sears et al., 1983).

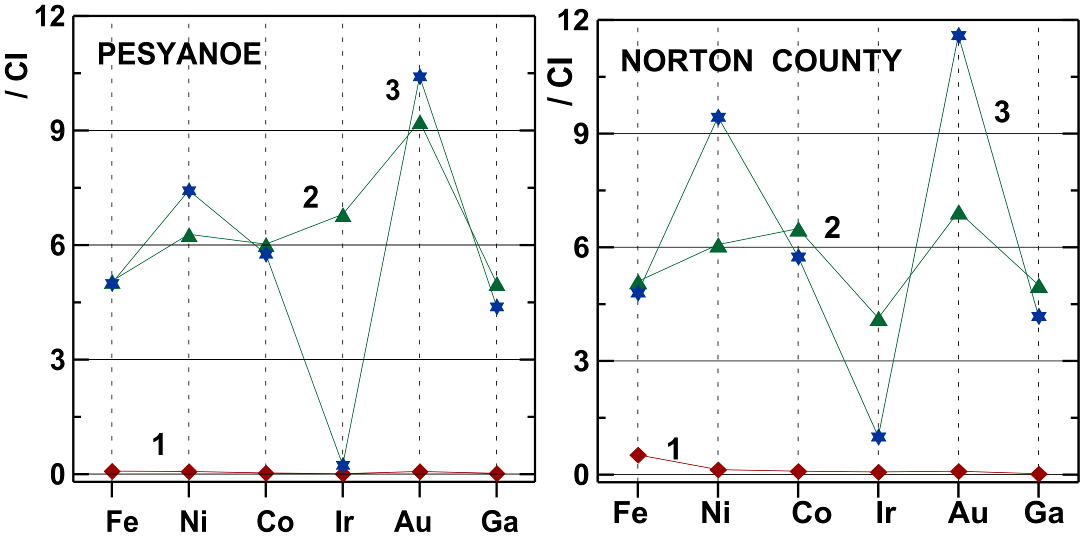

Fig. 2. CI-normalized siderophile element abundance patterns for the components of enstatite achondrites 1 – fine-grained fractions; 2- large metal nodules; 3 – fine-grained metal. Data (Lavrentjeva et al., 2003; Lyul et al., 2013)

A noticeable fractionation between Ir and Au was also found in the Abee EH4 chondrite metal particle, isolated from the impact-molten clast (see Fig. 1), the magnitude of which significantly exceeds that observed in the chondrite metal. Consequently, the degree of fractionation between these elements characterizes the intensity of the partial melting of the metal in the parent bodies of meteorites. As follows from Fig. 2, the degree of partial melting of the Pesyanoe regolith breccia is higher than that of the fragmental breccia Norton County. However, it is possible that the repeated agglomeration of fragments of Norton County somewhat averaged the composition of the metal ejected from different depths of its parent body.

From the given in Fig. 1 and 2 data on the content of siderophile elements of different volatility in the metal and the fine-grained fraction of enstatite meteorites follows that the variations in the relative abundance of siderophile elements in the metal of meteorites far exceed those for the corresponding fine-grained fractions. Consequently, either the composition of the smallest grains of the metal enstatite meteorites included in the fine-grained fraction is different from the composition of the main mass of the metal, or these elements are partly included in other components of this group of meteorites.

The metal phase of enstatite meteorites is characterized by the enrichment of gold relative to other siderophile elements. The same trend is also observed for the fine-grained fraction of chondrites, with the exception of the Abee chondrite fraction. Since gold is concentrated mainly in the taenite, but the metal of enstatite meteorites is represented mainly by kamacite, the composition of these fraction of enstatite meteorites may be primary, originated during the formation of this group of meteorites in the protoplanetary nebula.

There are two types of siderophile element fractionation in the metal of the Norton County and Pesyanoe achondrites. The composition of large grains of metal is similar to that of the metal phase of chondrites, whereas the significant fractionation between Ir and Au observed in the fine-grained metal fraction indicates a partial melting of the meteorite metal in its parent body. Minor gold enrichment is also observed in the fine-grained fraction of the meteorite. It can also be noted that the content of siderophile elements in the fine-grained fraction of achondrite is significantly lower than that in the similar fraction of chondrites. This depletion is caused by very low metal content in this group of enstatite meteorites. The enrichment of iron relative to the other siderophile elements in the fine-grained fraction of the Norton County achondrite may be due to the presence in it the smallest grains of troilite or daubreelite. The similarity in chemical composition and in fractionation trends of siderophile elements in the Fe,Ni-phase of chondrites and achondrites is consistent with the model of the formation of enstatite meteorites at different depths of a common parent body.

Conclusion Analysis of the data on the fractionation of siderophile elements of different volatility in the fine-grained fraction and metal of enstatite chondrites and achondrites revealed a similarity of trends in the fractionation of this group of elements in enstatite meteorites. Variations in ratios between highly siderophile elements Ir and Au are consistent with the hypothesis of the enstatite meteorites formation at different depth of a single parent body.

References:

Brett R., Keil R., Enstatite chondrites and enstatite achondrites (aubrites) were not derived from the same parent body // Earth Planet. Sci. Lett., —1986. Vol. 81. —P. 1-6.

Lavrentjva Z.A., Lyul A.Yu. REE and some other trace element distributions of mineral constituents in enstatite meteorites. // Lunar and Planetary Science XXXIV. — 2003. 1026.pdf

Lavrukhina A.K., Lyul A.Yu., Baryshnikova G.V. On the distributions of siderophile elements in the Fe,Ni-phase of ordinary and enstatite chondrites // Geochemistry. —1982. N 5. —P. 645-663. (In Russian)

Lyul A.Yu., Kolesov G.M., Lavrukhina A.K. //Elemental composition and history of the metal from enstatite achondrites Pesyanoe and Norton County // Geochemistry. —2013. N 7. —P. 1-16. (*In Russian*)

Lyul A.Yu., Lavrentjeva Z.A., On siderophile elements and Se fractionation in the fine-grained fractions of enstatite chondrites // Proceeding of 18th International Conference “Physical-chemical and petrography research in Earth’ Science. 2017. Moscow. P. 168-171. (*In Russian*)

Moynier F., Panielo .C., GounelleM/. Albare F., Beck P., Podosek F., Zanda B. // Nature of volatile depletion and genetic relationship in enstatite chondrites and aubrites inferred from Zn isotopes . // Geochim. Cosmochim. Acta. —2011. V. 75. — P. 297-307.

van Acken D., Brandon A. D., Humayun M. // Siderophile trace elements in metal and sulfides on enstatite achondrites record planetary differentiation in an enstatite chondritic parent body. // Geochim. Cosmochim. Acta. —2011. V. 75. —P. 297-307

Watters T.R., Prinz M. Aubrites: their origin and relationship to enstatite chondrites. // Proc. 10th Lunar Planet. Sci. Conf., 1979. P. 1073-1093.

Wasson J.T., Wai C.M., Composition of metal, schreibersite and perryite of enstatite chondrites and achondrites // Geochim. Cosmochim. Acta. —1970. V.34. —P. 169-184.

Shornikov S. I. Thermodynamics of evaporation of perovskite – the mineral of white inclusions of chondrites

V. I. Vernadsky Institute of Geochemistry & Analytical Chemistry RAS, Moscow (sergey.shornikov@gmail.com)

Abstract. The perovskite evaporation studied by high-temperature Knudsen effusion mass spectrometric method at 1700–2200 K. The molecular components typical of simple oxides and a small amount of $CaTiO_3$ complex gaseous oxide identified in the gas phase over perovskite. For the first time, the determined values of the partial pressures of the vapor of molecular components contained in the gas phase over perovskite are compared with those corresponding to simple oxides. It shown the predominant effect of the calcium component of perovskite on its evaporation process.

***Keywords**: Knudsen effusion mass spectrometric method, thermodynamics of evaporation, perovskite*

Calcium titanate $CaTiO_3$ (perovskite) is a relatively rare mineral. Perovskite is of particular interest for cosmochemical studies, as a mineral of the substance of refractory Ca–Al–inclusions, often found in carbonaceous chondrites – an earliest object of the Solar system with unusual isotopic characteristics (Zhang et al., 2014).

There are two more calcium titanates in the CaO–TiO_2 system – $Ca_3Ti_2O_7$ and $Ca_4Ti_3O_{10}$, which melt incongruently (Fig. 1).

It is believed that perovskite is a polygenic material that combines the relict substance formed in the inner shells of supernovae, and the product of high-temperature gas condensation, and the product of crystallization of silicate melt (Nazarov et al., 1984; Goswami et al., 1991). In this regard, experimental information on evaporation processes and thermodynamic properties of perovskite is important for understanding of its formation in the composition of CAIs.

The evaporation of perovskite in the temperature range 1791–2182 K and the CaO–TiO_2 melts in the temperature range 2241–2441 K from a molybdenum container were studied by Knudsen effusion mass spectrometric method.

The established molecular composition of the gas phase over perovskite and over the CaO–TiO_2 melts testified to the evaporation of the considered compositions according to the reactions typical for the evaporation of individual oxides:

$[CaO] = (CaO)$ (1)
$(CaO) = (Ca) + (O)$ (2)
$[TiO_2] = (TiO_2)$ (3)
$(TiO_2) = (TiO) + (O)$ (4)
$(TiO) = (Ti) + (O)$ (5)
$2(O) = (O_2)$ (6)

(the square brackets denote the condensed phase and the parentheses brackets denote the gas phase).

The presence of a small amount of molecular form ($CaTiO_3$) in the gas phase over perovskite showed the possibility of the following heterogeneous reaction:

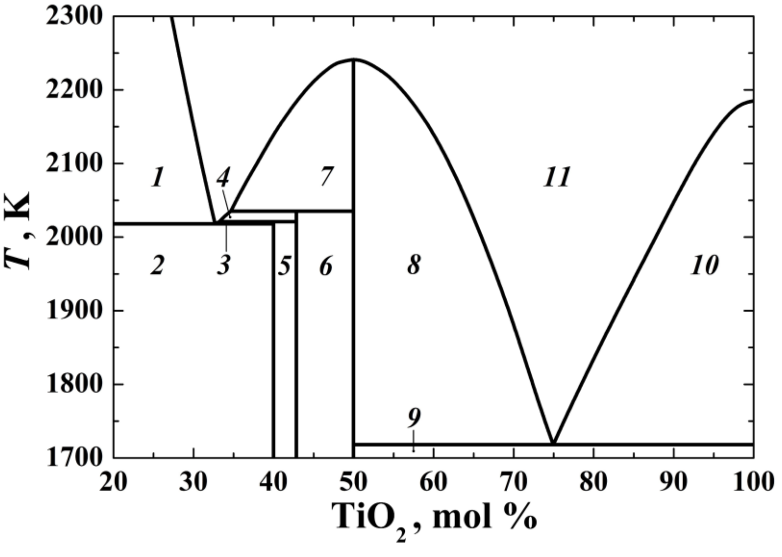

Fig. 1. The phase diagram of the CaO–TiO_2 system (Gong W. et al., 2018): ***1*** – CaO + liquid; ***2*** – CaO + $Ca_3Ti_2O_7$; ***3*** – $Ca_3Ti_2O_7$ + liquid; ***4*** – $Ca_4Ti_3O_{10}$ + liquid; ***5*** – $Ca_3Ti_2O_7$ + $Ca_4Ti_3O_{10}$; ***6*** – $Ca_4Ti_3O_{10}$ + $CaTiO_3$; ***7*** and ***8*** – $CaTiO_3$ + liquid; ***9*** – $CaTiO_3$ + TiO_2; ***10*** – TiO_2 + liquid; ***11*** – liquid.

$$[CaTiO_3] = (CaTiO_3). \quad (7)$$

The values of partial pressures of the gas phase components (p_i) over perovskite and over the CaO–TiO_2 melts were determined by the Hertz-Knudsen equation (Fig. 2).

Values of oxide activities (a_i) in perovskite and in the CaO–TiO_2 melts were calculated on the Lewis ratio:

$$a_{CaO} = \frac{p_{CaO}}{p^{\circ}_{CaO}} \quad (8)$$

$$a_{TiO_2} = \frac{p_{TiO_2}}{p^{\circ}_{TiO_2}}. \quad (9)$$

They were calculated by an independent method according to Belton and Fruehan (1971) in the case of the CaO–TiO_2 melts (Fig. 3a) using the following relationship:

$$\ln a_i = -\int x_j d \ln \frac{a_j}{a_i}, \quad (10)$$

which could be converted in the case of titanium dioxide to the following equation:

$$\ln a_{TiO_2} = -\int x_{CaO} d \ln \frac{p_{Ca} p_O}{p_{TiO} p_O} = -\int x_{CaO} d \ln \frac{p_{Ca}}{p_{TiO}}. \quad (11)$$

At the same time it becomes possible to minimize the value of non-systematic error of the experiment, taking into account the proportionality of the partial pressure values (p_i) to the ion currents (I_i):

$$\ln a_{TiO_2} = -\int x_{CaO} d \ln \frac{I_{Ca}}{I_{TiO}}. \quad (12)$$

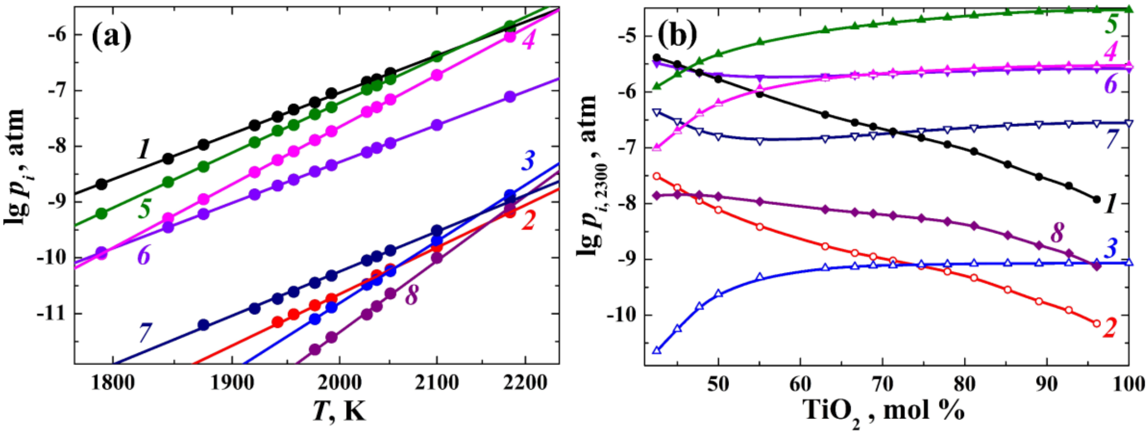

Fig. 2. The partial pressure of vapor species over the perovskite (a) and over the CaO–TiO_2 melts (b) at 2300 K: ***1*** – Ca, ***2*** – CaO, ***3*** – Ti, ***4*** – TiO, ***5*** – TiO_2, ***6*** – O, ***7*** – O_2, ***8*** – $CaTiO_3$.

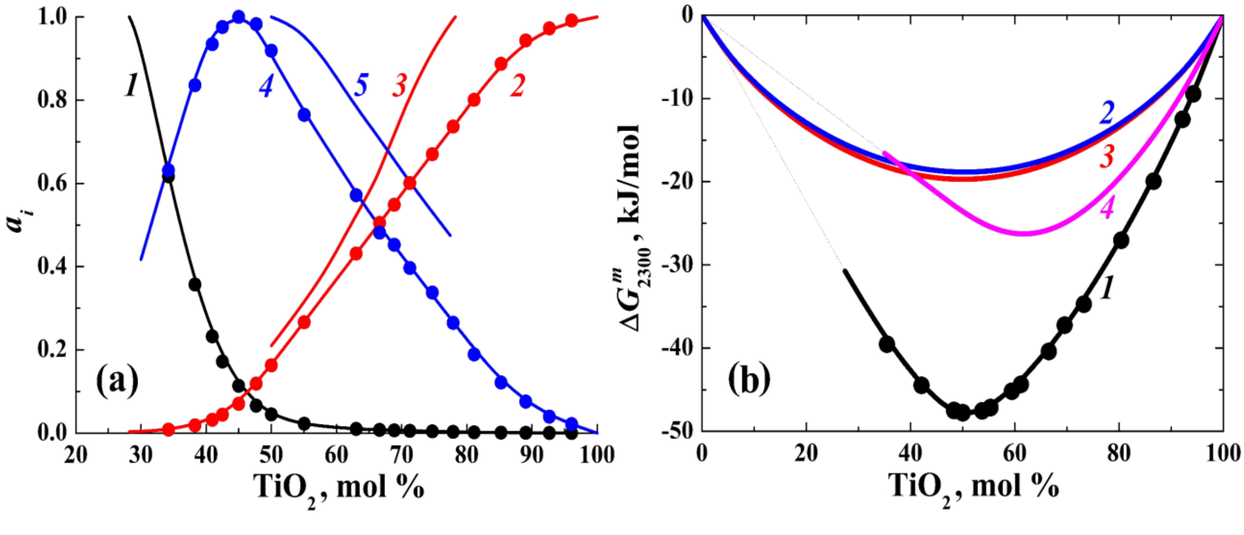

Fig. 3. Activity of oxides (a) and mixing energy (b) in the CaO–TiO_2 melts.

The activities of CaO (***1***), TiO_2 (***2***, ***3***) and $CaTiO_3$ (***4***, ***5***) oxides were determined by the Knudsen effusion mass spectrometric method: ***1***, ***2*** and ***4*** – in the present study at 2250 K; ***3*** and ***5*** – by Banon et al. (1981) at 2150 K.

Mixing energies in the CaO–TiO_2 (***1***), FeO–TiO_2 (***2***), Al_2O_3–TiO_2 (***3***) and MgO–TiO_2 (***4***) melts at 2300 K, determined experimentally in the present study and calculated in (Shornikov, 2018; Shornikov and Shornikova, 2018; Shornikov, 2019), respectively. Dotted lines correspond to the heterogeneous areas.

It becomes possible also to avoid the need for additional thermochemical data (Glushko et al., 1978–1982). The values of a_{CaO} in the CaO–TiO_2 melts were calculated by the Gibbs-Duhem equation:

$$\ln a_{CaO} = -\int \frac{x_{TiO_2}}{x_{CaO}} d \ln a_{TiO_2} \quad (13)$$

According to the relations (8), (9), (12) and (13) the calculated values of oxide activities has allowed to determine the values of mixing energy (ΔG^m) in the CaO–TiO_2 melts (Fig. 3b), as well as the enthalpy and entropy of perovskite formation (from simple oxides), equal to –39.88±0.54 kJ/mol and 3.15±0.28 J/(mol×K), respectively, and the melting enthalpy of perovskite at 2241±10 K, equal to 47.61±1.84 kJ/mol (per 1 mol of the compound).

The determined values of CaO, TiO_2 and $CaTiO_3$ activities in the CaO–TiO_2 melts at 2250 K with those obtained by Banon et al. (1981) at a close temperature of 2150 K are presented in Fig. 3a. Some difference in the activity of titanium dioxide is probably due to extrapolation procedures of information obtained by Banon et al. (1981) for the compositions of the $CaTiO_3$–Ti_2O_3–TiO_2 triple system, which could reduce their accuracy. However, their observed behavior of TiO_2 activity in melt at concentrations close to rutile, as well as in the present work, indicates some immiscibility in the melt, which follows from the observed inflection of the concentration dependence of a_{TiO_2} (Fig. 3a). The a_{CaTiO_3} maximum value corresponds to the compositions close to perovskite (Fig. 3a, lines ***4*** and ***5***).

A comparison of mixing energy in the CaO–TiO_2 melts at 2300 K with those for the FeO–TiO_2 (Shornikov, 2018), Al_2O_3–TiO_2 (Shornikov and Shornikova, 2018) and MgO–TiO_2 (Shornikov, 2019) melts, shown in Fig. 3b indicates a stronger chemical interaction in the CaO–TiO_2 melt compared to the other melts under consideration, which is due to the high base of calcium oxide in the melt. The considered titanate melts can be arranged in the following series according to the degree of chemical interaction: CaO → MgO → Al_2O_3 → FeO.

The present study was supported by RAS Presidium's Program #7 (*Experimental and theoretical studies of Solar system objects and star planetary systems. Transients in astrophysics*) and the Russian Foundation for Basic Research (grant #19-05-00801A).

References:

Banon S., Chatillon C., Allibert M. (1981) Free energy of mixing in $CaTiO_3$–Ti_2O_3–TiO_2 melts by mass spectrometry. *Can. Met. Q.*, vol. 20, no. 1, pp. 79–84.

Belton G. R., Fruehan R. J. (1971) The determination of activities of mass spectrometry: some additional methods. *Met. Trans. B*, vol. 2, no. 1, pp. 291–296.

Glushko V. P., Gurvich L. V., Bergman G. A., Veitz I. V., Medvedev V. A., Khachkuruzov G. A., Yungman V. S. (1978–1982) Thermodynamic properties of individual substances. Moscow: Nauka, vol. 1–4.

Gong W., Wu L., Navrotsky A. (2018) Combined experimental and computational investigation of thermodynamics and phase equilibria in the CaO–TiO_2 system. *J. Amer. Ceram. Soc.*, vol. 101, no. 3, pp. 1361–1370.

Goswami J. N., Srinivasan G., Ulyanov A. A. (1991) Titanium, calcium and magnesium isotopic compositions in a hibonite-rich inclusion from Efremovka. *Met. Planet. Sci.*, vol. 26, no. 4, p. 339.

Nazarov M. A., Korina M. I., Ulyanov A. A., Kolesov G. M., Sherbovsky E. J. (1984) Mineralogy, petrography and chemical composition of calcium and aluminum-rich inclusions of Efremovka meteorite. *Meteoritika*, vol. 43, pp. 49–65 (in Russian).

Shornikov S. I. (2018) Thermodynamic properties of the FeO–TiO_2 melts. *Proc. XIX Intern. Conf. "Physical-chemical and petrophysical researches in the Earth's sciences"*. Moscow: IGEM RAS, pp. 345–348 (in Russian).

Shornikov S. I., Shornikova M. S. (2018) Thermodynamic properties of the Al_2O_3–TiO_2 melts. *Proc. XIX Intern. Conf. "Physical-chemical and petrophysical researches in the Earth's sciences"*. Moscow: IGEM RAS, pp. 349–352 (in Russian).

Shornikov S. I. (2019) Thermodynamic properties of the MgO–TiO_2 melts. *Experiments in Geosciences*, vol. 25, no. 1.

Zhang J., Huang S., Davis A. M., Dauphas N., Hashimoto A., Jacobsen S. B. (2014) Calcium and titanium isotopic fractionations during evaporation. *Geochim. Cosmochim. Acta*, vol. 140, pp. 365–380.

Tselmovich V.A.[1], Maxe L.P.[2] Cosmogenic substance from sedimentary rock, called tripoli, from the deposit field «Stalnoye». UDC 523.681

[1]Borok Geophysical Observatory is a branch of Shmidt's Institute of Physics of the Earth, Russian Academy of Sciences, (tselm@mail.ru), [2]LL "Tsedar", Mogilev, Republic of Belarus, (larissa_maxe@rambler.ru)

Abstract. Cosmic dust (CD) was studied in samples of the sedimentary rock tripoli and peat. Sedimentary rock tripoli from the field «Stalnoye» is characterized by the specific composition caused by conditions of its formation that affected the preservation of cosmic particles. CD extracted from peat and tripoli has a similar morphology and chemical composition. The predominant part of CD particles is Mt balls of ablative origin and micrometeorites, pure Fe and FeCr alloys. Particles of pure Ni and its alloys are not preserved in the tripoli sediment but were found in peat from deposits in the Mogilev region. The safety of Ni-particles differs from the unified nature of the CD.

Keywords: *tripoli, sedimentary deposit, tripoli rock, Paleogen, cosmic dust, Mt microspheres, cosmogenic origin, peat, Ni particles, micrometeorite.*

Introduction. Cosmic dust (CD) continuously falls on the Earth in the amount of 40 thousand tons per year. CD is accumulated in the various forms of the environment. Information about the features of its accumulation, the safety of CD microparticles having been in various forms of the environment during long geological periods of the Earth has not only scientific interest as it can be taken into account while solving a wide variety of problems arising from the study of Earth history (climate, stratigraphic, etc.), but also solving technological tasks.

The present work is the initial stage of the study of cosmic dust accumulated over the millions of years in the «Stalnoye» field (located on the border with the Russian Federation, Khotimsky district, Mogilev region, Republic of Belarus). The task was to study comparatively the characteristics of the accumulation and preservation of CD particles inside the environment of marine deposits (in tripoli). Taking into account the fact that the age of the sedimentary rock tripoli is tens of millions of years, and the age of peat does not exceed 12 000 years, we compared the CD, isolated from peat and tripoli rock.

Tripoli rock under study is sedimentary rock, nonmetallic, semi solid mineral. Rocks like tripoli are found throughout the world, but they differ significantly in mineralogical and elemental composition. In many countries, tripoli refers to monomineralic rock, almost entirely represented by amorphous silica (diatom shells, re-precipitated silica gel, volcanic ash). But there are deposits of tripoli where it includes two or more main rock-forming minerals and a complex of concomitants.

A feature of the structure of all tripoli types is their microporous internal structure due the amorphous state of the main components (silica, aluminosilicates). The combination of internal channels and cavities creates a system of pores, the surface of which (the inner surface of the adsorbent) can be hundreds of square meters per 1 g. Features of the structure, sorption and cation-exchange properties of both monomineral and composite tripoli cause a wide range of areas of its practical application. Bergmeal (tripoli) is used as an adsorbent and enterosorbent, as a filtering material in the textile, petrochemical, feed industry, it is used in the manufacture of antibiotics, paper, paint.

At present the industrial development of the «Stalnoye» field has begun, that gives respectively the possibility to study the composition and the origin of magnetic impurities that has scientific and practical importance.

Cretaceous sediments of Belarus (and several regions of Russia) were formed in the Mesozoic (the Cretaceous) period. However, thripoli sediment had been probably formed in the Cenozoic era. In the Paleogene there was a warm, shallow sea in the South which boundary was not constant and passed through the territory of the modern Mogilev region. Finally, the ancient sea left the territory of Belarus about 30 million years ago.

The open pit of the field under development is located in the east of the Mogilev region near the border of the Russian Federation, 7 km from the urban settlement Khotimsk. With geographic proximity to the sedimentary deposits in the Bryansk region, deposit rocks of the «Stalnoye» are significantly different both from them and from other sedimentary rocks of Russia by their mineralogical composition, features of occurrence, location and hydrological regime of formation. The open-pit mine is quickly flooded, as can be seen in satellite imagery. The proximity of the Paleogene-Neogene sediments to the surface is explained by neotectonic processes – uplift in the west of the Voronezh anteclise; in the later Quaternary period glaciers produced their work four times.

The main peculiarity of the tripoli from the «Stalnoye» is that within 30 – 35 million years it was formed as a natural composite – by the co-precipitation of aluminosilicates (smectites, zeolites), amorphous silica, and biogenic calcium carbonate. During these millions of years, the bottom of the ancient sea collected not only the material composing the sedimentary rock, but also the falling out of space matter. The structure and elemental composition of CD became the subject of research when it was extracted from samples of native tripoli rocks of the «Stalnoye» deposit, as well as CD isolated from the mass of metal-magnetic impurities.

The main minerals forming tripoli rock of the «Stalnoye» studied at CD are as follows: smectites (beidellite, montmorillonite, 25 – 40 %), silica (opal cristobalite and amorphous diatom transformation forms, 20 – 40 %), zeolites (heylandite, clinoptilolite, 10 – 20 %) and microcalcite (mainly represented by coccoliths – fragments of coccolithophores – carbonate unicellular algae, 15 – 30 %). Pyrite (often biogenic), hematite, terrigenous minerals and sands similar to placers (including small zircon crystals) are found in the rock, the rock also contains mineralized remains of the simplest filamentous, stained with microinclusions and UV fluorescent compounds.

The coordinates of the location of the open pit mining of the «Stalnoye» (south-west of the village Vasilevka-2): 53.479508, 32.567206 (marked using the satellite map – satellite image of the quarry).

Methods & Results. The preparation for microscopic study was isolated with a magnetic plate from MM-concentrate – an average sample from a sample of factory metal-magnetic admixture (with a total mass of 24 kg), formed during cleaning (with a magnetic column with neodymium magnets) 200 tons of the tripoli sedimentary rocks. Such high volume of processed raw material allowed us to hope that these preparations may contain the most characteristic microparticles. The presence of a large number of magnetic microspheres was marked in the studied samples that aroused interest of their origin's study and elemental composition. Although similar microspheres can have the most diverse origins (technogenic, volcanogenic, cosmogenic), as the most likely, we considered the cosmogenic origin of these microspheres. The reason for this conclusion is the absence of volcanic activity in the Mogilev region during the last 300 million years, as well as the absence of industrial sources and mechanisms for the formation of technogenic microspheres. In addition, a similar set of microspheres was previously found in sections of various peatlands (Tselmovich, 2018; Tselmovich et al, 2019a; Tselmovich et al, 2019b), where it was also suggested that the microspheres are cosmogenically originated. Unlike peatlands, in which nickel microparticles were rarely found, nickel was not detected in the studied extracts of CD from tripoli sediment of the «Stalnoye».

For comparison with previously studied samples of peat sections we studied samples of peat from the deposit «Gonchanskoye» (peat processing plant «Dneprovskoe», Bykhov district, Mogilev region, Republic of Belarus). The samples were taken on October 4, 2017 from the batch of milled peat delivered to a processing plant in Chausy in 2015 (from the deposit «Gonchanskoye» for processing). Mt microspheres, Fe, FeCr, Ni were detected in those peat samples.

We believe that the absence of cosmogenic nickel particles in magnetic extracts from our tripoli samples is a feature of the results obtained at this stage of research, which requires a separate analysis.

Taking into account the above features and geochronology of the tripoli formation, it can be assumed that conditions could arise in a warm sea basin causing natural «dissolution» of cosmogenic nickel particles differing in micro- and nano-geometrical characteristics from terrigenous minerals that contained nickel in the compounds.

The presence of carbonates and coccolithic sediments caused the alkaline environment of the warm ancient basin. In the deep parts conditions that were favourable for the development of methanogens might have been developed; for their metabolism, nickel is needed, which is part of their enzymes and catalyzes chemical reactions. Archaebacteria that prevailed during the pre-oxygen geological period are activated in favourable conditions and in other periods of the Earth development. During the warming period caused, among other things, by the fall of a large number of meteorites in the Paleogene (Paleocene-Eocene boundary), their development could have a local, but relatively long-term character.

The small dispersion of particles and the tendency of nickel to pitting contribute to the transition of metallic nickel into warm sea water, while the conditions regulating the process of nickel passing into solution are temperature, pH of the medium, ionic composition, nature of the marine basin. In swamps and peatlands the conditions for the accumulation of particles of a cosmogenic substance differ significantly from the conditions of the marine basin by the temperature regime, time interval, acidity, oxygen supply, and other factors. For cyanobacteria, nickel is not a limiting element.

Nickel was not detected in CD studies from Atlantic oceanic sediments (Pechersky et al, 2013). Probably, our conclusions have also worked in this case regarding the behavior of nickel.

The composition of the substance surrounding the CD small magnetic balls in tripoli sedimentary rock and in the peat bog leaves its «imprint» and affects the results of microprobe analysis. On the Mt balls recovered from the tripoli, «adhered» aluminosilicate (smectite) is noted, on the Mt peat balls – amorphous silica, which is associated with differences in sedimentation conditions.

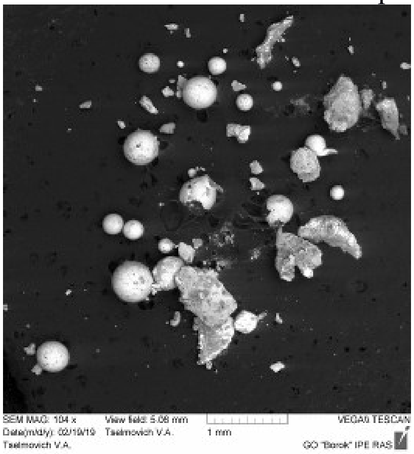

Fig.1. General view of magnetite balls from tripoli.

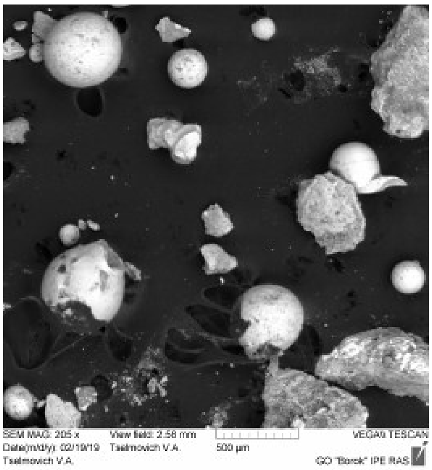

Fig.2. General view of magnetite bead from tripoli.

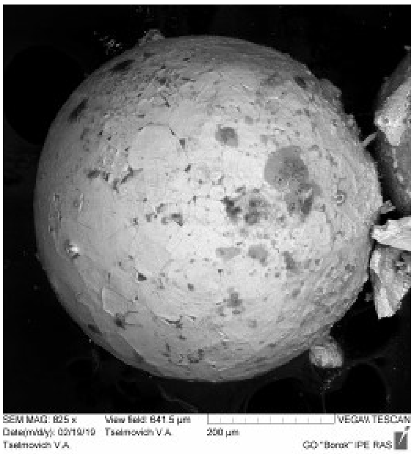

Fig.3. Micrometeorite, Mt.

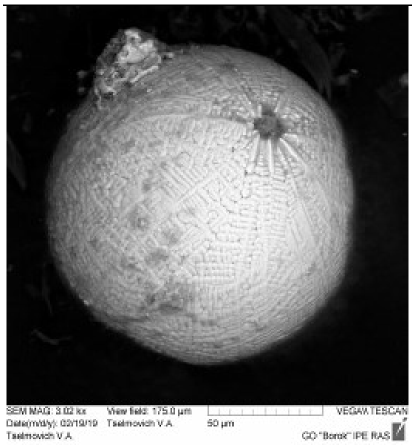

Fig.4. Mt with detrital structure of ablative origin.

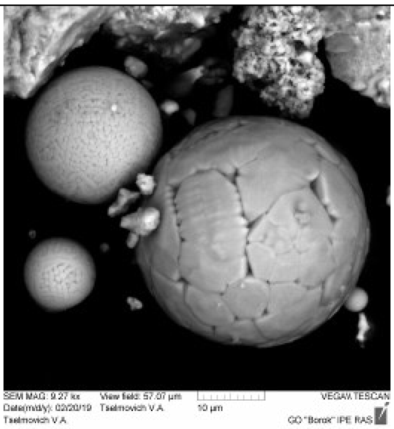

Fig.5. Mt microspheres -micrometeorite (right) and ablative microspheres.

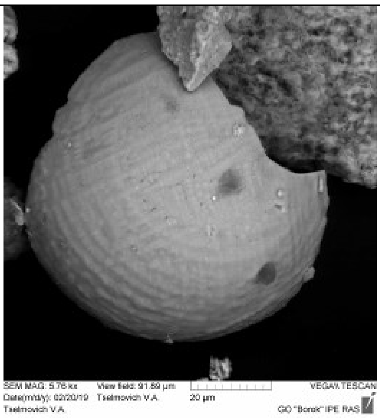

Fig.6. Chip hollow Mt microspheres of ablative origin.

Fig.7. Scaled Fe.

Fig.8. Fe band and Mt microsphere of ablative origin.

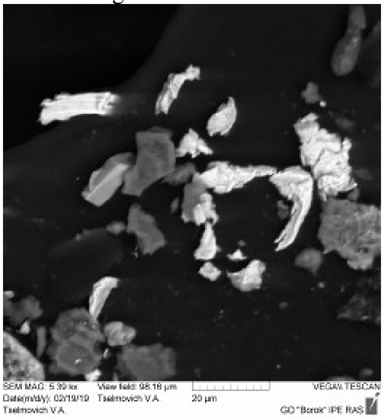

Fig.9. Particles of FeCr alloy

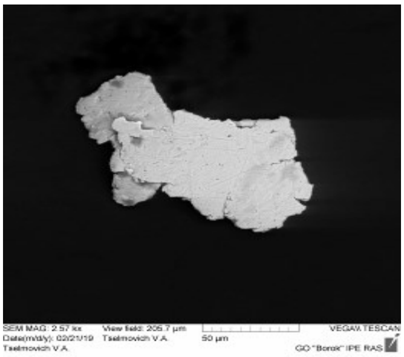

Fig.10. Scale FeNi alloy, peat.

The work was performed in the state framework «Spatio-temporal structure of the ancient geomagnetic field and petrophysics of magnetic minerals as indicators of geological and geophysical processes No. AAAA-A17-117040610183-6», microprobe studies supported by the Russian Foundation for Basic Research, project 16-05-00703a

Conclusions. We compared CD extracted from peat (Tselmovich, 2018; Tselmovich et al, 2019a; Tselmovich et al, 2019b) and Tripoli (Fig.1 – 9). It turned out that they have similar morphology and chemical composition. The most massive or dominant part of CD particles are Mt balls of ablative origin and micrometeorites, pure Fe and FeCr alloys. Particles of pure Ni and its alloys are not preserved in the tripoli sediment; therefore, they were not found, but they were found in peat from various deposits (Tselmovich, 2018; Tselmovich et al, 2019a; Tselmovich et al, 2019b), including the deposit in the Mogilev region (Fig.10). This fact is evidence of the unified nature of a CD the features of which will be studied later.

References:

Pechersky D.M., Gilmanova D.M., Markov G.P., Murdmaa I.O., Nurgaliyev D.K., Tselmovich V.A., Sharonova Z. V. Native iron and other magnetic minerals in the sediments of the north West Atlantic. Results of thermomagnetic and microprobe analyzes // Izv., Phys. Solid Earth (2013) 49: 426. https://doi.org/10.1134/S1069351313020067 Original Russian Text © D.M. Pechersky, D.M. Gil’manova, G.P. Markov, I.O. Murdmaa, D.K.

Nurgaliev, V.A. Tsel'movich, Z.V. Sharonova, 2013, published in Fizika Zemli, 2013, No. 3, pp. 131–153.

Tselmovich V.A., Kurazhkovskii A.Yu., Kazansky A.Yu., Shchetnikov A.A., Blyakharchuk T.A., and. Philippov D.A. Studying the Dynamics of Cosmic Dust Flux on the Earth's Surface from Peat Deposits ISSN 1069-3513, Izvestiya, Physics of the Solid Earth, 2019, Vol. 55, No. 3, pp. 517–527. © Pleiades Publishing, Ltd., 2019. Russian Text © The Author(s), 2019, published in Fizika Zemli, 2019a, No. 3.

Tselmovich V.A. Pure nickel as an indicator of cosmogenic substance // Nineteenth International Conference «Physico-chemical and petrophysical studies in earth sciences». Moscow, 24 – 26, Borok, September 28, 2018. Conference proceedings. Moscow, 2018. p. 330 – 333.

Tselmovich V.A., Kurazhkovskii A.Y. (2019b) Background Magnetic Component of Holocene Cosmic Dust Allocated from Peat. In: Nurgaliev D., Shcherbakov V., Kosterov A., Spassov S. (eds) Recent Advances in Rock Magnetism, Environmental Magnetismand Paleomagnetism. Springer Geophysics. Springer, Cham. First Online 15 August 2018. DOI https://doi.org/10.1007/978-3-319-90437-5_31. Publisher Name Springer, Cham.

Ustinova G. K. Special features of the magneto hydrodynamic situation in the internal heliosphere for the 11-year cycles according to meteorite data UDC 523.165

V. I. Vernadsky Institute of Geochemistry and Analytical Chemistry RAS, Moscow (ustinova@dubna.net.ru)

Abstract. Analysis of cosmogenic radionuclide production rates in 42 chondrites, having fallen successively in 1957-2016, testifies to temporal and spatial variations of the magneto hydrodynamic situation in the internal heliosphere, which are conditioned by temporal generation and dissipation of a layer of magnetic irregularities of the solar wind plasma, effectively modulating the galactic cosmic rays that produced the radionuclides. It allows us to advance a project of a meteorite patrol service for permanent study of further magneto hydrodynamic processes in that part of space, which is important for forthcoming manned flights.

Keywords: *chondrites, cosmogenic radionuclides, internal heliosphere, magneto hydrodynamic processes, cosmic rays, solar activity.*

Introduction: On the threshold of forthcoming cosmic flights for study of the Solar system bodies, the subtle investigation of the radiation environment in the heliosphere, especially in its internal part (up to 4-5 AU) that is exceedingly subject to magneto hydrodynamic processes of interaction of the solar wind plasma with the high energy galactic cosmic rays (GCR), isotropically incoming into the Solar system, becomes of paramount importance. Towards the GCRs isotropically entering the heliosphere from outer space, the Sun radiates solar wind and solar cosmic rays (SCR), which, weakening proportionally to the square distances, propagate up to the dynamic equilibrium boundary with interstellar gas at more than 100 AU. This leads to a gradual decrease in the intensity of the incoming GCRs, to their modulation by the total volume of the solar wind, which is characterized by small GCR gradients (~2–4%/AU). Just such gradients were measured in flights of Mariner-4, -5 in 1964–1965, Pioneer-10, -11 in 1972–1976, and Voyager-1, -2 in 1984–1986 (O'Gallagher, Simpson, 1967; McKibben et al., 1977; Venkatesan et al., 1987), which indicates to a continuous and uniform increase in the GCR intensity with distance from the Earth up to its levelling with the GCR intensity in space at the boundary of the heliosphere.

Effective modulation layer in the region of meteorite orbits: However, such a constant uniformity is inconsistent with dynamic processes and configurations of magnetic fields in the heliosphere. In accordance with the 11-year variations of solar activity, the solar wind and SCRs are emitted by the Sun periodically, with different intensity and speed towards the GCRs. Primarily, their movement is radial, but due to the rotation of the Sun, their paths are gradually bent, twisting in a spiral of Archimedes, and approximately at ~5 AU they become practically azimuthal (Parker, 1979). The twisting magnetic fields of the solar wind, being frozen into the plasma, create almost insuperable barriers for the penetration of GCRs to the Sun; i.e., they practically sweep them from the heliosphere. The higher is the solar activity, the lower is the GCR intensity at the Earth.

Thus, in addition to the GCR modulation (conditioned by the total volume of the solar wind) during the periods of high solar activity, due to the worse diffusion of GCRs in azimuthal fields than in radial ones (their coefficients of longitudinal and transverse diffusion might be different by an order of magnitude (Parker, 1979)), periodically more efficient GCR modulation occurs at 2–5 AU from the Sun, in particular, with higher GCR gradients in this region. Here is apparently a zone of interaction between forward and backward shock waves, high speed solar wind flows, and co-rotating fluxes of low energy particles, which is characterized by increased turbulence of magnetic fields and increased density of magnetic irregularities, effectively scattering GCRs, creating an additional gradient of their intensity to a small gradient with a calm solar wind (Lavrukhina, Ustinova, 1990). At remote distances, the action of those factors becomes gradually weaker because of adiabatic cooling, i.e. due to the solar wind deceleration and its distribution in ever-expanding volume with undeviating decrease of density of magnetic irregularities.

When solar activity declines, nonstationary processes weaken, and such an effective modulating layer gradually becomes thinner and disappears, so that the residual modulation is determined again by only the total volume of the solar wind (Lavrukhina, Ustinova, 1990). It should be noted that the above launches of the spacecrafts Mariner, Pioneer, and Voyager were made during periods of solar activity minima of the 19, 20, and 21 solar cycles, when there was no modulation in the inner heliosphere and the GCR gradients were small. In the years of the development of solar maxima, the spacecrafts were already outside the effective modulation region, and again only small GCR gradients were recorded, due to the total volume of the solar wind only.

Meteorites as cosmic ray variation probes (Lavrukhina, Ustinova, 1990): Meanwhile, the orbits of meteorites (e.g. the stony ones – chondrites) that could fall to Earth lie in the region up to 4–5 AU of the inner heliosphere. The contents of the cosmogenic radionuclides in chondrites are in direct proportionality to the intensity of cosmic rays along the chondrite orbits, which presumes a possibility to use cosmogenic radionuclides in the fallen chondrites to study cosmic radiation along their orbits, i.e. up to ~5AU in the inner heliosphere. Thus, cosmogenic radionuclides in the chondrites that fell during the whole solar cycle, might be valuable instruments to study this range of the effective solar modulation of the GCRs.

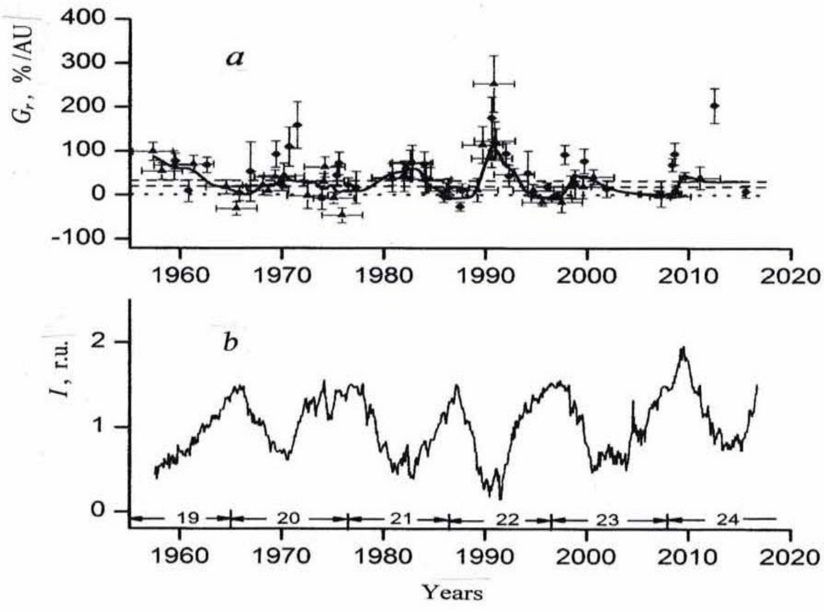

Fig.1 ***(a)*** Variations of the integral gradients of cosmogenic radionuclide production rates along the orbits of 42 chondrites having fallen to the Earth in 1959-2016, according to the contents of ^{54}Mn (circles), ^{22}Na (triangles) and ^{26}Al (dashed horizontals at 20-30%/AU) (Ustinova, Alexeev, 2019) (the curve is a polynomial curve of smoothing the experimental data for five points, taking into account the weight of each of the points; the unknown orbits of chondrites are calculated with a phenomenological method (Lavrukhina, Ustinova, 1990; Lavrukhina, Ustinova 1972)); ***(b)*** Variations of the GCR intensity (E > 100 MeV) near the Earth, according to the balloon experiments (Bazilevskaya et al., 2014)

Just the first studies of radionuclides in the Pribram and Lost City chondrites with the well-known orbits, which fell in the phases of the maximum of the 19 and 20 solar cycles, registered a significant increase in the GCR integral gradients (E > 100 MeV) along their orbits (up to ~4 AU), whereas the data of the Innisfree chondrite, which fell at a minimum of the 20 cycle, recorded small GCR gradients corresponding to the measurements from Pioner-10, -11 (Lavrukhina, Ustinova, 1979; 1981). These patterns were confirmed by our continuous study of cosmogenic radionuclides in the 42 chondrites that have fallen since 1959 (Ustinova, Alexeev, 2019), which has led to monitoring of the spatial and temporal GCR variations in the heliosphere over five solar cycles and has revealed, for the first time, the dynamic nature and features of the GCR solar modulation at 2–4 AU of the internal heliosphere (i.e., within meteoric orbits) (Fig. 1). For ten of these chondrites, the orbits are precisely calculated (http://www.meteoriteorbits.info) (Fig. 1a), and the patterns found for their radionuclide production rates completely correspond to the overall monitoring pattern of 11-year GCR variations over ~60 years, smoothed by a polynomial curve (Fig. 1b). The estimation of the length of the orbits for other chondrites in Fig. 1b was performed by the phenomenological method developed and described in detail in (Lavrukhina, Ustinova, 1990; Lavrukhina, Ustinova 1972). Figure 1c from the stratospheric balloon data (Bazilevskaya et al., 2014) shows that the GCR intensity near the Earth is anti-correlated with the solar activity and the magnitude of the gradients of radionuclide production rates in chondrites. Indeed, gradients range from 0 to ~100%/AU proportionally to the solar activity, being averaged over the solar cycle 20–30%/AU (Lavrukhina, Ustinova, 1990; Alexeev et al., 2015). Direct measurements within ~5 AU from the Sun and variations of the GCR gradients depending on solar activity were recorded only after the launch of the Ulysses spacecraft at its maximum in 1990 (McKibben и др., 2003).

How do these processes manifest themselves on a long-term scale? The second feature of cosmogenic radionuclides, namely, the existence of long-lived radionuclides, in particular, ^{26}Al with $T_{1/2}$ = 0.717 Ma, reveals such fundamental patterns. To estimate the average GCR intensity at 1 AU for a million years, the ^{26}Al depth profiles were analyzed in the columns of the lunar soils Luna-24 (L-24) and Apollo-15 (Ap-15) (Lavrukhina, Ustinova, 1990; Lavrukhina, Ustinova, 1971). It is shown that they are quantitatively reproduced by calculation using the average GCR intensity ($E > 100$ MeV) $I = 0.24$ cm^{-2} s^{-1} sr^{-1}, corresponding to the average intensity during modern solar cycles, which indicates to the constancy of the solar modulation processes near the Earth during the last ~1 million years.

What happens at other heliocentric distances? Such unique information turns out to be accessible due to the ^{26}Al contents measured at the moments of fall of 10 chondrites of known orbits, in which they were accumulated being irradiated by the average GCR intensity for ~ 1 million years at an average heliocentric distances of orbits of those chondrites (Ustinova, Alexeev, 2019). Calculations of the production rates of ^{26}Al in identical chondrites at 1 AU using an average intensity of $I = 0.24$ cm^{-2} s^{-1} sr^{-1} and a comparison with the measured contents of ^{26}Al revealed production rate gradients of this isotope of the order of 20–30%/AU (in Figs. 1a this range is marked with dashed horizontals). The growth of the average GCR intensity for a million years with the heliocentric distance (corresponding to this gradient) is presented in Fig. 2 (curve 1) (Ustinova, Alexeev, 2019)). It is seen that curve 1 does not demonstrate the continuous growth of the GCR intensity in accordance with the gradient of about 2-4%/AU, conditioned with only total volume of the solar wind (shown by lines 2). It can be seen that curve 1 demonstrates a steep increase in the GCR intensity with a peak of 2–4 AU due to the periodic accumulation of GCR in this area due to the worst conditions for further penetration to the Earth. The tendency to the subsequent flattening of the GCR intensity with further distance from the Earth indicates to the locality of the heliosphere with dynamic processes of solar modulation, i.e., the continuous emergence of an effective modulating layer of magnetic irregularities at 2–4 AU of the internal heliosphere during the last ~1 million years. This indicates to the consistency of the magneto-hydrodynamic situation in the solar system, at least for the last million years.

In conclusion, it should be noted (as was already mentioned above) that nowadays there is no alternative to permanent and continuous study of magneto hydrodynamic situation in the internal heliosphere due to use of cosmogenic radionuclides in meteorites falling to the Earth. It allows us to advance a project of patrol meteorite service for constant study and forecast of peculiarities of magneto hydrodynamic processes in that region of cosmic space, which is especially important on the threshold of forthcoming manned space travels (Ustinova, Alexeev, 2018).

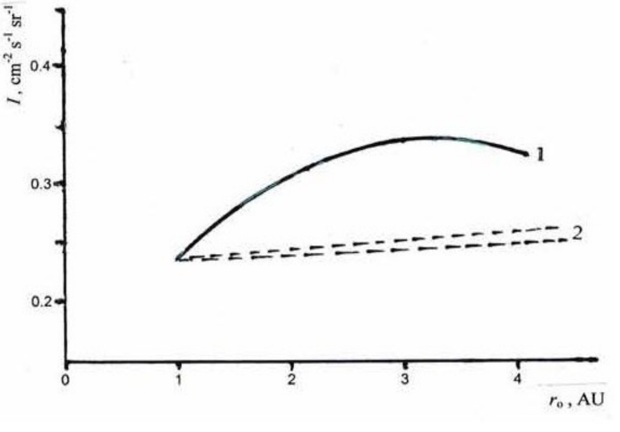

Fig.2 – Growth of the GCR (E>100MeV) intensity averaged for a million years with heliocentric distances, according to the data of ^{26}Al contents in 10 chondrites of known orbits (curve 1 (Ustinova, Alexeev, 2019)), in comparison with lines 2, which describe an expectable growth of the GCR intensity under their modulation only by the total volume of the solar wind (gradients 2-4%/AU)

The work is partly supported by Program № 28 of Fundamental Researches of the Presidium RAS

References:

Alexeev V. A., Ustinova G. K. // Geochemistry International. 2006. V. 44. No. 5. pp. 423-438.

Alexeev V.A.,et al. // Adv. Space Res. 2015. V. 56. pp. 766-771. Doi: 10.1016/j.asr.2015.05.004

Bazilevskaya, G.A., et al. // Proc. 33-rd Int. Cosm. Ray Conf., 2013. Rio de-Janeiro, The Astroparticle Phys. Conf. arXiv: 1411.7534v.1 [astroph. SR] 27 Nov. 2014.

Lavrukhina A.K., Ustinova G.K. // Nature. 1971. V.232. No. 5311. pp. 462-463.

Lavrukhina A.K., Ustinova G.K. // Earth and Planet. Sci. Letts. 1972. V.15. No 4. pp.347-360.

Lavrukhina A.K., Ustinova G.K. // Proc. 16-th Int. Cosm. Ray Conf. 1979. Kyoto. V.3. pp. 206-211.

Lavrukhina A.K., Ustinova G.K. // Adv. Space Res. 1981. V 1. No 3. pp. 143-146.

Lavrukhina A.K., Ustinova G.K. Meteorites as probes of cosmic ray variations. Moscow. Nauka, 1990. 262 p. (in Russian).

McKibben R.B., et al., // Proc. 15-th Int. Cosm. Ray Conf. 1977. Plovdiv. V. 3. pp. 240-245.

McKibben, R.B., ,et al. // Ann. Geophys. 2003. V. 21. pp. 1217–1228.

O'Gallagher J.J., Simpson J.A. // Astrophys. J. 1967. V.147. No. 2. pp. 819-827.

Parker E. N. 1979. Cosmic magnetic fields. Oxford: Clarendon press. 841p.

Ustinova G. K. // Doklady Physics. 2016. V. 61. No.11. pp.571-575.

Ustinova G. K. Alexeev V. A. // MAPS. 2018. V. 53. No. S1. pp. 6056.

Ustinova G. K., Alexeev V. A. // Doklady Physics. 2019. V. 64. No 3. pp. 139-143.

Venkatesan D.,et al.M. //Proc. 20-th Int. Cosm. Ray Conf. 1987. Moscow. V.3. pp. 385-288.

Yurkovets V.P. Catastrophe layers of the near zone of Ladoga impact. UDC 551.4:552.6

The Academy of DNA Genealogy, Boston, USA
(valery.yurkovets@gmail.com)

Abstract. This article presents some results of the study of Ladoga impact-volcanic structure created by the fall of a major, about 11 kilometers across, cosmic body onto present-day northwest Russia about 38.5 thousands years ago.

Keywords: *Ladoga impact-volcanic structure; catastrophe layers; coptoclastites; volcanic ash*

Age of Ladoga impact-volcanic structure, figure.1, resulting from a fall on the territory of northwest Russia a major, about 11 kilometers across, cosmic body is 38.5 thousand years. The fall of such a large body disturbed the integrity of Baltic shield, which caused a giant eruption - approximately 1500 km3 of volcanic ash was released into the atmosphere, which became horizon marker in upper-Pleistocene sediments of East European platform. Ash plume covered a vast territory from south Ladoga region in the north Russian Plain to its south part where it is currently preserved in aeolian and diluvial deposits in the Dnieper-Donetsk interfluve and fine sandy loams and clay loams of basin of Don River. Coptoclastites and catastrophe layers of the near zone of Ladoga impact were buried under it in Ladoga region (Yurkovets, 2012).

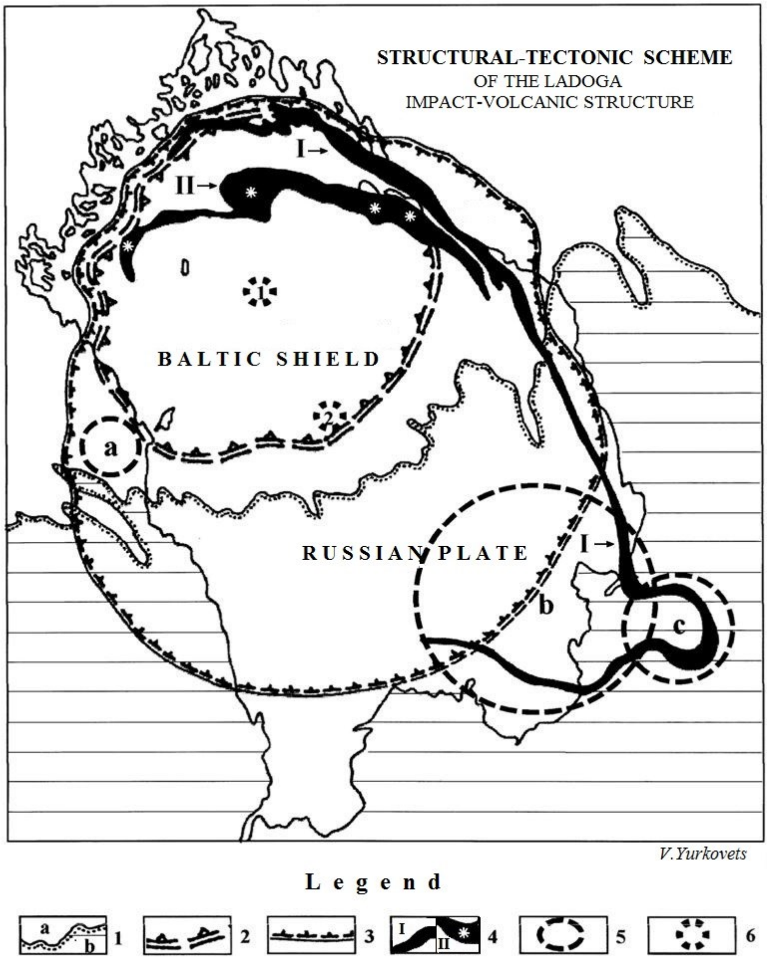

Fig. 1. Structural-tectonic scheme of Ladoga impact-volcanic structure
1 - boundary between plate cover (Russian platform) and crystalline basement (Baltic shield); 2 - boundary of impact crater; 3 - boundary of collapse caldera of Ladoga volcano; 4 - crop outs of impact-melt formations (I) and impact-melt formations complicated with extrusive domes of Ladoga volcanic edifice (II); 5-astroblemes formed by satellite bodies: (a)-Yablonovskaya, b and c - Bolshaya and Malaya Pashskie; 6 - epicenters of Lodoga impact structure (1) and subsidence caldera of Ladoga volcano (2)

Fig. 2. Industrial outcropping of volcanic ash.

Maximum ash thickness in the south, in the region of Duvanka settlement near Voronezh where paleolithic sites of Kostyonkovsko-Bortchevsky region have been buried (so-called layer in ash) is 1.25 m. In the north, in glacial deposits of Kirsinsko-Shapkinsky kames (middle Valdai horizon of upper Pleistocene of Ladoga area), that are in 150 km distance from the structure center, ash layers are up to several meters, fig. 2.

A considerable part of Ladoga ashes settled on the top of the ice sheet because the event occurred during one of Valdai Glaciation maximums. This part of ashes with the end of glaciation hit mainly in Volga runoff forming so-called "chocolate clay" of lower Khvalynskaya suite of upper-Pleistocene deposits of north part of Caspian basin (Yurkovets, 2012). Also, such ash deposits are known in Bulgaria, Hungary, Romania, Greece, Cyprus and Eastern Mediterranean bottom sediments (Kholmovoy, 2008).

In Ladoga region ash layers overlap coptoclastites of Ladoga impact presented mainly by fragmentary material of silt size and containing about 5% of impact glass. Coptoclastites position in industrial outcropping (mining of sand and gravel mix) of one of Kirsinsky open cuts is shown by the arrow in Figure 2. The border between coptoclastites and volcanic ash is extremely contrasting, which indicates instant change in composition of residues as a result of powerful explosive eruption following the impact, fig. 3.

Under coptoclastites there are catastrophe layers deposited represented by water-glacial sediments Kisinsky kames, containing products of explosive stage of Ladoga impact. fig. 4.

Quite insignificant, on a scale of geology, age of events and related to glaciation special conservation conditions of short-lived part of coptogenic complex helped to preserve unique evidence of Ladoga event. These primarily include shock microstructures (ShM) formed in quartz sandstones in near zone of impact by specific Ladoga tektites containing microscopic (0.02 mm or less) fragments of moissanite. Moissanite appeared at an early stage of formation of Ladoga impact-volcanic structure as a result of crystallization in expanding explosion gas cloud of sublimated phase of polycrystalline moissanite formed, in turn, from shungite-containing rocks of the target, for which at the place of impact there were necessary conditions including quite high pressure and temperature (Yurkovets, 2016).

Fig. 3. Contact of coptoclastites with volcanic ash.

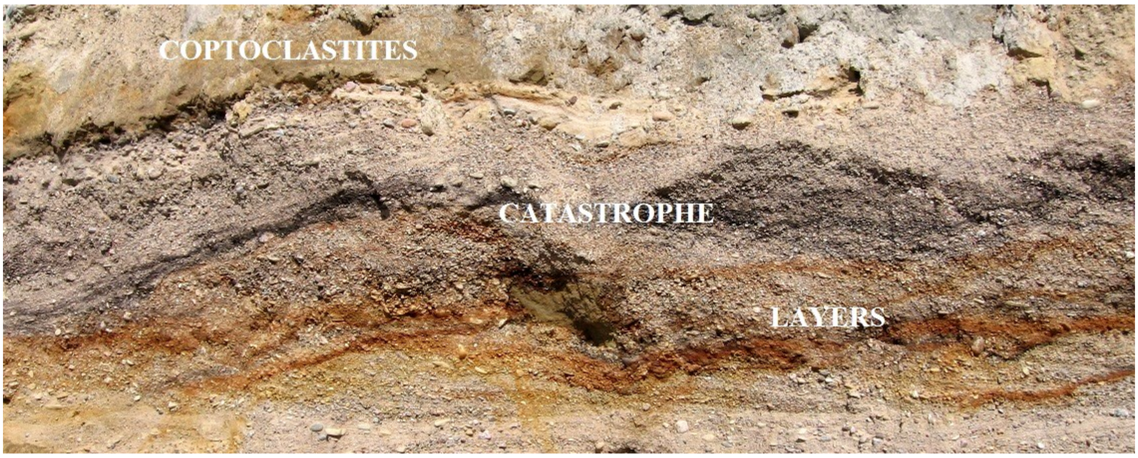

Fig. 4. Catastrophe layers.

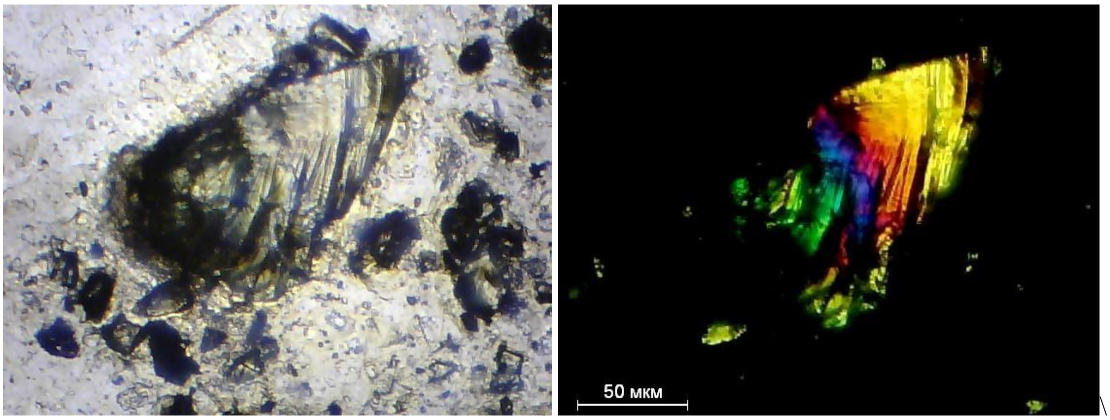

Fig. 5. Moissanite

Moissanite is one of the markers of Ladoga impact, it is found in all sampling points both in impact crater and beyond, at a distance of up to 150 kilometers from the center of fall, fig. 5.

Along with ShM similar forms of macroscopic are found in Ladoga region. They are formed by high-speed inelastic (penetrating each other) drops strikes of impact melt (mainly iron and alkali) moving with “cosmic” velocities to pebble of Cambrian and Vendian quartz sandstones outside the crater with formation of crushed to pelitic size mass bound by melted cement. Part of such inclusions preserved “aerodynamic” form after falling into sandstone, fig. 6. In figure 6, in the center, a drop after destruction of host pebble is shown.

Fig. 6. Impact inclusions in sandstone.

Inclusions consist of crushed with cloud extinction quartz bound by pyrite-melanterite-jarosite (depending on initial composition of drops and conditions of their occurrence) cement. Host quartz has no signs of impact, is well-rounded, contact cement (Yurkovets, 2016). On the border of inclusions and host mass grains of quartz are characterized by a classical impact spallation occurring when grain stretching by reflection impulse (Ernstson, Claudin; 2011).

Thickness of iron sublayers is up to ten and more centimeters. They mainly consist of target rocks bounded with ochre. Genesis of their impact component coincides with the one of “classic” catastrophe layers formed by major impacts in sedimentary rocks of our planet. The essential difference is that in the near zone “catastrophe” is not only their genesis, but also the nature of interaction with the target species resulted in formation of shock microstructures, impact inclusions in pebble of Cambrian and Vendian quartz sandstones, isotropization and impact spallation of quartz in them, etc. (Yurkovets, 2012).

In “classic” catastrophe layers “small fragments of meteorites” are found very rare (Feldman, 1990), so expected in catastrophe layers of Ladoga region were rare finds of strong magnetic samples with a uniform for the entire territory of such finds petrologic composition, aerodynamic shape, remnants of melting crust, fig. 7. In addition to ilmenite, magnetite, pyrrhotine, titanomagnetite and magnetite they contain barringerite, troilite and native iron, Table. 1.

Fig. 7. Samples destroying in oxidation zone.

Table 1. Results of optical, x-ray-structure, microprobe analyses.

Plagioclase	50-55%
Clinopyroxene	30-35%
Olivine	1-2%
Quartz	1-2%
Micrographic concretion of quartz and potassium feldspar	1-2%
Ore minerals: ilmenite, pyrrhotine, titanomagnetite, magnetite, barringerite*, troilite*, cnative iron**	8-10%
Accessory minerals: apatite	≈ 1%

**) based on x-ray-structure analysis (Karpinsky Russian Geological Research Institute (VSEGEI)*
***) based on microprobe analysis (Borok IPE RAS)*

Melting crust of those samples is mainly destroyed. As judged by significant limonitization it is destroyed by weathering. But on some samples from great depth (below the oxidation zone) it has partly preserved, fig. 7, to the right. Sample No. 103 typical for this group, fig. 7, to the left, was studied using an optical, x-ray-structure, microprobe, silica and rare-earth analyses, on the basis of which it was pre-classified as HED group meteorites (Yurkovets, 2015).

Apparently, presence of barringerite and native iron in these samples is the reason for the fact that they are rather quickly destroyed in oxidation zone with the formation of multilayer “coat”. Samples with melting crust lose it pretty quickly too, without passing, however, limonitization stage near surface layer. As a result, all the samples have a rough mesh surface inheriting crystal structure of the sample, fig. 7. As judged by in section position these finds are individual falls as a part of “satellite” bodies accompanying main Ladoga. It happen to be several large “satellite” astroblemes in them formed around Ladoga (Janisjarvi in the north of Ladoga, Yablonevskaya in the west, Bolshaya and Malaya Pashskie in the southeast), fig. 1. Janisjarvi is a proved astrobleme (Masaitis, 1973). The rest are classified as constituting in this capacity in geomorphological, geological, structural and tectonic and, ultimately, genetic relations a whole both with Ladoga impact-volcanic structure and Janisjarvi astrobleme. Being at the same time, independent impact formations (Yurkovets, Mikheeva, 2015).

References:

Masaitis V. L. and others. Geology of astroblemes. 1980 Leningrad, Nedra, 231 p.

Feldman V. I. Petrology of impactites. M.: MSU publishing house. 1990. 300 p.

Kholmovoy G. V. Morphoscopic features of Neogene and Quaternary volcanic ashes of Voronezh region//VSU Bulletin, series: Geology, 2008. No. 1. P. 19-22.

Yurkovets V. P. Ladoga impact-volcanic structure//Proceedings of Russian Academy of DNA genealogy. (ISSN 1942-7484). Raleigh, N.C., Lulu. 2012. V. 5 No. 8 P. 1059-1085.

Yurkovets V. P. 2015. Extraterrestrial minerals in rocks of Ladoga region. Works of all-Russian Annual Seminar on Experimental Mineralogy, Petrology and Geochemistry (VESEMPG). Publication editor A. A. Kadrik /M.: GEOKHI RAS, 2015; 343 p. ISBN 978-5-905049-11-8

Yurkovets V. P. Moissanite in the rocks of Ladoga region as an indicator of Ladoga impact // Experiment in Geosciences. V. 22, No. 1. P. 11-12

Ernstson K., Claudin F. 2011. Impact spallation in nature and experiment. http://www.impact-st...and-experiment/ (дата обращения 22.01.2019)

Yurkovets V.P., Mikheeva A.V. On the origin of the Ladoga impact-volcanic structure // Computing Center Bulletin. Series: Math. model. in geoph. – Novosibirsk: NCC Publisher, 2015. N.18 P. 53 -67